On the operation of a long-pulse KrCl excimer laser

This work was financially supported by SenterNovem.

The research was carried out at the Laser Physics and Nonlinear Optics Group, Faculty of Science and Technology, University of Twente, P.O. Box 217, 7500 AE Enschede, The Netherlands.

On the operation of a long-pulse KrCl excimer laser,
Lars C. Casper,
PhD thesis, University of Twente.
ISBN 978-90-365-2512-1

Printed by Wöhrmann Print Service, Zutphen, The Netherlands, 2007.

ON THE OPERATION OF A LONG-PULSE KrCl EXCIMER LASER

Proefschrift

ter verkrijging van
de graad van doctor aan de Universiteit Twente,
op gezag van de rector magnificus,
prof. dr. W.H.M. Zijm,
volgens het besluit van het College voor Promoties
in het openbaar te verdedigen
op vrijdag 25 mei 2007 om 16.45 uur

door

Lars Christian Casper
geboren op 20 April 1975
te Hanau, Duitsland

Dit proefschrift is goedgekeurd door de promotor,

prof. dr. K.-J. Boller

en de assistent promotor,

dr. ir. H. M. J. Bastiaens

List of Publications

- L.C. Casper, H.M.J. Bastiaens, P.J.M. Peters, K.-J. Boller, and R.M. Hofstra, *"Long-pulse KrCl laser with a high discharge quality"*, accepted for publication in Applied Physics B, 2007. Published online: dx.doi.org/10.1007/s00340-007-2621-y.

- L.C. Casper, H.M.J. Bastiaens, P.J.M. Peters, K.-J. Boller, and R.M. Hofstra, *"Gain of a long-pulse KrCl laser"*, submitted to Journal of Applied Physics.

- L.C. Casper, H.M.J. Bastiaens, P.J.M. Peters, K.-J. Boller, and R.M. Hofstra, *"A compact three-electrode discharge system for long-pulse high-power excimer discharges"*, submitted to Plasma Source Science and Technology.

- L.C. Casper, H.M.J. Bastiaens, P.J.M. Peters, K.-J. Boller, and R.M. Hofstra, *"Gain and fluorescence in a long-pulse KrCl laser"*, in XVI. International Symposium on Gas Flow, Chemical Lasers, and High-Power Lasers, Gmunden, to be published in Proc. of SPIE, 2007.

- L.C. Casper, H.M.J. Bastiaens, P.J.M. Peters, K.-J. Boller, and R.M. Hofstra, *"A three-electrode discharge system for long-pulse high-power KrCl excimer lasers"*, in XV. International Symposium on Gas Flow, Chemical Lasers, and High-Power Lasers, Prague, Proc. SPIE **5777**, 554 (2005).

- L.C. Casper, H.M.J. Bastiaens, P.J.M. Peters, K.-J. Boller, and R.M. Hofstra, *"Three-electrode discharge system for long-pulse high-power KrCl/KrF excimer lasers"*, Poster presentation, 16th NNV/CPS - Plasma Physics & Radiation Technology Symposium, Lunteren, The Netherlands, 2004.

- L.C. Casper, H.M.J. Bastiaens, P.J.M. Peters, K.-J. Boller, and R.M. Hofstra, *"A novel Long-Pulse KrCl Excimer Laser"*, Poster presentation, 17th NNV/CPS - Plasma Physics & Radiation Technology Symposium, Lunteren, The Netherlands, 2005.

- L.C. Casper, H.M.J. Bastiaens, P.J.M. Peters, K.-J. Boller, and R.M. Hofstra, *"Dust Formation in a High-Power Long-Pulse Excimer Laser"*, Poster presentation, 18th NNV/CPS - Plasma Physics & Radiation Technology Symposium, Lunteren, The Netherlands, 2006.

- L.C. Casper, H.M.J. Bastiaens, P.J.M. Peters, K.-J. Boller, and R.M. Hofstra, *"Gain of a long-pulse KrCl excimer-laser"*, Poster presentation, 19th NNV/CPS - Plasma Physics & Radiation Technology Symposium, Lunteren, The Netherlands, 2007.

In memory of my parents.
To my family.

Abstract

High-power lasers pumped by a gas discharge are extensively used in industrial applications. Of particular importance are lasers pumped by an electric discharge in excimer gas mixtures because this allows the generation of powerful ultraviolet radiation (UV), with wavelengths below 350 nm. Due to the short wavelength, these lasers offer the unique possibility to structure materials on the sub-micron scale, when focused or with mask techniques. Also, the absorption of UV radiation is strong in many materials, which allows an improved control of the ablation depth. Also when larger structures are to be fabricated, excimer lasers can be of advantage, e.g. for hole drilling in materials which are too brittle for mechanic processing, such as ceramics. The excimer lasers used predominantly so far are XeCl lasers and KrF lasers but these show important limitations. Although XeCl lasers can be operated with a high spatial beam quality, close to the fundamental limit of diffraction, the comparatively long wavelength (308 nm) often leads to an undesirably deep penetration of the radiation, which leads to problems with the quality of machining. KrF lasers emit at a shorter wavelength (248 nm), which reduces the absorption depth. However, the spatial beam quality of KrF lasers is rather poor. This limitation arises because, with decreasing wavelength, discharges in excimer are known to become spatially inhomogeneous through instabilities leading to filamentation, within typically only ten or a few tens of nanoseconds after the ignition of the discharge. This excludes the build-up of an unperturbed, high-quality beam in sufficiently many roundtrips through the laser resonator. High-precision processing may still be done with low quality beams,

by spatial filtering with masks or diaphragms. But this strongly reduces the efficiency because only a small fraction of the radiation reaches the work piece. What is actually required is an excimer laser, which emits a diffraction-limited, high quality beam but at a much shorter wavelength than that of XeCl lasers, possibly even below the wavelength of KrF lasers.

The goal of this thesis was to demonstrate such a high-beam quality laser with a wavelength shorter than both XeCl and KrF. Our choice was to realize, for the first time, a KrCl laser with 222 nm wavelength where a high spatial homogeneity of the discharge is maintained over a largely extended duration of up to several hundred nanoseconds. As spatial inhomogeneities that are present during the ignition of the discharge will continue to grow until they dominate the structure of the discharge, our approach was to employ discharge excitation techniques, which should enable a homogeneous ignition. This way, it should be possible to extend the homogeneous regime of the discharge, increase the laser pulse duration and, thereby, enable a high beam quality.

In this work, we describe the successful realization of the first discharge pumped KrCl laser with a high discharge homogeneity with durations of several hundred nanoseconds, which resulted in the generation of laser pulses with a long duration and high pulse energy. In our set-up, the laser is pumped in the so-called prepulse-mainpulse scheme. Here the prepulse, a fast-rise time high-voltage pulse, is employed to ignite the discharge homogeneously. A subsequent mainpulse is used to sustain the discharge after its ignition and delivers the main part of the electrical pump energy into the gas mixture. Note that the application of only the main pulse would lead to strong discharge inhomogeneities because of the slow rise time of the main pulse pump circuit that arises from the need to deliver a high pulse energy within an extended time interval. Due to the different rise times, the prepulse and the mainpulse can be optimized only (for homogeneity and pulse energy, respectively) when the two circuits are separated by a fast switching mechanism. This is why we have chosen a three-electrode discharge with two adjacent discharge volumes. Here the discharges are capacitively coupled such that the first discharge rapidly switches the ignition of

the second discharge.

To investigate the stability of KrCl discharges for various discharge conditions, we built a test set-up that is based on the described three-electrode prepulse-mainpulse excitation. The small dimensions of the set-up allowed us to initiate and sustain discharges under optimum conditions, i.e., a very short rise time of the prepulse voltage and the mainpulse discharge current, both as short as a few to a few tens of nanoseconds. As a result of these optimum conditions, we were able to demonstrate very homogeneous discharges in KrCl for record time intervals of up to 300 ns in the test set-up. This shows the high potential of KrCl discharges to generate laser pulses with a high spatial beam quality and long pulse duration.

Based on the result with the test set-up, a complete three-electrode KrCl discharge laser was designed and constructed, brought into operation and characterized. In a first step, to optimize the laser output, i.e., maximize the pulse energy and pulse duration, we performed a detailed study of the most important discharge system parameters. These are the composition of the gas mixture, the mainpulse voltage and the resulting pump current and pump power density. As a main result we found that, in both laser discharge chambers, a high discharge quality is achieved for long pump durations of several hundred nanoseconds.

To determine the optical gain parameters in these long-pulse, homogeneous KrCl discharges, we built an oscillator-amplifier set-up with the three-electrode discharge system. Here the first discharge volume is used to provide gain for the two-mirror laser oscillator, and the second volume is used as a single-pass amplifier. With this set-up, we measured for the first time the central gain parameters for a KrCl laser with long pulse duration. We found a net gain of 1.6% cm^{-1}, which is maintained over a long time interval resulting in laser pulses with durations of up to 150 ns. The peak gain in our measurement is lower than in standard KrCl lasers, where the pump current is stronger, but where the duration of the current pulse is short and the output beam quality is low. Determining the small-signal gain, the losses, and the saturation intensity, we found that the small-signal gain and also the losses increase with increasing pump power density. The saturation intensity was found

to rise with the pump power density as well. This shows that a strong population quenching of the upper laser level by collisions with electrons is present in standard KrCl lasers, but is reduced in long-pulse KrCl discharges. After a first optimization of the resonator output coupling, and when employing the optimum pump conditions that we previously identified, we find a high specific laser pulse energy of 0.45 J/l emitted over a long pulse duration of 117 ns. These values form a clear improvement compared to previously reported KrCl lasers.

To explore ways for a further increase of the output energy, we employed a simple numerical model and compared its predictions with our experimental data. The model predicts the temporal development of the intracavity photon number density and the laser output power, based on the temporally dependent values of small-signal gain, losses, and saturation intensity, as found in independent experiments. This way of modeling enables to avoid the much more complex modeling of the discharge kinetics. We found a good agreement of the laser model predictions with our experimental results, which justify the several model assumptions and approximations made. Motivated by the agreement we used a variation of the model input parameters, to observe the influence on the laser output. We found that a considerable increase of 30% of the pulse energy seems possible by employing a shorter resonator, while the pulse duration reduces only marginally.

In conclusion, we demonstrated the feasibility of a KrCl laser with high discharge homogeneity for durations of several hundred nanoseconds, resulting in long laser pulse durations and high pulse energies. With these significant improvements compared to previous work, the present thesis may form a highly important step for the development of industrial KrCl excimer lasers in a unique combination of short wavelength with high spatial beam quality.

Samenvatting

Gasontlading gepompte, hoog vermogen lasers worden intensief gebruikt in allerhande industrile toepassingen. Van specifiek belang zijn lasers die gepompt worden met een elektrische ontlading in excimeer gas mengsels omdat hiermee hoogvermogen ultraviolet (UV) straling kan worden gegenereerd met een golflengte korter dan 350 nm. Lasers die deze korte golflengte genereren bieden unieke mogelijkheden om materialen op sub-micron schaal te structereren door focusering of door gebruik te maken van maskers. Daarnaast is de absorptie van UV straling in veel materialen erg sterk wat een betere beheersing van de ablatiediepte mogelijk maakt. Ook voor de fabricage van grotere structuren, bieden excimeer lasers voordelen, zoals bijvoorbeeld voor het boren van gaten in materialen die te bros zijn om mechanisch te bewerken, zoals bijvoorbeeld keramiek.

Tot nu toe worden voornamelijk XeCl en KrF excimeer lasers gebruikt maar deze hebben aanzienlijke beperkingen. Alhoewel men XeCl lasers kan maken met een goede ruimtelijke bundel kwaliteit, nabij fundamentele diffractie limiet, leidt de betrekkelijke lange golflengte (308 nm) dikwijls tot een ongewenste diepe penetratie van de straling, waardoor problemen ontstaan met de kwaliteit van de bewerking. KrF lasers zenden straling uit met een kortere golflengte (248 nm) waardoor de absorptie diepte afneemt. Echter, de ruimtelijke bundel kwaliteit van deze KrF lasers is tamelijk slecht. Deze beperking komt voort uit de ruimtelijke inhomogeniteit die ontstaat in de ontlading in excimeer lasers tengevolge van instabiliteiten, en die typisch binnen een tiental

tot enkele tientallen nanoseconden na de ontsteking leiden tot filamentatie van de ontlading. Hierdoor wordt een ongestoorde opbouw van een laser bundel met een hoge bundel kwaliteit, door voldoende rondgangen in de laser resonator, uitgesloten. Door gebruik te maken van ruimtelijke filters, zoals maskers of diafragma's, kan men met een slechte kwaliteit laser bundel nog wel hoge precisie bewerkingen uitvoeren. Hierdoor wordt echter de efficiency van het bewerkingsproces sterk gereduceerd omdat slechts een klein deel van de laser straling het werkstuk bereikt. Voor hoge precisie bewerkingen is eigenlijk een excimeer laser nodig die een diffractie gelimiteerde bundel met een hoge kwaliteit uitzendt en met een veel kortere golflengte dan XeCl lasers, eventueel zelfs met een golflengte korter dan KrF lasers.

Het doel van dit proefschrift is de werking aan te tonen van een laser met een hoge bundel kwaliteit en met een kortere golflengte dan zowel de XeCl als de KrF laser. Hiervoor hebben we ons gericht op de realisatie van een KrCl laser met een golflengte van 222 nm waarin we een hoge ruimtelijke kwaliteit van de ontlading kunnen handhaven over een lange pulsduur van enkele honderden nanoseconden. Omdat ruimtelijke inhomogeniteiten, die al tijdens de ontsteking van de ontlading aanwezig zijn, uitgroeien totdat ze de structuur van de ontlading domineren, hebben wij gekozen voor een ontladings excitatiemethode die een homogene ontsteking mogelijk maakt. Op deze manier zou het mogelijk moeten zijn om de homogene duur van de ontlading en daarmee de laserpulsduur te vergoten waarmee dan een hoge bundelkwaliteit bereikt kan worden.

In dit proefschrift wordt de succesvolle realisatie beschreven van de eerste ontladingsgepompte KrCl laser met een hoge graad van ontladingshomogeniteit voor de duur van enkele honderden nanoseconden waardoor het mogelijk is laserpulsen te genereren met een lange pulsduur en hoge pulsenergie. In onze experimentele opstelling, wordt de laser gepompt met een zogenoemd voorpuls-hoofdpuls circuit. De voorpuls, een hoogspanningspuls met een korte stijgtijd, wordt gebruikt voor het homogeen ontsteken van de ontlading. De daaropvolgende hoofdpuls wordt gebruikt om na de ontsteking de ontlading te onderhouden, deze levert daarmee het grootste deel van de elektrische pompenergie aan het gasmengsel. Aangetekend dient te worden dat

het aanbieden van alleen de hoofdpuls zou leiden tot sterke inhomogeniteiten in de ontlading door de lange stijgtijd van het hoofdpulscircuit die volgt uit de voorwaarde dat een hoge pulsenergie aangeleverd moet worden over een groot tijdsinterval. Door de verschillen in stijgtijd, kunnen de voorpuls en de hoofdpuls alleen worden geoptimaliseerd (naar homogeniteit en pulsenergie, respectievelijk) als de twee circuits gescheiden worden door een snel schakelend mechanisme. Daarom hebben wij voor een drie-elektroden ontladingssysteem gekozen met twee aan elkaar grenzende ontladingsvolumes. In dit systeem zijn de ontladingen capacitief gekoppeld waardoor de eerste ontlading de ontsteking van de tweede ontlading initieert.

Voor het onderzoek naar de stabiliteit van KrCl ontladingen onder verschillende ontladingsomstandigheden, hebben we een testopstelling gebouwd die is gebaseerd op het beschreven drie-elektroden voorpuls-hoofdpuls excitatiesysteem. Door de beperkte afmetingen van de opstelling is het mogelijk om ontladingen te ontsteken en te onderhouden onder optimale omstandigheden, dit wil zeggen met een zeer korte stijgtijd van zowel de voorpulsspanning als de hoofdpuls ontladingsstroom, beide in de orde van slechts enkele tot enkele tientallen nanoseconden. Onder deze optimale omstandigheden, hebben wij in de testopstelling zeer homogene ontladingen in KrCl kunnen genereren over tijdsintervallen met een recordlengte tot 300 ns. Deze resultaten tonen aan dat KrCl ontladingen zeer veelbelovend zijn voor de generatie van laserpulsen met een hoge ruimtelijke bundelkwaliteit en lange pulsduur.

Op basis van de resultaten behaald met de testopstelling is een complete drie-elektroden KrCl ontladingslaser ontworpen en geconstrueerd, in bedrijf gesteld en gekarakteriseerd. Als eerste is voor de optimalisatie van de laser opbrengst, dat wil zeggen de maximalisatie van de puls energie en de pulsduur, een gedetailleerde studie gemaakt van de meest belangrijke parameters van het ontladingssysteem. Deze parameters zijn de samenstelling van het gasmengsel, de hoofdpulsspanning en de resulterende pompstroom, en de dichtheid van het pompvermogen.

Als belangrijkste resultaat hebben we gevonden dat in beide ontladingsvolumes kwalitatief uitstekende ontladingen kunnen worden gemaakt met pulsduren van meerdere honderden nanoseconden lang. Voor het bepalen van de optische versterkingspa-

rameters in deze lange puls, homogene KrCl ontladingen, hebben we met het drie-elektroden ontladingssysteem een oscillator-versterker opstelling gebouwd. In deze opstelling voorziet het eerste ontladingsvolume in de versterking voor de laser oscillator, die voorzien is van twee spiegels. Het tweede volume wordt gebruikt als versterker voor de oscillator puls die hier een enkele maal doorheen wordt geleid. Met deze opstelling zijn we in staat geweest voor de eerste maal de belangrijkste versterkingsparameters van een lange puls KrCl laser te bepalen. We hebben een netto-versterking van 1.6%/cm gemeten over een lang tijdsinterval waardoor laser pulsen van 150 ns lang kunnen worden gegenereerd. De piek-versterking, zo blijkt uit onze metingen, is lager dan bij standaard KrCl lasers die gepompt worden met een grotere stroom waarvan echter de pulsduur kort is en waardoor kwaliteit van de laser bundel laag is. Uit metingen aan de klein-signaal versterking, de verliezen en de verzadigingsintensiteit blijkt dat zowel de klein-signaal versterking als de verliezen toenemen met de dichtheid van het pomp vermogen. Tevens blijkt dat de verzadigingsintensiteit toeneemt met de dichtheid van het pomp vermogen. Dit geeft aan dat er een sterke afbraak van de populatiedichtheid in bovenniveau van de laser plaatsvindt door botsingen met elektronen in de standaard KrCl lasers. In lange puls KrCl ontladingen is deze afbraak echter beperkt.

Na een eerste optimalisatie van de uitkoppeling van de resonator, waarbij we onder de optimale pompcondities werken zoals deze eerder zijn bepaald, vinden we een hoge specifieke laser pulsenergie van 0.45 J/l die wordt uitgezonden in een lange puls van 117 ns. Deze waarden tonen de duidelijke verbetering aan ten opzichte van eerder gerapporteerde KrCl lasers.

Om te onderzoeken op welke manieren de energieopbrengst van de laser kan worden vergroot, hebben we een eenvoudig numeriek model gebruikt waarvan de uitkomsten zijn vergeleken met de experimenteel verkregen data. Het model voorspelt de tijdsafhankelijke ontwikkeling van de foton dichtheid in de optische trilholte en het uitgezonden vermogen van de laser op basis van de tijdsafhankelijke waarden van de klein-signaal versterking, de verliezen en de verzadigingintensiteit zoals we die hebben gemeten in onafhankelijke experimenten. Met deze manier van modeleren

vermijden we de veel complexere modelering van de ontladingskinetiek. De gemeten experimentele resultaten komen goed overeen met de voorspellingen van het model, waarmee de verschillende aannames en benaderingen die gebruikt zijn in het model zijn gerechtvaardigd. Gesteund door deze goede overeenstemming, hebben we de invoer parameters van het model gevarieerd om de invloed daarvan op de laseropbrengst te kunnen volgen. We hebben gevonden dat de pulsenergie met 30% verhoogd kan worden door gebruik te maken van een kortere resonator, wat de pulsduur slechts marginaal verminderd.

Tot besluit, we hebben de haalbaarheid aangetoond van een KrCl laser waarin een hoge ontladingshomogeniteit gehandhaafd kan worden gedurende honderden nanoseconden, wat heeft geresulteerd in de generatie van lange laserpulsen en hoge pulsenergien. Met de belangrijke verbeteringen die behaald zijn in vergelijking met eerder onderzoek, vormt dit proefschrift een zeer belangrijke stap in de ontwikkeling van industrile KrCl excimeer lasers die een uitzonderlijke combinatie bieden van korte golflengte en een hoge ruimtelijke bundel kwaliteit.

Contents

Chapter 1

Introduction

Since the first experimental realization of **l**ight **a**mplification by **s**timulated **e**mission of **r**adiation (laser) by Maiman in the early 60's [1], the field of laser physics and related application has experienced rapid growth. Due to the special spatial, temporal and spectral properties to which the output light from lasers can be tailored, they have acquired a central position in a wide number of applied and scientific fields. The most well-known presence of lasers is found in applications related to data storage and transmission, such as DVD players, laser printers, and fiber networks, to name a few. Lasers have also found a strong position in medical applications, where tailoring the light output enables improved medical diagnostics, such as in optical coherence tomography, and in medical treatment, such as the eye corona surgery. The third field of applications benefiting strongly from lasers is the manufacturing industry, where lasers are used in automated environments. In this case, mostly the high spatial quality of lasers in combination with a high output power offer a greater precision and higher processing speeds, respectively, thereby reducing production costs. Examples of industrial applications include precision welding, precision hole drilling, and local surface treatment.

In a basic scheme, a laser consists, of a light amplifying medium and two mirrors

that form a cavity. The cavity builds up a very intense light field along its axis due to repeated amplification of light in the amplifying medium. This leads to three basic properties of a laser, which are used in the aforementioned applications. Firstly, lasers can easily be designed to be monochromatic, i.e., the emitted light is confined to frequencies in a very narrow band, particularly, when compared for example to thermal sources such as an electric bulb. This makes lasers ideal for spectroscopic applications. Secondly, laser can be brought to emit with a high spatial coherence, i.e., the light propagation in space being sharply defined. Lasers can thereby provide light at the fundamental limit of maximum beam quality, so-called diffraction-limited beams. The importance of this for applications is that such beams can be focused as tightly as the fundamental wave-limit of light permits, i.e., to a tiny spot size being in the order of the laser wavelength. This allows, e.g., high-precision material processing at hugely elevated intensities. Thirdly, the light generated by lasers is temporally coherent, meaning that a phase relation exists between the emitted light waves in a laser, in contrast to the thermal emission of light, for example, in an electric bulb. Even more, when the emission spectrum of the amplifying medium is broad, lasers can be designed such that a temporally stable phase relation exists between the various spectral components. The temporal coherence enables, with a suitable selection of the laser's power and phase spectrum, applications ranging from holography and interferometry, to the generation of ultrashort pulses for providing huge peak powers or highest temporal resolution.

During the past years of laser development, many materials have been found that exhibit strong amplification (gain), in combination with an easy excitation and low absorption. According to the physical state of the gain medium, lasers are coarsely divided into Free Electron Lasers (FEL), solid-state, liquid, and gas lasers, which mostly cover the spectral range from the far infrared (FIR, several 10s to 100s of micrometer wavelength) to the ultraviolet (UV, shorter than 400 nm wavelength).

There are numerous applications in this huge wavelength interval from the FIR to the UV, however, for applications in material processing, the UV with its short wavelength principally offers the highest precision. Furthermore the UV, with its high energy

per photon, enables also processing of materials with a large electronic bandgap, i.e., materials with extreme hardness or which are not absorbing longer (visible or infrared) wavelengths. When looking to more details one finds, actually, that many of these applications are much hindered or even unexplored by the lack of UV lasers which provide a combination of a shorter UV wavelength, a high average output power, and, most importantly, a high spatial quality (coherence) of the output in the form of a diffraction limited beam.

When looking closely to these specifications, it is only the excimer gas lasers [2–4] that can offer these high output powers in the UV wavelength range [5,6]. This makes excimer lasers the prime candidates for optical processing of a largely extended range of materials, and for structuring of such materials in an unprecedented combination of precision and throughput, such as has been demonstrated previously at longer UV wavelengths with XeCl lasers [7].

The operation of excimer lasers typically requires high electrical input powers in the order of several MW, such that their operation is bound to the pulsed regime with durations in the order of a few nanoseconds. To achieve a sufficiently high average power for a high throughput, excimer lasers are operated at repetition rates of typically several 10s of Hz and, favorably reaching the kHz range. When looking at the corresponding pump requirements, the only practical way of pumping is via a gas-discharge, i.e., excitation by sending high-power current pulses through the excimer gas mixture [6].

Although excimer lasers are efficient sources for the generation of UV radiation and are commercially available since 20 years, the tailoring of the output beam properties towards high spatial quality still forms a significant technological challenge involving some fundamental obstacles. The excitation in the form of a short current pulse usually leads to a high optical peak power in the MW-range, which, together with the high photon energy of UV photons, degrades the laser optics and limits their lifetime. Furthermore, the average power, particularly for wavelengths below 250 nm, is low compared to the favored kW-regime for fast material processing. The highest disadvantage of such lasers is, however, that the output beam is far from its

maximum possible beam quality, the diffraction limit, and resembles merely that of a directional lamp-like (spatially incoherent) source. With such poor spatial quality the beam cannot be tightly focused and is thus inappropriate for high-precision machining. So far, the implementation of such short wavelengths in precision machining is only possible by strong spatial filtering or by using high-resolution masks. However, this strongly reduces the overall efficiency, machining speed and throughput, because a major part of the laser output remains unused.

A promising approach to eliminate these problems and which increases the efficiency and precision of excimer laser based material processing has been demonstrated in the group of W. J. Witteman [8–10], where a significant lengthening of the discharge current pulse has been realized in XeCl laser gas mixtures while simultaneously preserving the spatial homogeneity of the discharge. This way the light in the laser resonator is amplified by a smaller factor per round trip, but also over a largely increased number of round trips, which much increases the beam quality of the output towards the diffraction-limit. With this technique, a duration of the laser gain of several hundred nanoseconds had been obtained, generating hundreds of nanoseconds long laser pulses, with a high beam quality close to the diffraction-limit [10]. Such pulse durations are long compared to the resonator round trip time of the pulse, giving these lasers the label long-pulse laser (also used hereafter). Furthermore, the extended pulse duration reduces the optical peak power and thereby promised a longer lifetime of the optics.

With such promise, these improvements have been taken up by a collaborating laser company, Nederlands Centrum voor Laser Research (NCLR), who systematically pursued the exploitation of this potential of long pulses in XeCl excimer lasers. So far they succeeded in developing an industrial high-beam-quality XeCl laser at 308 nm with a high repetition rate of 1 kHz (1 kW average power) based on the named long-pulse discharge techniques. [11–13]. Here, the low peak power of the output pulses became indeed a key advantage as the lifetime of the resonator optics is typically several orders of magnitude longer than in short-pulse XeCl lasers. Also, the effective suppression of higher-order transverse modes enabled by long-pulse operation allows,

e.g., to transform the beam without much power-loss into various other beam shapes desired for machining, by using low-loss (transparent) diffractive or refractive optics. Furthermore, it became clear that machining with long-pulse excimer lasers is often much more energy-efficient compared to machining with short pulses of the same energy, because material can be removed via melting and blow-out, rather than via energy-consuming evaporation [7].

Based on these promising developments with XeCl lasers, which operate at 308 nm, our goal was to extend these approaches by realizing a long-pulse excimer laser at a much shorter wavelength. Among the various candidates for a different excimer laser gas, the F_2-based lasers provide the shortest wavelengths but also the highest degree of technological problems. To warrant higher chances for a feasibility, we decided to focus our research on KrCl. This excimer emits at a much shorter wavelength of 222 nm than XeCl, while a relatively high maturity in short-pulse operation promises that one may arrive at a successfully working long-pulse laser design. At the same time the short wavelength bears significant potential for novel steps in material processing. In particular, one expects a higher efficiency of processing because the UV absorption of most materials increases towards shorter wavelengths. Examples of potential applications are photo-induced changes of the surface structure in polymers and composite materials [14–18] where the penetration of 308 nm radiation is undesirably high. Additionally one can vision the machining of finer structures with non-contact methods of large throughput. An example is the micro-structuring of airplane components. Here, an improved cooling in jet engines and methods to reduce turbulences promise a significant reduction of the fuel consumption and CO_2 loading of the atmosphere. Based on such possibilities and other potential applications, we investigated whether the efficient operation of KrCl lasers with diffraction-limited beam quality due to long-pulse excitation can indeed be realized.

1.1 Outline of the thesis

The work presented in this thesis was a joint project between the University of Twente and the Nederlands Centrum voor Laser Research (NCLR). Compared to XeCl discharge lasers, long-pulse KrCl lasers have received only minor attention and most essential parameters, such as the gain in long-pulse operation were not known. For this reason, the experiments presented in this thesis cover the full range. They include basic investigations of the discharge dynamics, the design, realization and operation of a long-pulse KrCl laser, with an experimental characterization of the central gain parameters. The latter characterization enabled modeling of the laser for exploring further improvements.

In chapter 2, an introduction into the fields of laser and discharge physics, with emphasis on excimer laser is given. Chapter 3 outlines and compares the various electric discharge circuits that can be employed to pump excimer lasers. Via conditions necessary for the most efficient energy transfer from the pump source into the gas discharge, electric excitation circuits are presented that appear suitable to pump long-pulse discharge lasers. In chapter 4, we present the three-electrode discharge excitation circuit and we describe the results from testing it in long-pulse operation, initially with a small discharge test-cell. As a result, we were able to demonstrate for the first time KrCl discharges with long durations of the homogeneous glow regime for up to 300 ns. The corresponding design criteria found in this manner are taken up in Chapter 5 for the design of a long-pulse KrCl laser based in a three-electrode discharge excitation circuit. With this set-up, compared to previously published results on KrCl lasers, we demonstrate successfully the first discharge pumped high-pressure KrCl laser with a high discharge quality that resulted in an considerable increased laser energy and well-extended pulse duration. This shows success with regard to the essential goals of this work. Chapter 6 presents the first characterization of the gain parameters in long-pulse KrCl lasers. These are based on a time-resolved measurement of the fluorescence, and also on a direct measurement of the time-dependent optical gain in long-pulse KrCl amplification (in an oscillator-amplifier configuration). These measurements enabled to determine so-far unknown gain parameters in long-pulse KrCl

excitation, the small-signal gain, losses in the gain medium, and the saturation intensity. Based on the knowledge of these central parameters, and implementing them in a simple model for the laser resonator, we describe the temporal development of an optical pulse in the laser, which is in good agreement with the experimentally observed pulse shape.

Finally, we give a summary of the essential results and a conclusion of the work presented in this thesis, which points out remaining steps for improvements and research fields to be considered for the future.

Chapter 2

Discharge pumped excimer-lasers

Nowadays, ultraviolet (UV) light sources are important tools in industrial and scientific applications, such as surface treatment, material processing and micro-machining. However, many applications would strongly benefit if high-power light sources became available with a high spatial coherence. In particular, since the spot size of a focused beam reduces with decreasing wavelength, the application of UV-lasers with high spatial coherence is very promising for the generation of structures on the (sub-) micrometer-scale. So far, only excimer gases have proved to be efficient gain media for high-power UV-lasers, while other gain materials such as found in standard solid-state lasers are highly absorbing in this wavelength range.

This chapter outlines the important physical processes that have to be considered for the successful operation of excimer lasers with a high spatial coherence. A brief introduction to laser theory is given in Sec. 2.1. Important properties of excimer molecules for gain are presented in Sec. 2.2. This section focuses on the intrinsic properties of the excimer molecule and their production. A short description of important reac-

tions leading to the production and loss of excimers is presented. The properties and dynamics of gas discharges with respect to the efficient production of excimer molecules is presented in Sec. 2.3. In Sec. 2.4 we discuss the initiation and growth of discharge inhomogeneities. Such discharge inhomogeneities are the main limitation for the spatial coherence of excimer lasers and methods for suppressing their growth are discussed in the end of Sec. 2.4.

2.1 Laser fundamentals

In the following, a brief overview of the basic principles of lasers is given. A more detailed discussion can be found in various text books, see, e.g., Siegman [19] or Milonni and Eberly [20].

The basic idea of a laser is the amplification of light due to an interaction of the light with the medium in which it travels. Although the medium consists of particles, e.g., atoms or molecules, each possessing a large number of discrete energy levels, for a better understanding, let us consider an ensemble with just two energy levels, consisting of a ground state ($|E_1\rangle$) with an energy E_1 and an excited upper state ($|E_2\rangle$) with an energy E_2, where $E_2 > E_1$. The energy difference between both states is proportional to the frequency, ν, of an electromagnetic wave:

$$\Delta E = E_2 - E_1 = h\nu, \tag{2.1}$$

where h is Plank's constant. In the ensemble, the population of the states is distributed between both levels, where N_1 is the number density of the ground state and N_2 the excited state number density. As shown in Fig. 2.1, there are three possible processes which generate or absorb photons.

1. *Absorption*: A photon with the energy $E_{\mathrm{ph}} = h\nu$ can be absorbed by a particle in the ground state, inducing a transition to the excited state. The number of absorbed photons depends on the number density in the ground state and the

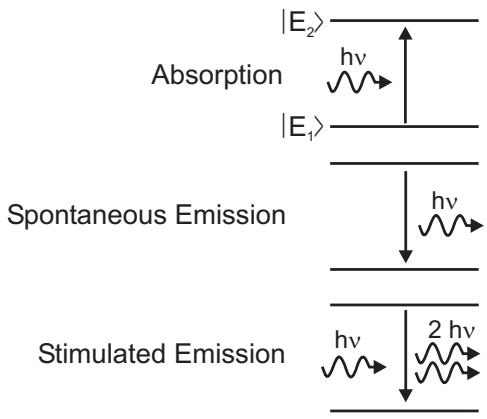

Figure 2.1: Schematic overview of the energy levels in a two-level system and the possible transitions. $|E_1\rangle$: ground state, $|E_2\rangle$: excited state, $h\nu$: photon energy.

photon number density, ρ_ν, at the transition frequency. The resulting change of the number of particles populating the upper state is described by a rate equation:

$$\frac{dN_2}{dt} = B_{12}\rho_\nu N_1, \tag{2.2}$$

where B_{12} is the so-called Einstein coefficient of absorption.

2. *Spontaneous emission*: A particle in the excited state can return into its ground state by emitting a photon with energy $E_{\mathrm{ph}} = h\nu$ but at a random time, with random direction and with random polarization. The number of transitions into the ground state is proportional to the number of particles in the excited state and is described according to:

$$\frac{dN_1}{dt} = A_{21}N_2, \tag{2.3}$$

where A_{21} is the so-called Einstein coefficient of spontaneous emission.

3. *Stimulated emission*: In this case, a photon with the energy $h\nu$ causes a particle

in the excited state to release its energy by emission of a photon of well-defined properties. The transition rate into the ground state is given by:

$$\frac{dN_1}{dt} = B_{21}\rho_\nu N_2, \tag{2.4}$$

where B_{21} is the so-called Einstein coefficient of stimulated emission. The emitted photon is in phase with the incident photon, it travels in the same direction and possesses the same polarization. Under suitable conditions, stimulated emission can be used to amplify electromagnetic waves, as will be shown below.

It can be shown by thermodynamical arguments that the Einstein coefficient of absorption and stimulated emission are related via the degeneracy of the energy levels, g_1 and g_2:

$$g_1 B_{12} = g_2 B_{21}. \tag{2.5}$$

Furthermore, the coefficient for stimulated emission and spontaneous emission follow the relation:

$$\frac{A_{21}}{B_{21}} = \frac{8\pi h\nu^3}{c^3}, \tag{2.6}$$

where c is the vacuum speed of light.

2.1.1 Population inversion and gain

In a simple picture of an incident electromagnetic wave with frequency ν that travels through a medium in which stimulated emission and absorption can take place, its intensity, I_ν, changes by ΔI_ν due to propagation over a distance Δx [21]:

$$\Delta I_\nu = h\nu B_{21}\frac{I_\nu}{c}N_2 g(\nu)\Delta x - h\nu B_{12}\frac{I_\nu}{c}N_1 g(\nu)\Delta x, \tag{2.7}$$

where $g(\nu)$ is the lineshape function that describes the spectral spread of the considered transition. The x direction is given by the propagation direction of the incident wave. For simplicity, we have neglected spontaneous emission in Eq. 2.7, because its

random direction usually yields only a minor contribution to the intensity along the propagation direction.

For sufficiently small ΔI_ν and Δx, and taking Eq. 2.5 into account, we obtain:

$$\frac{dI_\nu}{dx} = \frac{h\nu}{c} B_{21} g(\nu) \left(N_2 - \frac{g_2}{g_1} N_1 \right) I_\nu, \tag{2.8}$$

from which we define the *population number density*:

$$\Delta N = (N_2 - \frac{g_2}{g_1} N_1), \tag{2.9}$$

and the *gain*:

$$\gamma_0 = \frac{h\nu}{c} B_{21} g(\nu) \Delta N = \sigma_{\mathrm{SE}} \Delta N, \tag{2.10}$$

where

$$\sigma_{\mathrm{SE}} = \frac{h\nu}{c} B_{21} g(\nu) \tag{2.11}$$

is the cross section for stimulated emission. As can be seen from these equations, for $\Delta N > 0$, the gain becomes positive and the intensity increases according to:

$$I_\nu(x) = I_\nu(0) e^{\gamma_0 x}, \tag{2.12}$$

where $I_\nu(0)$ is the initial value of the intensity. For the amplification of light it is required that the excited state has a higher population density than the ground state (Eq. 2.9), i.e., $\Delta N > 0$, which is called *population inversion*.

Since, in a thermal equilibrium, most atoms will populate the ground state, energy has to be added in a very specific manner to the system in order to generate the population inversion. This procedure is called *pumping*.

To favor light amplification over spontaneous emission, the stimulating light field needs to be sufficiently intense, as can also be seen by the product $B_{21}\rho_\nu$ in Eq. 2.4. For this reason, emitted photons usually are fed back into the emitting medium. This feedback is realized by the use of an optical resonator, formed by mirrors, as shown,

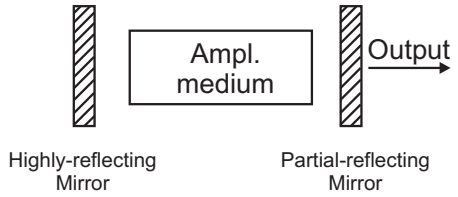

Figure 2.2: Simplified schematic diagram of a laser, which is formed by the amplifying medium and two mirrors that form a resonator. The radiation can be coupled out through a partial reflecting mirror, as indicated on the right side.

e.g., in Fig. 2.2.

2.1.2 Gain saturation

With the goal to describe the steady-state operation of a laser, we describe the population density of the upper state $|E_2\rangle$ with a rate equation that includes also the pumping of the upper level. For this, we assume an ideal laser in the sense that the lower state $|E_1\rangle$ decays immediately and is for this reason unpopulated ($N_1 = 0$). This situation is almost perfectly fulfilled in the type of lasers investigated in this thesis, as will be described below. Writing the rate equation for N_2, including stimulated emission, absorption, and spontaneous emission and using the definition of σ_{SE}, we obtain:

$$\frac{dN_2}{dt} = R_2 - \frac{N_2}{\tau_2} - \frac{\sigma_{\mathrm{SE}} I_\nu}{h\nu} N_2, \tag{2.13}$$

where R_2 is the pump rate populating the upper level, and τ_2 the effective lifetime of the upper state, which includes spontaneous emission and quenching of the upper state and is given by:

$$\frac{1}{\tau_2} = \frac{1}{\tau_{\mathrm{s}}} + \frac{1}{\tau_{\mathrm{Q}}}. \tag{2.14}$$

with the spontaneous fluorescence lifetime, τ_s, and the collisional quenching lifetime, τ_{Q}. Assuming steady-state ($d/dt = 0$), we can solve for N_2:

$$N_2 = \frac{R_2 \tau_2}{1 + \frac{I_\nu}{I_{\mathrm{sat}}}}, \tag{2.15}$$

where we defined the *saturation intensity* as:

$$I_{\mathrm{sat}} = \frac{h\nu}{\sigma_{\mathrm{SE}} \tau_2}. \tag{2.16}$$

It is evident from Eq. 2.14 and Eq. 2.16 that a decrease of the quenching lifetime will increase the saturation intensity. Since $N_1 = 0$, we can write for the gain:

$$\gamma_s = \frac{R_2 \sigma_{\mathrm{SE}} \tau_2}{1 + \frac{I_\nu}{I_{\mathrm{sat}}}}. \tag{2.17}$$

This equation shows that the gain reduces as the intensity I_ν increases, which is called *gain saturation*. Specifically, Eq. 2.17 shows that the saturation intensity is the intensity that reduces the gain to half the value expected for amplification of low intensities.

2.1.3 Threshold condition

An amplification of the light field can take place, when a population inversion has been established. However, in addition, there are also optical losses present in real lasers, which reduce the light intensity such that the total (net) change of the intensity becomes:

$$I(L) = I_0 e^{(\gamma - \alpha)L}. \tag{2.18}$$

Here, L is the length of the gain medium, and α is a loss coefficient that includes all optical losses inside the resonator, except the desired outcoupling at the mirrors (active losses). A number of processes contribute to the undesired (passive) losses:

1. Absorption and scattering at the mirrors.

2. Partial transmission of a mirror where outcoupling was not intended.

3. Diffraction of light out of the resonator, e.g., at the mirrors.

4. Scattering due to refractive index inhomogeneities in the gain medium.

5. Absorption by other gas constituents and other possible transitions.

When looking at the resonator feedback in the presence also of active losses by selecting partially transmitting mirrors with a non-unity reflectivity R, the reflection from a mirror causes a reduction of the intensity from I to RI. In a two-mirror resonator as used in this thesis, therefore, after a round trip, the intensity is given by the reflection coefficients of both mirrors, R_1 and R_2. The light field is only amplified, if the intensity after a round trip, I_f, is larger than the initial intensity, I_i:

$$\frac{I_\mathrm{f}}{I_\mathrm{i}} = R_1 R_2 e^{2(g-\alpha)L} > 1, \tag{2.19}$$

Requiring that the intensity after a round trip has to be at least equal to the initial intensity leads to the following definition of the threshold gain:

$$g_\mathrm{th} = \alpha - \frac{1}{2L} \ln\left(R_1 R_2\right). \tag{2.20}$$

The simple considerations show that the gain, losses, and saturation intensity are intrinsic properties of the laser medium which determine what external parameters (such as the mirror and resonator length) enable the desired operation of the laser. In this thesis, a KrCl excimer laser is operated in a novel regime and systematically investigated for the first time. Correspondingly, this includes the first systematic study of the named intrinsic parameters of KrCl in that regime, as will be described in Chapter 6.

2.2 Excimers

The following section treats several properties of excimers and their discharge kinetics, particularly in KrCl, that make them suitable as gain medium for lasers. The goal of this section is to give a brief overview, while a more detailed treatment can be found in various text books, such as Refs. 22–24.

Excimers, an abbreviation for **exc**ited d**imers**, are so far the only gain medium suitable for the generation of UV radiation with large average powers. In other spectral ranges of longer wavelength, many gain materials are at disposal, such as semiconductors, dyes or solid-state materials. However, for the generation of ultraviolet radiation, the pump power density required for reaching the laser threshold increases strongly, because the minimum pump power needed to reach threshold scales with λ^{-5} [25]. With this, it can be shown that the formation of excimers, which will be described in detail below, requires pump power densities that are higher than the damage threshold of solid-state materials.

An excimer is a di-atomic molecule, where the two involved atoms attract and bind to each other only in an excited state, and which can decay into its constituents by the emission of a photon. The wavelength of the emitted photon depends on the atoms used to form the excimer molecule. Such excimers can be formed in a plasma with a high pump rate by igniting a discharge in a suitable gas mixture. However, high-power requirements in the order of several MW cm^{-3}, reaction kinetics and discharge instability limit excimer lasers to pulsed devices in the nanosecond regime. The development of powerful cw-excimer lasers is hindered on the one hand due to intrinsic properties of the generation of excimers, which will be discussed in the following, and on the other hand due to the practical limitations of delivering the required high pump power.

Excimers formed by a rare-gas ion and a halogen ion have been found to be very efficient UV emitters. An overview of the known laser transitions of rare-gas halide excimers is shown in Tab. 2.1. The rare-gas halogen excimers exhibit laser gain in the wavelength range between 193 nm and 351 nm.

	Ne	Ar	Kr	Xe
F	(108)	193	248	351
Cl		175	222	308
Br		(161)	206	282
I			(185)	(253)

Table 2.1: Overview the main optical transition wavelength (nm) of rare-gas halogen excimer species. Given is the laser transition, brackets apply for transitions where only fluorescence has been observed. Taken from Ref. 25.

The ground state of excimer molecules is either repulsive or weakly bound ($N_1 \approx 0$). Thus, a population inversion is realized as soon as the molecule is formed (corresponding to N_2 in the previous section). A simplified scheme of the potential energy of an excimer as a function of the interatomic separation is shown in Fig. 2.3. The scheme shown is representative also for the KrCl molecule. Shown are the potential energy curves of the excited electronic states B, C, and D, the lower-lying state A, and the ground state X. The excimer molecule (RgH^*) is formed from an ionized rare-gas atom, Rg^+, and a halogen ion, H^-. The molecule decays into its atomic species Rg and H by emission of a photon with the energy $h\nu$, according to the potential difference between the states. The mass of the nuclei is too large to cause a displacement on the time scale of the transition. Hence, the interatomic separation remains constant during the transition, which is known as the Franck-Condon principle [24].

In KrCl, the laser transition takes place between the B and the X state, where X is a repulsive state. A weak C→A transition that emits photons with a wavelength of $\lambda = 235$ nm has been observed as well [27]. The lasing wavelength of KrCl is $\lambda = 222$ nm for the B→X transition, which corresponds to a photon energy of 5.6 eV. The linewidth of the transition is determined by the potential energy curve of the repulsive ground state. A strong repulsive ground state results in a broad linewidth since small variations in the interatomic distance lead to large changes in the potential energy difference. For example, KrCl has a bandwidth of $\Delta\lambda = 2$ nm due to its bound-free transition. For comparison, XeCl, which has a very weakly bound ground state, a narrower linewidth of $\Delta\lambda = 0.5$ nm has been measured for the B→X transition [28].

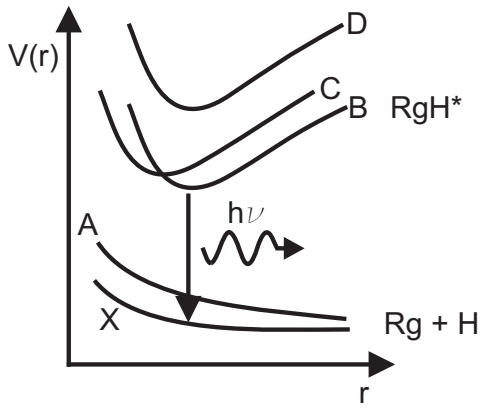

Figure 2.3: Simplified scheme of the potential energy $V(r)$ of an excimer molecule as function of the interatomic separation r. Rg: Rare-gas, H: halogen, hν: photon energy. Taken from Ref. 26

Another important property of excimer molecules is their radiative lifetime, which is the decay time of the excited state given solely due to spontaneous emission. From measurements, a radiative lifetime of the B state of $\tau_r = 19$ ns has been reported [29]. Using the linewidth and radiative lifetime, the cross section for stimulated emission can be calculated according to [25]:

$$\sigma_{\mathrm{SE}} = \frac{1}{4\pi}\left(\frac{\ln 2}{\pi}\right)^{1/2}\frac{\lambda^4}{c\tau_r\Delta\lambda}, \tag{2.21}$$

where c is the vacuum speed of light. Evaluating Eq. 2.21 for KrCl leads to an estimated stimulated emission cross section of 0.8 Å^2, which is approximately 50% lower compared to the calculated value for XeCl. The implications of the lower cross section for the gain of a KrCl laser will be discussed in chapter 6.

2.3 Discharge kinetics

The main formation reactions of excimers will be outlined in this section, in order to provide the background to explain the experimental results presented in Chapter 5 and 6. Since gas discharge physics is a mature field in experimental physics, a vast amount of literature is available. A thorough overview is given, e.g., in Ref. 30. Specific aspects of the formation of excimers can be found in Refs. 22–24.

As has been recalled in the previous section, the formation of excimers requires that rare-gas and halogen ions are created. Given the small cross section and gain of a single excimer molecule, a high number density of at least 10^{12} cm^{-3} is required for high-power operation [22]. Furthermore, due to the short lifetime of the excited state, this large number must be formed within a few nanoseconds. These conditions can only be fulfilled in gas discharges that are operated at atmospheric pressure [22] or with electron beam (E-beam) pumping. Here, an electron beam with energies of several hundred keV, is injected into the gas volume, causing the formation of excimers molecules. This technique has several drawbacks compared to discharge pumping:

1. E-beam pumping can only sustain a repetition rate of a few pulses per minute compared to kHz operation of discharge pumped lasers. This results in low average power from E-beam pumped lasers.

2. The high accelerating voltages, of several hundred kV, is technically very demanding compared to a few tens of kV typically required for discharge pumped lasers.

3. The electron beam is to be created in a vacuum chamber and to be transfered with low loss into the gas volume, operated at atmospheric pressures. This is typically done by passing the electrons through a foil, a few tens of μm thick, that separates both volumes. Due to the very high currents, damage of the foil is a common problem, which is avoided in discharge pumped lasers.

Formation of rare-gas ions

In gas discharges, an electric current flows through the laser gas mixture in the presence of an applied electric field. Inelastic collisions between the electrons and atoms cause excitation and ionization of the gas mixture constituents [23]:

$$\begin{aligned} \mathrm{Rg} + \mathrm{e}^- &\longrightarrow \mathrm{Rg}^* + \mathrm{e}^- \\ \mathrm{Rg}^* + \mathrm{e}^- &\longrightarrow \mathrm{Rg}^+ + 2\mathrm{e}^- \end{aligned} \tag{2.22}$$

where Rg denotes a rare-gas atom, Rg^* an excited rare-gas atom, and Rg^+ an ionized rare-gas atom. Ionization via excited states, so-called step-wise ionization, is the most important contribution to the formation of rare-gas ions. Since the average electron temperature in a discharge is typically of the order of 2-4 eV [21,30] and since energies of 10 eV or higher are required for a direct ionization of rare-gas atoms, this is only possible with electrons in the high energy tail of the electron energy distribution (EED). In discharge pumped lasers, this process is therefore of minor importance for the rare-gas ionization.

The next step towards the excimer formation is the build-up of molecular rare-gas ions via a three-body recombination (dimerization) process:

$$\mathrm{Rg}^+ + \mathrm{Rg} + \mathrm{M} \longrightarrow \mathrm{Rg}_2^+ + \mathrm{M}, \tag{2.23}$$

where M denotes a third reaction partner that is required to fulfill the conservation of momentum. Typically, the third reaction partner comes from a buffer gas atom (He or Ne), which forms more than 90% of the gas mixture. In KrCl discharges, the dimerization reaction leads to a fast (within 40 ns) build-up of Kr_2^+ ions compared to XeCl dsicharges, where a slower build-up time (within 200 ns) has been observed [27]. This has lead to the suggestion that this reaction is more important for the formation of KrCl than for XeCl.

The formation of halogen ions typically proceeds as an electron attachment reaction

of the form:

$$\mathrm{XH} + \mathrm{e}^- \longrightarrow \mathrm{H}^- + \mathrm{X}, \tag{2.24}$$

where H denotes a halogen atom (for example chlorine) that is initially bound in a molecular form (XH) to a species X (for example hydrogen). These molecules are also called halogen donor. As a result of the attachment reaction, the number of electrons and halogen donor molecules reduces. This has important implications for excimer formation and the stability of gas discharges, as will be explained in more detail in Chapter 4. Additionally, as a result of the attachment reaction, the halogen ion concentration increases. Although required for the excimer formation, halogen ions can reduce the laser performance through absorption of photons. In the case of KrCl lasers, Cl^- is assumed to be a dominant absorber at the laser wavelength [31], since the photodetachment coefficient of Cl^- increases strongly for wavelengths below 300 nm [32, 33]. Therefore, a model of KrCl lasers should include also absorption losses in the laser gas medium.

The previous reactions form the precursors required for the formation of excimer molecules. In the following, the three most relevant excimer formation channels are given [23]:

$$\begin{aligned} \mathrm{Rg}^+ + \mathrm{H}^- + \mathrm{M} &\longrightarrow \mathrm{RgH}^* + \mathrm{M} \\ \mathrm{Rg}_2^+ + \mathrm{H}^- &\longrightarrow \mathrm{RgH}^* + \mathrm{Rg} \\ \mathrm{Rg}^* + \mathrm{XH} &\longrightarrow \mathrm{RgH}^* + \mathrm{X}. \end{aligned} \tag{2.25}$$

The first two reactions are so-called ion-ion recombinations that take place in the form of three body reactions. In the third, the so-called harpooning reaction, an excited rare-gas atom reacts with the bound halogen to form an excimer molecule. The relative importance of the ion-ion recombination and the harpooning reaction depends on the EED and the energy levels of the gas discharge constituents. For example, in discharge pumped ArF lasers, the harpooning reaction contributes almost 80% [34] while in KrCl lasers only 5% of the excimer molecules are formed via this reaction [27].

The presented treatment has been limited to the most important reactions that take place in a discharge. Many more reactions are known to be involved, however, their discussion falls outside of the scope of this introduction. More information on discharge kinetics can be found, for example, in Refs. 35–37.

2.4 Discharge stability and homogeneity

The following section introduces the discharge conditions, which are necessary to employ a discharge as an spatial homogeneous gain medium for laser operation.

Many industrial applications for discharge pumped lasers require a beam cross-section of several square-centimeters. Additionally, in order to achieve pulse energies of several Joules the gain volume, given by the volume filled by the discharge, is in the order of several liters. Consequently, a very important condition is that the discharge remains spatially homogeneous over the duration of the pump pulse. However, without special precautions, discharges in rare-gas halide mixtures will be spatially inhomogeneous from the beginning. In this case, the discharge will not fill the desired volume, but will be restricted to streamers, which are thin channels of elevated current density with dimensions ranging from a few μm to mm in diameter. Therefore, streamers strongly reduce the efficiency of excimer lasers or even prevent laser oscillation. In order to discuss the possibilities to improve the discharge homogeneity, in the following, the formation of a discharge is briefly outlined in order to identify causes that are responsible for the formation of inhomogeneities.

The initiation of a discharge requires an electric field that is strong enough to start and maintain electron avalanches by ionization processes initiated by the electrons drifting towards the anode [30]. An important characteristic of this process is its threshold behavior. Avalanches will not start below a certain critical electric field strength. As soon as this field strength is reached, the electron avalanches are initiated. However, only after a sufficiently high electron density is reached, the impedance of the gas reduces and a large current can flow through the plasma, causing the formation of

excimer molecules according to the reactions presented in Sec. 2.3. In particular, the electron balance, given by gain and loss of electrons, is used to describe the temporal development of the discharge, which is related to the electron density, $n_e(t)$, via a rate equation:

$$\frac{dn_e}{dt} = (\alpha - a) v_d \, n_e - \tau \, n_e^2, \tag{2.26}$$

where α is the Townsend ionization coefficient, a is the attachment coefficient (for example due to HCl), v_d is the electron drift velocity, and τ is the recombination coefficient. The for a gas discharge important situation, in which the electron density is constant, i.e., $dn_e/dt = 0$, is called the steady-state regime of the discharge, because here the electron losses are balanced by the production due to ionization. In this mode, the discharge sustains itself, which is associated to a, gas composition and pressure depending, electric field, which is called the steady-state field, U_{ss}.

However, without any external preionization of sufficient strength and spatial homogeneity, the initial electron density will be inhomogeneous and very low (only a few electrons/cm^3), originating only from natural processes, such as ionization by the cosmic background radiation. In this case, streamers are likely to form [38], since then the avalanches in the discharge volume are independent events with a random spatial distribution. Figure 2.4 shows schematically the formation of such a streamer in the electric field between two electrodes. As shown in Fig. 2.4(a), the electrons form a cloud that is drifting in the direction of the anode. An ionic tail is formed, because the ions with their larger mass move towards the cathode at a much lower speed than the electrons. Due to this charge separation, strong local electric fields of the order of the applied external electric field can develop. The high local field causes the emission of highly-energetic photons that photo-ionize the gas surrounding the charge cone from which more charge cones are formed, as shown in Fig. 2.4(b). The electrons continue to drift towards the anode and multiply, increasing the electron density in the head of the streamers, simultaneously, the ions move slowly in the direction of the cathode. With proceeding time, the gap between the electrodes will be bridged, as shown in Fig. 2.4(c). Once this occurs, the current will preferably flow through the channel

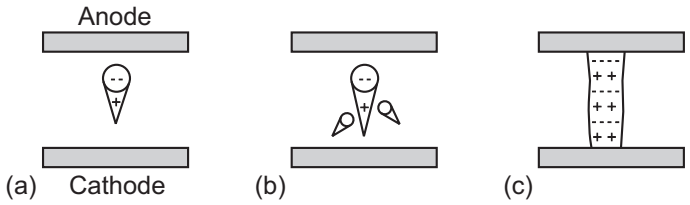

Figure 2.4: Schematic representation of the streamer development in a gas discharge. (a) Development of a charge cone in the electric field between the anode and cathode. (b) Charge cone collection due to the local electric field around the single cones. (c) Bridging of the electrode gap by the charged cloud.

formed by the streamer, but not through the remaining volume. Since the streamer dimensions are very small compared to the desired discharge volume, conversion from the electrical pump energy into excimer formation is very inefficient. Also, streamers conduct very high current densities that can accelerate the erosion of the electrode material.

To prevent the formation of streamers, the initial electron density, at the moment that the critical field strength for electron avalanches is applied, must be higher than a certain specific minimum electron density. It has been found that this lower limit of the electron density in a high-pressure excimer gas mixture is of the order of 10^7 cm^{-3}, depending on the rise time of the applied voltage [38]. The required density increases with the rise time of the applied voltage across the electrode gap and increasing gas pressure. The initial electron density can be supplied by preionization of the gas mixture (see also Chapter 4). In this case, when a large number of free electrons are generated in a homogeneously distributed manner in the discharge volume (see Fig. 2.5), the electrons drift in the electric field such that the avalanche heads start to overlap and homogeneously fill the volume between the electrodes. A high electric field leads to stronger electron multiplication, resulting in numerous charge cones, which overlap to create a homogeneous discharge. A short rise time prevents significant electron drift before the avalanche threshold is reached. If the rise time is not fast enough, an electron depleted layer is formed close to the cathode, which

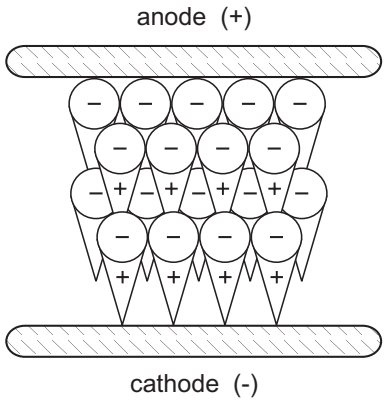

Figure 2.5: Schematic representation of the overlapping charge cones during the formative stage of the discharge.

forms streamers, thus, destroying the homogeneity of the electron distribution. Thus, preionization in combination with a very high and fast-rising electric field is a central precondition for initiating and maintaining a very homogeneous discharge [38].

In rare-gas halide mixtures, discharge instabilities have been found to be always present. The discharge homogeneity in these gas mixtures can decrease on a time scale of a few tens of nanoseconds even after a homogeneous formation. For this reason, it is important to find ways to at least reduce the rate at which instabilities evolve. A short overview of the physical processes which reduce the discharge homogeneity is given and possible solutions to prevent these are discussed in the following.

Inhomogeneities, such as filaments or arcs, develop due to local variations in the reaction kinetics. As was described in Sec. 2.3, electrons play a central role in the ionization and attachment processes in a gas discharge. For example, due to electron attachment, the halogen donor (e.g., F_2, HCl) is consumed during the discharge. A reaction channel that replenishes halogen donor molecules on the time scale of the discharge is missing. This lack of replenishment can lead to local halogen depletion [39, 40], which has been found to be an important mechanism causing the

formation of inhomogeneities in the glow of the discharge. Local halogen depletion can develop due to the close link between the dissociative attachment reaction and the electron density. Initially, a local enhancement of the electron density increases the number of attachment reactions, causing a faster reduction of the local halogen donor concentration. In turn, the number of attachment reactions decreases and the local electron density increases even further, creating a positive feedback loop for the current density. This feedback is sustained as the plasma resistivity reduces locally and carries a higher current compared to the surrounding plasma. In this way, thin, high-current channels can evolve, such as streamers or arcs. Consequently, the surrounding plasma is pumped insufficiently, with the result that the laser becomes less efficient or even stops oscillating, while the pumping current is still flowing.

The named spatial variations of the electron density are induced due to local inhomogeneities of the electric field. The cause can be an improper electrode design or surface roughness, causing field enhancements in the vicinity of the electrode edges or surface protrusions. The field enhancement and the current density are linked together in a positive feedback loop, comparable to the case of the local halogen donor depletion [41]. For this reason, much care has to be taken to achieve a uniform local electric field in the discharge volume and avoiding field enhancements close to the electrode surface. Protrusions on the cathode surface can lead to the formation of bright electrode spots, so-called hot spots [41–43], which predominantly sustain the discharge current. The electron density at such a hot spot is very high compared to the surrounding plasma, resulting in rapid depletion of the halogen donor in the vicinity of the hot spot. As a result of hot spot formation and the high current density, streamers develop, starting to grow into the bulk of the discharge until the anode-cathode gap is bridged. However, it has also been observed that a high number of small hot spots improves the discharge homogeneity compared to a low number of big hot spots, with the result that the discharge remains homogeneous for a longer time, because electric field distortions associated with the local electron density reduce. For the formation of small hot spots, several parameters have been found to be of importance [41–44]. Obviously, using a highly polished electrode surface reduces the number of large hot spots and rather favors the formation of a high number of

small hot spots. Additionally, reducing the rise time of the discharge current has been found to reduce the size of hot spots. A similar observation has been made for discharges with strong preionization with its resulting, highly dense and spatially homogeneous electron density. Also, the size of hot spots reduces, as the breakdown voltage is increased. This is thought to be due the presence of uniform overlapping charge cones, as discussed in the beginning of this section.

In conclusion, to sustain a homogeneous discharges over extended times in a high-pressure rare-gas halide mixture, highly polished electrodes are required, in combination with a strong preionization source, and a high breakdown voltage that is reached with a quickly rising voltage. The latter two conditions depend strongly on the electrical circuit used to pump the discharge, which will be outlined in the following chapter.

Chapter 3

Discharge excitation circuits

This chapter reviews excitation circuits employed in discharge pumped lasers. In particular, the efficiency and pulse duration of such lasers depends strongly on the discharge driving circuit. Reduction of the wavelength increases the pump power densities required to reach the threshold for lasing and particularly for excimer lasers, high excitation power densities of several MW cm^{-3} are required [4, 45]. This limits these lasers to the pulsed regime and puts considerable stress on the electrical circuit when operated with repetition rates of several kHz. A suitable pump circuit for excimer lasers provides the required power and deposits the stored energy into the discharge with low losses. Optimizing the laser efficiency was, and still is, subject of extensive study that has lead to various technological advances in the development of pump circuits [46]. High-pressure excimer gas discharges are initiated and sustained on a nanosecond time scale using voltages of several kV. Currents easily reach values of tens of kA. In addition, this requires switches well suited to switch and transport high currents with low losses and highly reliable for stable laser pumping. Furthermore, the lifetime of the switch becomes very important in high-repetition rate lasers and should extend over a billion of pulses.

We will show in the following that in order to deposit the pump energy with a high

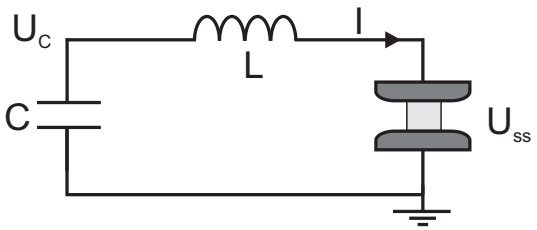

Figure 3.1: Basic discharge circuit scheme. C: storage capacitance, L: inductance, I: current, U_c: capacitor voltage, U_{ss}: discharge steady-state voltage.

efficiency into the gas discharge, the voltage of the discharge driving circuit has to be matched to the steady-state voltage of the discharge. This precondition can be derived from a very simple picture. A self-sustained discharge and its driving circuit can be modeled as an LC-circuit, as shown in Fig. 3.1. The current, flowing from the storage capacitance, C, through the inductance, L, of the circuit and the discharge is found by solving the differential equation for the circuit:

$$\frac{I}{C} + L\,\frac{d^2I}{dt^2} = 0, \tag{3.1}$$

where I is the discharge current at a time t. Initial conditions for the current are: $I(0) = 0$ for $t = 0$, and $dI/dt(0) = (U_c - U_{ss})/L$, where U_c is the capacitor voltage, and U_{ss} is the discharge steady-state voltage. Solving Eq. 3.1 with these initial conditions gives a periodic oscillating current:

$$\begin{aligned} I(t) &= I_{peak}\,\sin(t/\sqrt{LC}), \\ I_{peak} &= \sqrt{\frac{C}{L}}\,(U_c - U_{ss}), \end{aligned} \tag{3.2}$$

with an amplitude, I_{peak}, and a period of oscillation $T_I = 2\pi\sqrt{LC}$. The energy to pump the discharge must be deposited within the first half-cycle of the oscillation, because following oscillations do not contribute to the pumping of the laser discharge as inhomogeneities grow during the current and voltage reversal. Especially, the dis-

charge can constrict into an arc upon the current oscillation, damaging the electrode surface as thin plasma channels bridge the discharge volume while carrying several kA. This results in severe erosion at the electrode surface and reduces the lifetime of the discharge electrodes. Therefore, the highest efficiency of energy deposition is obtained when the current pulse consists of a single half-cycle. Calculation of the efficiency, η, under these circumstances yields:

$$\eta = \frac{\int_0^{T_I/2} U(t)I(t)dt}{E_{\text{stored}}} = \frac{4\,(U_{\text{c}} - U_{\text{ss}})}{U_{\text{c}}^2}, \tag{3.3}$$

where E_{stored} is the energy stored in the capacitance before the discharge. Evaluating Eq. 3.3, it can be shown that the highest efficiency is obtained when C is charged to a voltage $U_{\text{c}} = 2\,U_{\text{ss}}$. This condition is called the voltage-matching condition. Much effort has been spent on developing circuits that fulfill this condition. Note that the efficiency is only defined for $U_{\text{c}} \geq U_{\text{ss}}$, because a discharge will not be burning for lower values of U_{c} (non-self-sustained).

In this chapter, an overview of discharge circuits is given with emphasis on the efficiency and the voltage-matching condition. The first section is devoted to charge-transfer circuits. This circuit is popular in several industrial excimer lasers, as it is easy to realize and compact in its design. But it has several drawbacks, among which the inherent violation of the voltage-matching condition is the most severe, leading, as a consequence, to a limitation of the laser pulse duration to a few tens of nanoseconds. A different discharge excitation technique will be shown in Sec. 3.2, in which the prepulse-mainpulse circuit is introduced. This excitation technique has been proven to be suitable to sustain discharges over hundreds of nanoseconds. Two specific realizations of this circuit will be outlined in Sec. 3.2, motivating our choice of a excitation circuit for the pumping of the KrCl laser.

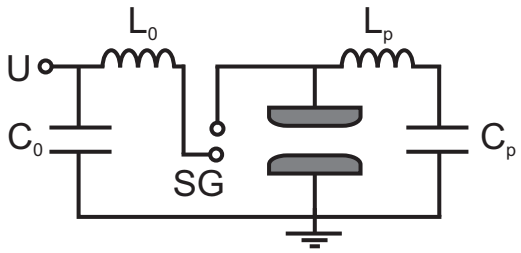

Figure 3.2: Charge-transfer circuit. C_0: transfer capacitance, L_0: circuit self-inductance, C_p: sustaining capacitance, L_p: discharge circuit self-inductance, SG: spark gap.

3.1 Charge-transfer circuit

The charge-transfer circuit [47–50] shown in Fig. 3.2 is the simplest excitation circuit used to pump a gas discharge laser. Here, the capacitance, C_0, is charged to a voltage, U, while being separated by a spark gap (SG) from the capacitance used to sustain the discharge, C_p, which is connected directly to the discharge electrodes. High peak powers can be achieved due to the small current loop of the circuit formed by L_p and C_p, where the inductance of L_p is almost fully given by the intrinsic inductance of the discharge cell. For example, C_p can be placed next to the electrodes inside the laser chamber. Discharge peak powers of several tens of MW cm^{-3} are realized this way.

In the following, we explain the initiation and sustainment of gas discharges employing this scheme and its limitations. During the time of charging, C_0 is electrically separated from C_p. This prevents spontaneous gas breakdown as the electric field across the discharge gap is zero and electron avalanches are suppressed. The spark gap, typically placed inside the laser vessel, consists of two electrodes and applying a high electric field across the electrodes results in breakdown that occurs within the electrode gap. This allows C_0 to transfer its charge to C_p. The voltage across the laser electrodes increases. However, to initiate the discharge, a voltage up to 4-6 U_{ss} has to be applied to the laser electrodes and C_p [38, 49]. Therefore, the voltage-matching

condition is violated. Even worse, it is impossible to fulfill the voltage-matching condition using this circuit, as the gas breakdown and sustainment is provided by the same circuit.

Many commercial short-pulse excimer lasers rely on this circuit, due to the robust and uncomplicated design. Tabletop-devices are available with repetition rates of several kHz. Improvements on the preionization of the gas have shown to increase the stability and efficiency somewhat [49, 50]. As an example, XeCl excimer lasers with an efficiency of 2.9% and a pulse width of 20 ns [49] have been demonstrated using charge-transfer circuits. Preionization is provided by the ultraviolet radiation emitted during the discharge in the spark gap, which is automatically synchronized with the voltage pulse. Nonetheless, the voltage-matching condition cannot be fulfilled, inducing current oscillatins, and laser pulse durations are limited to a few tens of nanoseconds. Furthermore, the spark gap suffers from erosion due to the high current density and pollutes the laser gas mixture during operation.

3.2 Prepulse-Mainpulse circuit

For the generation of stable discharges over a longer duration, the separation of the discharge initiating circuit and the sustaining circuit has been shown to be a successful approach [51]. The mutually excluding requirements for homogeneous initiation and sustaining are met independently this way. This scheme makes use of two circuits, the prepulse and the mainpulse circuit as shown in Fig. 3.3. First, the discharge volume must be preionized (see Ch.4), e.g., by irradiation with UV radiation, in order to generate a sufficiently high electron density according to the conditions presented in Ch.2. The prepulse capacitance, C_{pp}, contains only a few percent of the total circuit energy, typically 5% or less. Its purpose is to generate a high-voltage pulse, called a prepulse, to initiate breakdown of the laser gas. The prepulse rise time should be approximately 30-40 ns with a peak voltage of around 6-10 U_{ss}, which is achieved in a CLC-oscillation between C_{pp} and the peaking capacitance, C_{peak}. It increases the electron density from a pre-breakdown value of around 10^7 cm^{-3} to

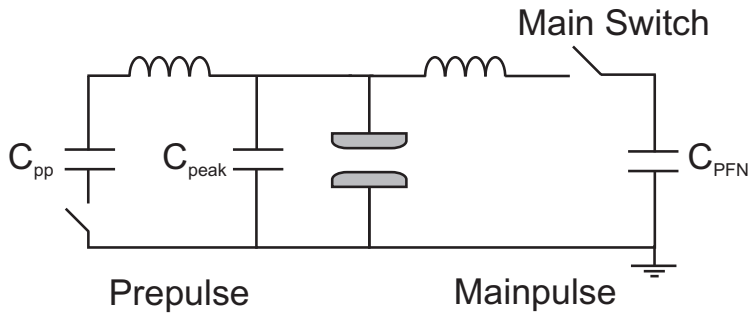

Figure 3.3: Basic prepulse-mainpulse circuit. C_{PFN}: capacitance of pulse forming network, C_{pp}: prepulse capacitor, C_{peak}: peaking capacitor.

more than 10^{14} cm^{-3}. The result is a very homogeneous gas breakdown and discharge initiation. The purpose of the mainpulse is to sustain the discharge after breakdown. Typically, the mainpulse is a low-impedance pulse forming network (PFN), consisting of several capacitors. Its total capacitance C_{PFN} is much larger than C_{peak} and contains the major fraction of the energy stored in both circuits. The mainpulse voltage is independent of the prepulse voltage and is therefore chosen to fulfill the voltage-matching condition.

A drawback of this circuit is the increased complexity, as it requires two high-voltage circuits and a separate preionization source. Furthermore, the impedance of the mainpulse is very low compared to the prepulse impedance. Therefore, a switch is necessary to separate both circuits before breakdown. This prevents the prepulse energy being discharged into the mainpulse circuit instead of initiating the discharge. The switch must meet several conditions: its self-inductance should be low, as this way a high discharge current can be achieved (see Eq. 3.2), and it must switch rapidly. After breakdown, the electron density begins to decay, as electron attachment and recombination takes place. To prevent the growth of discharge instabilities, the current from the PFN through the discharge has to be applied as fast as possible. Thus, the switching time must be very short. Furthermore, reliability and lifetime of the switch

are important parameters for high-repetition rate lasers.

Prepulse-mainpulse circuits have been shown to improve the efficiency of excimer lasers considerably [8, 52]. Also, this excitation scheme allows the laser to stay above threshold for longer time such that large increase in pulse duration is achieved [53], which can be used to generate spatially very coherent beams. The development of suitable switches is still an ongoing part of research related to excimer lasers. Two suitable methods to separate the circuits are discussed in the following sections.

3.2.1 Magnetic switches

Saturable magnetic inductor switches were found by Taylor et al. [51] to be efficient switches in a prepulse-mainpulse circuit. Here, a variable inductance is placed between both circuits. In its high-inductance state, it prevents charge from flowing out of the prepulse circuit and into the mainpulse capacitance. After breakdown, the inductance decreases due to the dynamics of the saturable inductor, with the result that the switch closes and the discharge can be sustained by the current from the PFN.

The dynamics of the inductor will be explained in more detail in the following. A schematic diagram of a saturable inductor is shown in Fig. 3.4. A conductor, connecting, e.g., the mainpulse with the discharge electrode, passes through the center of a toroidal core with the cross sectional area A. The inductance L_{core} of the toroid is given by:

$$L_{\mathrm{core}} = \frac{\mu\, N^2\, A}{l}, \tag{3.4}$$

where N is the number of windings, l is the mean path length of the magnetic field and μ is the magnetic permeability of the core. The magnetic permeability is given by $\mu = \mu_0\, \mu_r$, where μ_0 is the vacuum permeability and μ_r is the relative permeability. Since geometric factors remain constant, the dynamics of the switch, determined by L_{core}, are mainly dependent on the magnetic permeability, which is given by the slope $\partial B/\partial H$ in the hysteresis curve shown in Fig. 3.5, where B is the magnetic flux density and H is the magnetic field strength. Therefore, L_{core} is very large when the slope is

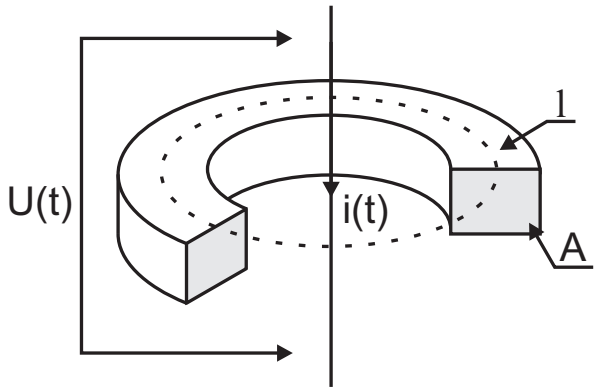

Figure 3.4: Schematic diagram of a saturable inductor switch. A: cross sectional area of the core, l: magnetic path length, i: current through the conductor, U: voltage difference.

very large and the inductor acts as an open switch. As shown in Fig. 3.5, the largest values for μ exist close to the remanent magnetic flux density B_r at low magnetic fields strengths. The closing of the switch proceeds by the following mechanism. Even though the switch is in a high inductance state for large values of L_{core}, it permits a small current to flow through the conductor, when a voltage $U(t)$ is applied across the core. This leak current, i, is given by:

$$\frac{di}{dt} = \frac{U(t)}{L_{\text{core}}}, \tag{3.5}$$

where $U(t)$ is the applied voltage across L_{core}. The magnetic field strength depends on the current:

$$H = \frac{N\, i(t)}{l}. \tag{3.6}$$

Therefore, the magnetic flux density increases from $-B_r$ as one follows the path along the hysteresis curve for increasing H until the flux density saturates at B_s. The inductance decreases rapidly as the magnetic permeability μ decreases. In the saturated state of the magnetic core, the switch is fully closed.

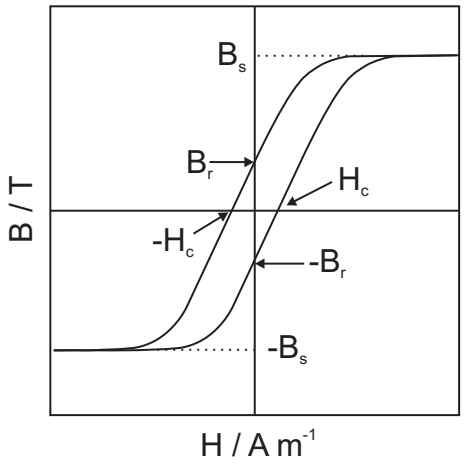

Figure 3.5: Schematic diagram of the hysteresis curve of a saturable inductor. B_s: saturation flux density, B_r: remanent magnetic flux density, H_c: coercive field strength.

Different excitation modes are possible in prepulse-mainpulse circuits switched by saturable magnetic inductors [54]. The modes are defined by the mainpulse and prepulse polarity and the voltage difference ($U_{\mathrm{pp}} - U_{\mathrm{pfn}}$). Four basic excitation modes using magnetic saturable inductors are possible: Diode mode, switch mode, charge mode, and resonant overshoot mode. In XeCl lasers, Gerritsen et al. obtained the highest efficiency of 5% when using the resonant overshoot mode [8].

Saturable magnetic inductors have been successfully implemented in many long-pulse lasers. Their lifetime is long, as they switch passively and do not suffer from erosion. XeCl lasers with pulse durations of up to 1 μs have been demonstrated [53]. Also, a KrCl laser with a pulse duration of 135 ns [55] was developed using a magnetic switch. Nonetheless, an inherent problem using magnetic elements is the self-inductance that remains after the magnetic core is driven into saturation, decreasing the possible peak current of the driving circuit as expressed by Eq. 3.5. Additionally, energy is dissipated due to the current required to drive the core into saturation, which can require up to 15% of the stored pump energy [56]. Therefore, prepulse-mainpulse

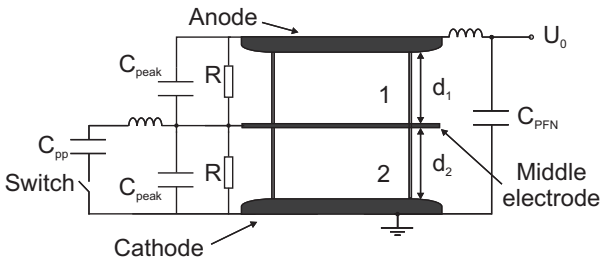

Figure 3.6: Three-electrode prepulse-mainpulse circuit. C_{PFN}: mainpulse capacitance, C_{peak}: peaking capacitance, C_{pp}: prepulse capacitance. d_1: upper volume electrode separation, d_2: lower volume electrode separation, R: resistor to define the middle electrode potential.

excitation circuits using alternative switches or exclude the use of switches have the potential to improve the efficiency of excimer lasers.

3.2.2 Three-electrode circuit

An interesting alternative for implementation in prepulse-mainpulse circuits, is the use of the discharge volume itself as switch instead of saturable magnetic inductors. A schematic overview of the circuit is shown in Fig. 3.6. In this scheme, a third electrode is placed between the two main electrodes of the discharge cell [57–60]. This divides the discharge cell into two volumes with electrode separations of d_1 and d_2. The mainpulse capacitance, C_{PFN}, is connected directly to the main electrodes. Thus, the circuit inductance is reduced to the inherent inductance of the PFN connection to the laser and of the laser head, L_{con}, itself. The middle electrode is connected electrically to the main electrodes via resistors, R, that define the middle electrode potential and peaking capacitors, C_{peak}, which are placed parallel to both volumes. The prepulse circuit is connected to the middle electrode and is thus separated from the mainpulse. The prepulse switch, shown in Fig. 3.6, is required to initiate the CLC-oscillation between C_{pp} and C_{peak} and is for this reason also present in prepulse circuits using magnetic switches. Therefore, the switch does not introduce extra energy losses in a

three-electrode circuit compared to circuits utilizing saturable inductors.

The breakdown modes in a three-electrode circuit depend, similar to circuits using magnetic switches, on the difference between the voltage amplitudes and the voltage polarities of prepulse and mainpulse, which can be chosen independently because two independent circuits are employed. In a three-electrode circuit, this is complicated by the presence of two volumes. In general, two breakdown modes are possible: consecutive breakdown and simultaneous breakdown. Both will be described in more detail in the following.

Consecutive breakdown

A consecutive breakdown is realized in a three-electrode discharge cell, when the breakdown field strength in one volume is reached earlier than in the second volume [56, 58, 61]. This is for example the case, when equal electrode separations ($d_1 = d_2$) are chosen, as shown in Fig. 3.6.

We will explain this mode by a qualitative example of the voltage across both volumes for a mainpulse with positive polarity and a prepulse with negative polarity. This situation is shown in Fig. 3.7. The mainpulse capacitance C_{PFN} is connected directly to the discharge cell and is charged to a voltage $U_0 = 2U_{\mathrm{ss}}$ before initiating the discharge. U_1 and U_2 are the potential differences in volume 1 and 2, respectively, where $U_0 = U_1 + U_2$. Before applying preionization, $U_1 = U_2 = U_0/2$. After charging C_{PFN}, both discharge volumes are preionized and the prepulse is applied to the middle electrode. The prepulse voltage is generated by switching a dc-charged capacitance, C_{pp}, to ground, causing the charge to be transferred from C_{pp} to C_{peak}, resulting in a decrease of the voltage across volume 2, while the voltage across volume 1 increases. Due to the initial positive voltage across volume 1 in combination with the increasing voltage, the breakdown threshold $U_{\mathrm{br},1}$ is reached earlier compared to volume 2, where the voltage first reduces. As the discharge is initiated in volume 1, charge is transferred between C_{PFN} and C_{peak}, causing a voltage oscillation across volume 2, which increases the voltage U_2 such that the breakdown threshold $U_{\mathrm{br},2}$ is reached. As a result, both

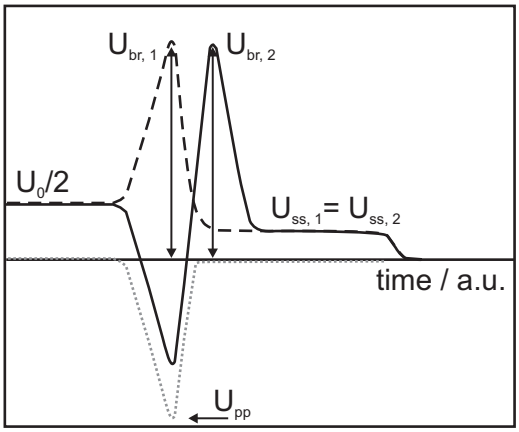

Figure 3.7: Qualitative time development of the voltage in volume 1 and volume 2 with consecutive discharge initiation. (solid line): voltage U_1 across volume 1, (dashed line): voltage U_2 across volume 2. U_0: PFN charging voltage, U_{pp} (dotted line): prepulse voltage, $U_{\mathrm{br},1}$, $U_{\mathrm{br},2}$: breakdown voltage and $U_{\mathrm{ss},1}$, $U_{\mathrm{ss},2}$: steady-state voltage in volume 1 and 2, respectively.

discharges are initiated and the voltage across d_1 and d_2 reduces to the discharge steady-state voltage $U_{\mathrm{ss}} = U_{\mathrm{ss},1} = U_{\mathrm{ss},2}$.

Advantage of this breakdown mode is in first place the simplicity of implementation, as it takes place automatically in a symmetric three-electrode configuration. Furthermore, in a laser both volumes generate equally sized laser beams. This discharge mode is successfully employed in long-pulse XeCl lasers, reaching efficiencies of 2.8% [58]. A drawback, however, is the time delay between the breakdowns in both volumes, because it has been found that a small current preceding the main discharge current in the first ignited volume leads to deviations of the spatial electron density profile [61]. This can lead to a local depletion of the halogen donor already before the discharge is fully established in both volumes, reducing the stability of the discharge and, therewith, the achievable laser pulse duration. Furthermore, the current direction changes due to the voltage reversal, strongly modulating the pump power in the early stage of the discharge, which can lead to the formation of instabilities.

Simultaneous breakdown

To increase the discharge stability, it seems advantageous to reduce or even prevent the time delay between the breakdown in both volumes. In the ideal situation this can be achieved if the breakdown takes place in both volumes simultaneously, which requires that the breakdown field strength in both volumes is reached at the same time. In the three-electrode configuration, both volumes are filled to the same gas pressure, p, so the breakdown field strength in both volumes is equal and given according to:

$$E_{\mathrm{br}} = \frac{U_{\mathrm{br},1}}{d_1} = \frac{U_{\mathrm{br},2}}{d_2}, \tag{3.7}$$

where E_{br} is the breakdown field strength of the gas mixture and $U_{\mathrm{br},1}$ and $U_{\mathrm{br},2}$ are the breakdown voltages associated to the electrode separation d_1 and d_2, respectively. The field strength scales with pd, where d is the electrode separation. As will be shown in the following, the electrode separations have to be unequal in order to simultaneously reach the breakdown field strength. For a better understanding,

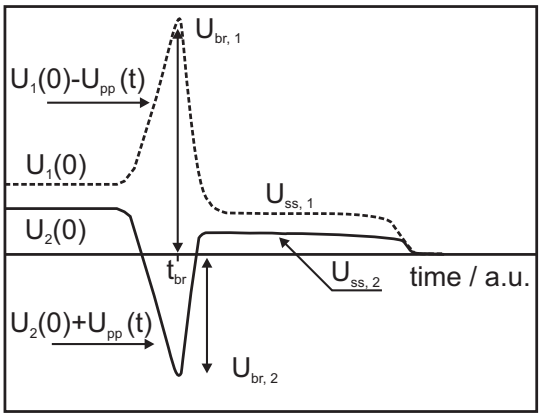

Figure 3.8: Qualitative time development of the voltage U_1 in volume 1 and U_2 in volume 2 in a three-electrode configuration with $d_1 > d_2$. $U_{\mathrm{br},1}$, $U_{\mathrm{br},2}$: breakdown voltage and $U_{\mathrm{ss},1}$, $U_{\mathrm{ss},2}$: steady state voltage in volume 1 and 2, respectively, U_{pp}: prepulse voltage

Fig. 3.8 shows the expected time development of the voltage in an asymmetric three-electrode system ($d_1 > d_2$) with simultaneous breakdown. Here, the PFN is charged with a positive voltage, while a prepulse with negative voltage is applied. U_1 and U_2 are the voltages across the electrode separations d_1 and d_2, respectively (with the anode-cathode separation $d_{\mathrm{tot}} = d_1 + d_2$). When the PFN is charged, before the preionization and prepulse are applied, the voltage across the volumes is given by the ratio of the impedances Z_1 and Z_2:

$$U_1/U_2 = Z_1/Z_2, \tag{3.8}$$

where Z_1 and Z_2 are given by the capacitances and resistors connected in parallel to the respective volumes. An efficient energy transfer into the discharge requires $U_0 = 2U_{\mathrm{ss}}$. The steady-state field in both discharge volumes is equal, thus, the

steady-state voltage in both volumes is given by their electrode separations:

$$E_{\mathrm{ss}} = \frac{U_{\mathrm{ss}}}{d_{\mathrm{tot}}} = \frac{U_{\mathrm{ss},1}}{d_1} = \frac{U_{\mathrm{ss},2}}{d_2}\,. \tag{3.9}$$

Moreover, the temporal dependence of the electric field in volume 1 and 2 before breakdown is given by the sum respectively difference of the mainpulse and prepulse voltage (see Fig. 3.8):

$$\begin{aligned} E_1(t) &= \frac{U_1(t)}{d_1} = \frac{U_1(0) - U_{\mathrm{pp}}(t)}{d_1}, \\ E_2(t) &= \frac{U_2(t)}{d_2} = \frac{U_2(0) + U_{\mathrm{pp}}(t)}{d_2}, \end{aligned} \tag{3.10}$$

where $U_{\mathrm{pp}}(t)$ is the prepulse voltage as a function of time and $U_1(0) = 2\,U_{\mathrm{ss},1}$, and $U_2(0) = 2\,U_{\mathrm{ss},2}$ are the voltages across the electrode gaps before the application of the prepulse. In the following, U_{pp} denotes the peak voltage of the prepulse as shown in Fig. 3.7 for which the breakdown threshold is expected to be reached. For the desired simultaneous breakdown, the breakdown field strength in both volumes has to be reached at the same time ($t = t_{\mathrm{br}}$). Taking into account that the voltage polarity in volume 1 is opposite to the one in volume 2, we obtain the condition:

$$|E_1(t_{\mathrm{br}})| = |E_2(t_{\mathrm{br}})|\,. \tag{3.11}$$

It becomes clear from Eq. 3.10 and condition 3.11, why the simultaneous breakdown in a symmetric three-electrode configuration ($d_1 = d_2$) is hindered. As an example, for the situation shown in Fig. 3.7 ($U_{\mathrm{pp}} < 0$ and $U_{1,\,2}(0) > 0$), the electric field in volume 1 will be different at all times from the electric field in volume 2. Therefore, reaching at the same time the breakdown field strength is only possible, if $U_1(0) = U_2(0) = 0$ and, thus, only when the PFN is not charged. We confirmed this result in experiments.

To determine the required electrode separation for a simultaneous breakdown, we will derive in the following an expression for d_1 for a predefined electrode separation d_{tot} of

the discharge cell. As a precondition, the steady-state field, E_{ss}, and the breakdown field strength, E_{br}, have to be known. Furthermore, the thickness of the middle electrode is assumed to be much smaller than the electrode separations in order to be able to neglect its dimension. The derivation is carried out for the situation shown in Fig. 3.8, i.e., $U_{\mathrm{pp}} < 0$, $U_{1,\,2}(0) > 0$, and $\left|U_{\mathrm{pp}}\right| > U_{1,\,2}(0)$. Starting from Eq. 3.10 and taking the polarities into account, we can write condition 3.11 in the following form:

$$\frac{U_{\mathrm{br},1}}{d_1} = -\frac{U_{\mathrm{br},2}}{d_2}. \tag{3.12}$$

Resolving this equation for d_1, while substituting $U_{\mathrm{br},1} = 2E_{\mathrm{ss}}d_1 - U_{\mathrm{pp}}$ and $U_{\mathrm{pp}} = -d_2(E_{\mathrm{br}} + 2E_{\mathrm{ss}})$, we derive following expression for the upper electrode separation:

$$d_1 = d_2\frac{E_{\mathrm{br}} + 2E_{\mathrm{ss}}}{E_{\mathrm{br}} - 2E_{\mathrm{ss}}}. \tag{3.13}$$

Finally, replacing $d_2 = d_{\mathrm{tot}} - d_1$, we obtain as result:

$$d_1 = d_{\mathrm{tot}}\frac{E_{\mathrm{br}} + E_{\mathrm{ss}}}{2E_{\mathrm{br}}}. \tag{3.14}$$

To give an example, for a KrCl gas mixture at a pressure of 4 bar, a steady-state field of $E_{\mathrm{ss}} = 1.5$ kV cm^{-1} and $E_{\mathrm{br}} = 13$ kV cm^{-1} has been measured [55]. Then, choosing $d_{\mathrm{tot}} = 2.6$ cm, we obtain an electrode separation of $d_2 = 1$ cm and, therefore, $d_1 = 1.6$ cm. Summarizing, if E_{ss} and E_{br} are known (from literature or experiments), and d_{tot} is chosen, the derived expression Eq. 3.14 allows us to calculate the required electrode distance, in order to realize the simultaneous breakdown. Similar expressions for d_1 can be derived for other voltage polarities than the ones taken as a precondition following from Fig. 3.8. This way, the electrode separation can be calculated for various configurations.

Evaluating Eq. 3.14, we see that for a very large breakdown field strength, $E_{\mathrm{br}} \gg E_{\mathrm{ss}}$, the electrode separation of both volumes becomes equal. Such a high breakdown field strength can only be reached when an extremely fast rising prepulse voltages is applied. However, in large discharge lasers, the self-inductance of the prepulse circuit

and laser head limit the rise time and only by using different electrode separations the simultaneous breakdown can be realized.

As concluding remark, simultaneous breakdown has the potential to improve the discharge quality and, thus, the laser efficiency. Bollanti et al. have demonstrated with this breakdown mode a long-pulse XeCl laser with an efficiency of 3% [59].

Summarizing, three-electrode discharge circuits are very interesting for excimer lasers, where the power deposition requirements are very demanding, such as KrF or KrCl lasers. The elimination of the magnetic switch allows one to build very compact mainpulse circuits, thus reaching high excitation rates. Energy dissipation in the switch is avoided and, thus, higher electrical efficiencies are expected compared to circuits using saturable inductors. For these reasons, we focused the research on developing a three-electrode discharge excitation circuit to pump a long-pulse KrCl laser.

Chapter 4

A low-inductive three-electrode discharge test system

The generation of self-sustained discharges in high-pressure excimer laser gases with long pulse durations with the goal to generate laser beams with a high spatial coherence is a technological challenge. Much effort is spend to develop techniques which suppress the inherent growth of discharge instabilities. Efficient long-pulse discharge systems have in common that they employ (a) a preionization source, (b) a prepulse to initiate the discharge, and (c) a mainpulse to sustain the discharge. In this chapter, we present the design and experimental results of a long-pulse KrCl discharge system, successfully incorporating these three techniques in a compact three-electrode excitation circuit.

In contrast to XeCl lasers, the information available on long-pulse KrCl discharge lasers is very scarce. Besides a study of Hueber et al. [55], no additional information concerning long-pulse KrCl lasers is reported. For this reason, we developed a

discharge test-cell, which will be presented in this chapter. The test-cell was used to observe the basic discharge properties of KrCl discharges, i.e., peak current, steady-state voltage, and stability of the homogeneous glow. These were compared with results from XeCl discharge experiments, for which a vast amount of information is available and, therefore, can be used for reference.

Because HCl is also used as halogen donor in KrCl discharges, the dynamics concerning the electron attachment (to HCl) are expected to be comparable to XeCl discharges. Instabilities due to local halogen depletion (see Sec. 2.4 and Ref. 40) are considered to develop on similar time scales. On the other hand, much higher rare-gas pressures are used in KrCl lasers when compared to XeCl lasers, which will change the overall KrCl discharge dynamics. In particular, the question on how far the stability time of KrCl discharges can be extended has been left unanswered so far.

In this chapter, we present the successful generation of KrCl discharges with a long duration of the homogeneous glow, employing the three-electrode discharge excitation circuit. Introducing the experimental set-up, we first describe the X-ray source, which was used to preionize the gas mixture and which is a crucial element to form a homogeneous discharge. This is followed by the description of the three-electrode discharge cell, which was developed to observe the discharge development under optimum pumping conditions, i.e., short current rise time (< 20 ns) and short prepulse rise time (≈ 30 ns). The experiments were carried out observing high-pressure XeCl and KrCl discharges, employing the consecutive and simultaneous breakdown. Investigating in particular the simultaneous breakdown, images taken with a fast gated ICCD camera revealed the temporal and spatial development of the discharge stability under various pump conditions and gas compositions. From these experiments, conclusions are drawn for the design of a large-scale long-pulse KrCl excimer laser.

4.1 The X-ray source

The generation of a stable discharge in excimer gas mixtures requires preionization of the gas. Before the application of the discharge initiating voltage, a minimum electron density in the order of $10^6 - 10^8$ cm^{-3} has to be present in the gas [38]. Various preionization techniques are known. The most commonly applied technique in self-sustained discharge excimer lasers is photo-ionization of the gas volume using ultraviolet [44] or X-ray radiation [62]. Less attention has been given to techniques using for example α-particles or neutrons as these require severe radiation protection and are, thus, not applicable for compact high-repetition rate lasers.

Ultraviolet radiation is produced using for example spark plug arrays. For industrial systems with a large discharge cross section, this technique is not suitable, because the penetration depth of the UV-photons into the gas volume is not large enough to provide a sufficient and homogeneous preionization. Furthermore, the UV-source has to be placed inside the laser chamber, leading to pollution of the laser gas due to erosion of the spark plugs, which reduces the gas lifetime. X-ray photo-ionization on the other hand has the advantage to preionize large scale volumes, due to the large penetration depth of X-rays in gas. The X-ray source can be placed outside the laser chamber, and X-rays can be coupled in through a thin metal window, thus, avoiding pollution of the laser vessel. Even more, X-rays offer the possibility to define the cross section of the preionized volume by using X-ray absorbing masks [63] that collimate the X-ray beam. X-ray preionization has proven to be suitable in high-repetition rate operation of excimer lasers up to several kHz [64]. Disadvantages arising from X-ray sources are the additional safety requirements. One has to provide appropriate shielding for the X-ray source and for the required high-voltage circuit.

In the following, the generation of X-rays is briefly outlined. The X-ray generation is based on the production of Bremsstrahlung by decelerating electrons in a target with a high atomic number (Z). First, electrons are produced and gain energy in an accelerating potential, U_{acc}. The maximum kinetic energy electrons can gain during acceleration is given by eU_{acc}, where e is the elementary charge. As electrons

hit the target on the anode, they lose kinetic energy due to scattering within the target material. The efficiency of the energy conversion can be approximated using $\eta = ZE_{\max}/700$, where $E_{\max} = eU_{\mathrm{acc}}$ is the maximum kinetic electron energy, given in units of MeV [65]. The Bremsstrahlung spectrum is a continuum with a mean value of the distribution at around $eU_{\mathrm{acc}}/2$ [66]. Next to the continuous Bremsstrahlung spectrum, material specific lines are present in the energy spectrum due to K-shell transitions in the atoms. In experiments employing X-ray preionization of excimer lasers, energies between 50 keV and 200 keV have been found to be sufficient to provide the necessary preionization electron density [62]. With respect to the mean energy in the spectrum, acceleration voltages of more than 100 kV are required.

The dependence of the X-ray intensity on the accelerating voltage will be outlined in the following. The intensity $I(\epsilon)$ in an energy interval $(E, E + \delta E)$ of the X-ray energy spectrum is given according to Kramers [67] by:

$$I(E) = C\, J\, Z\, (eU_{\mathrm{acc}} - E), \tag{4.1}$$

with C being a constant, J the current density in the vacuum gap, which is accelerated in the potential U_{acc} towards the anode, hitting the target with atomic number Z. Then, the total emitted intensity follows from integrating Eq. 4.1:

$$I_{\mathrm{tot}} = \int_0^{eU_{\mathrm{acc}}} I(E)\, dE \propto J\, (eU_{\mathrm{acc}})^2. \tag{4.2}$$

The current density J is space charge limited and, as described by the Child-Langmuir law, given by:

$$J = \frac{4}{9}\, \epsilon_0 \sqrt{\frac{2e}{m_e}}\, d^{-2}\, (eU_{\mathrm{acc}})^{3/2}, \tag{4.3}$$

where m_e is the electron mass and d is the distance between the cathode and the anode. Substituting Eq. 4.3 into Eq. 4.2 shows that $I_{\mathrm{tot}} \propto (eU_{\mathrm{acc}})^{7/2}$.

In our experiments, the X-ray generation is based on the deceleration of electrons

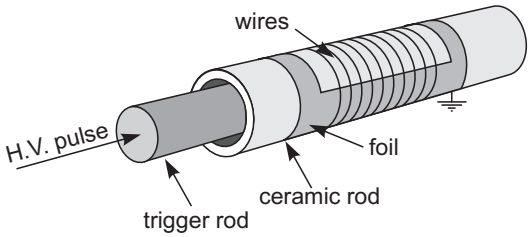

Figure 4.1: Scheme of a corona plasma cathode.

produced by a corona plasma cathode [68]. Such a cathode is shown schematically in Fig. 4.1. Similar sources using corona plasma cathodes were employed in experiments on XeCl [68, 69], ArF [34] and F_2 lasers [70]. In our X-ray source, the corona plasma cathode consists of a ceramic cylinder with a length of 90 cm, an outer diameter of 10 mm and a wall thickness of 1.5 mm. The cylinder is covered partially with brass foil (50 μm thickness) in which a rectangular window is cut. The foil window points toward the anode. The foil is wound tightly to the ceramic rod with a 0.1 mm thick tungsten wire. Both, foil and wire are on ground potential. A trigger rod, made of copper, is inserted into the ceramic rod. A fast rising high-voltage pulse is applied to the trigger rod, resulting in the field-emission of electrons from the wire due to electric field enhancements in the vicinity of the wire. Due to the voltage difference between trigger rod and the ceramic, these electrons impinge on the ceramic surface, creating a plasma. From this plasma, using a voltage difference between the anode and cathode, electrons are extracted and accelerated towards the anode.

A schematic overview of the X-ray source is given in Fig 4.2. The high-voltage electrodes (anode and cathode) are placed inside a vacuum chamber. Efficient plasma production requires pressures inside the chamber in the order of 10^{-6} mbar. While a maximum accelerating voltage of 140 kV is applied between the anode and cathode, a voltage of 20 kV is applied to the trigger rod. Tantalum ($Z = 73$) is used as target material and covers the anode. Using these values, an X-ray production efficiency of $\eta = 1.5\%$ and a mean energy of 70 keV is estimated for the source. The X-rays pass

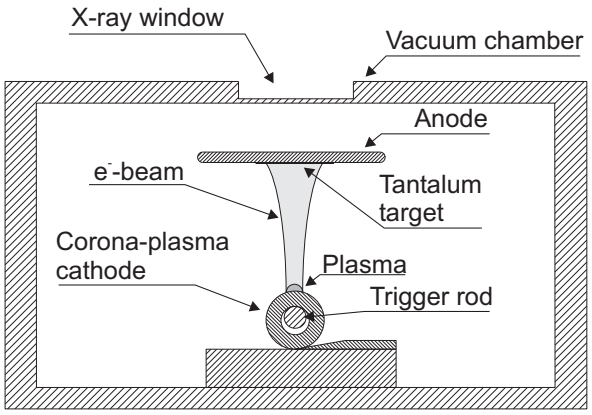

Figure 4.2: Schematic overview of the pulsed X-ray source based on the corona plasma cathode.

through a 1 mm thick window in the vacuum chamber with a cross section of 2×2 cm^2. Almost all photons with energies below 30 keV are absorbed in the material of the window, as the cross section for photon-absorption increases rapidly for such photon energies [71].

The electric circuit of the X-ray source is shown schematically in Fig. 4.3. The energy of the trigger pulse and the energy used to generate the accelerating pulse is stored in the capacitance C_p, which is charged to voltages of up to 15 kV, and is connected to the primary side of a voltage transformer (4:70). To initiate the X-ray generation, a high-voltage switch (S), e.g., a thyratron, is closed and charge flows through the transformer. This results on the secondary side of the transformer in the generation of anode-cathode voltages of up to 140 kV. Additionally, to form the trigger pulse, the capacitance C_d is charged to a lower voltage, employing a lower transformer ratio (4:10). In order to generate the peak electron density of the plasma when the maximum acceleration voltage is reached, both pulses have to be temporally synchronized. For this reason, a delay line is used for the trigger pulse, which is realized by preventing charge to flow from C_d to the trigger rod by inserting a

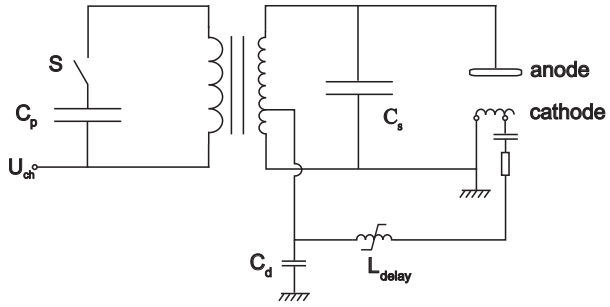

Figure 4.3: Schematic overview of the electric circuit of the short pulse X-ray source. C_p: primary capacitance, C_s: stray capacitance, C_d: trigger pulse capacitance, L_{delay}: delay line and pulse sharpening circuit.

saturable inductance L_{delay} in the trigger circuit. On a predefined moment, when the accelerating voltage reaches its peak value, the inductance decreases and the trigger pulse is generated. Using such a circuit allows the generation of intense X-ray pulses with a short duration (< 30 ns), which will be shown below.

Shown in Fig. 4.4 is a typical example of the temporal pulse shape of an X-ray pulse generated with the presented source. The pulse shape is followed using a fast responding plastic scintillator with a rise time of less than 1 ns (decay time 2.4 ns). The scintillator converts the absorbed X-ray energy into an optical signal that is transmitted via a plastic fiber to a photomultiplier tube (rise time 1.9 ns) and recorded with a digital oscilloscope. As can be seen in Fig. 4.4, the rise time of the X-ray pulse, defined as the time difference between the 10% and 90% value of the peak signal, is 18 ns with a pulse-width (FWHM) of 20 ns.

In order to determine the maximum dose, which is defined as the absorbed X-ray energy per unit of mass, in the discharge volume that can be achieved with the X-ray source, we measured the X-ray dose as a function of U_{ch}. Because $U_{\mathrm{acc}} \propto U_{\mathrm{ch}}$, we can investigate this way the dependence of the dose on the accelerating voltage. We used a pen-dosimeter to measure the dose, which is, in contrast to the scintillator, a calibrated detector that allows a comparison with other sources [34, 68, 70].

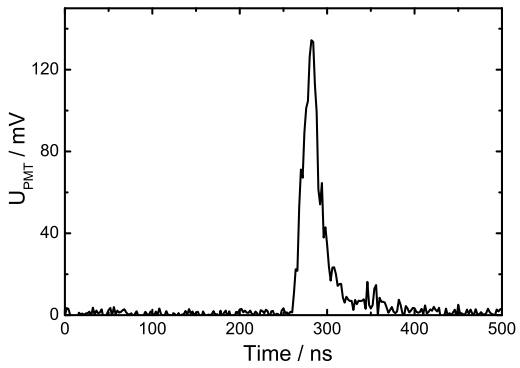

Figure 4.4: Typical waveform of the X-ray power measured with a fast responding plastic scintillator.

The X-ray dose was measured inside the discharge test-cell on top of the X-ray window in the bottom electrode for several pulses and the average dose per pulse was calculated. Shown in Fig. 4.5 is the result of this measurement. As a result, we find that the dose increases proportional to $U_{\mathrm{ch}}^{7/2}$. Such a dependence is expected from Eq. 4.2 and Eq. 4.3, because a higher accelerating voltage leads to a higher intensity, which in turn will increase the dose.

In a further experiment, the dependence of the X-ray dose on the distance to the source was investigated to determine the change of the dose at different positions inside the discharge cell. For this, we increased the distance at which the dose was measured with respect to the source. As a result, we observed that the X-ray dose scales proportional to $1/r^2$, where r is the distance of the pen-dosimeter to the source. This point-source like decrease is caused due to the small size of the X-ray window compared to the distance of the detector to the source.

Summarizing, we measured an X-ray dose of more than 1 mRad for a pulse duration of 18 ns. It is expected from measurements on XeCl lasers [69, 72], that such a combination of dose and short pulse duration represents a sufficiently high X-ray intensity to preionize chlorine based excimer lasers in order to generate an electron

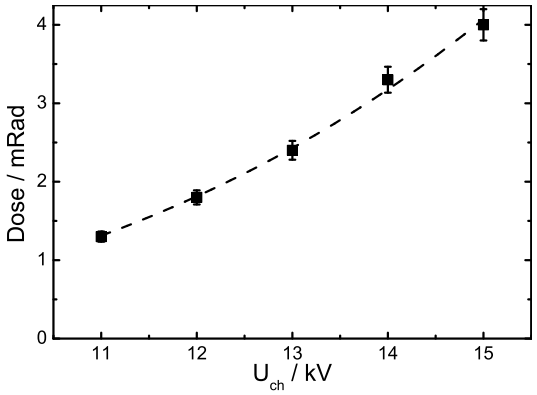

Figure 4.5: Averaged X-ray dose measured with a pen dosimeter as function of the X-ray source charging voltage U_{ch}. (- -): fitted function $\propto U_{\mathrm{ch}}^{7/2}$.

density of $10^6 - 10^7$ cm^{-3}.

4.2 Experimental set-up

For the realization of a discharge pumped KrCl excimer laser, we applied the three-electrode prepulse-mainpulse excitation technique which allows high-power pumping with a low inductive circuit. The development of such a laser with a large discharge volume requires the optimization of the geometric configuration and excitation circuit. In order to determine the optimum parameter range, we developed first a small test set-up. A scheme of the three-electrode discharge set-up and the connected electric circuit is shown in Fig. 4.6. The discharge cell consists of two volumes (labeled 1 and 2) that are formed using three electrodes. The volumes are preionized using the presented X-ray source. The radiation penetrates the cathode through a window of 2×2 cm^2, defining also the discharge cross section. The pulse forming network (C_{PFN}) is connected to the anode and cathode and is charged to a voltage of U_0 before the discharge. The prepulse capacitance, C_{pp}, is connected to the middle electrode in

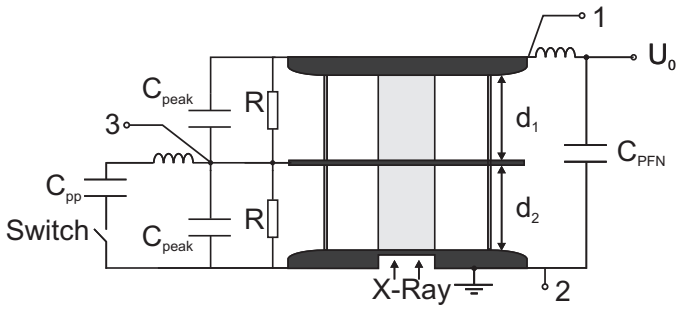

Figure 4.6: Schematic representation of the three-electrode mainpulse-prepulse circuit and discharge cell. C_{PFN}: PFN capacitance, C_{peak}: peaking capacitance, C_{pp}: prepulse capacitance. U_0: PFN charging voltage, U_{pc}: prepulse charging voltage, 1,3*: voltage probe position,* 2*: current probe position, R: resistor.*

order to generate a high-voltage pulse in a CLC oscillation with C_{peak}. The prepulse capacitance is charged to a voltage U_{pc} before the switch is closed. Resistors, R, are used to define the middle electrode potential.

Also shown in Fig. 4.6 are the probe positions we used to measure the discharge voltage and current. Calibrated resistive voltage-divider probes were connected at positions 1 and 3 in order to measure the anode-cathode voltage and the middle electrode-cathode voltage, respectively. In the data analysis, the signals from the voltage probes were corrected for inductive effects due to the laser head self-inductance, L_{head}:

$$U(t) = U_{\mathrm{sig}}(t) - L_{\mathrm{head}}\frac{dI}{dt}, \tag{4.4}$$

where $U(t)$ is the corrected voltage, $U_{\mathrm{sig}}(t)$ is the measured voltage and I the discharge current. A Rogowsky coil or a low-ohmic shunt-resistor probe placed at position 2 was used to measure the current from the PFN through the discharge.

The components used to construct the three-electrode discharge test-cell are shown in Fig. 4.7. The anode and cathode are plane aluminum electrodes. Since aluminum exposed to HCl corrodes, both electrodes were Ni-coated. The choice to use Ni is

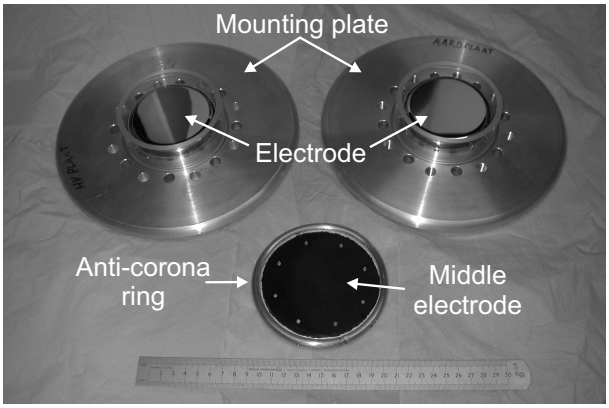

Figure 4.7: Picture of the discharge cell components. Left and right side: mounting plates with anode and cathode in the center part. Center: middle electrode with anti-corona ring.

motivated due to its high inertness with respect to HCl as well as its high melting temperature, preventing a damage of the electrode surface in case an arc discharge might occur with its associated high current densities. The electrodes have a diameter of 8 cm and are mounted to aluminum plates, suitable to withstand a gas pressures of 5 bar. The middle electrode, shown in the center, is a 1 mm thick Ni-coated flat aluminum plate. Holes in the plate ensure the pressure equalization between both volumes. To prevent flash-overs outside the cell along the insulator that might start from the sharp edge of the plate, an anti-corona ring made of copper is mounted to the perimeter of the middle electrode, reducing the field strength. All electrode surfaces are polished to ensure a very homogeneous electric field in the discharge volume with an electric field variation of less than 0.2%.

The discharge volumes and the electrode separations are defined by using electric insulators made of a polymer (Perspex). The electrode separations can be changed by inserting insulators of different heights, in order to study the two breakdown modes possible using the three-electrode excitation scheme.

4.3 Experimental results

This section presents the experimental results on current and voltage measurements obtained with the three-electrode discharge test set-up. We carried out the experiments with an emphasis on the observation of the stability of KrCl discharges, since this determines the laser pulse duration that can be achieved. In order to identify the dependence of the discharge stability on the halogen and rare-gas concentration, several gas compositions were employed.

4.3.1 Electric characteristics

Consecutive breakdown

In order to determine the breakdown field strength and the steady-state voltage of a KrCl gas mixture, we firstly measured the electric discharge characteristics, i.e., voltage and current, in the consecutive breakdown mode for a gas composition of HCl/Kr/Ne with partial pressures of (1.3/60/4940) mbar. Equal electrode separations were chosen ($d_1 = d_2 = 1$ cm). We estimated from the presented waveforms in Ref. 55 for an electrode separation of 2 cm and a gas pressure of 5 bar a steady-state voltage of 4 kV. For this reason, the PFN capacitance ($C_{\mathrm{PFN}} = 8$ nF) was charged to a voltage of ≈ 8 kV. The prepulse was generated by a capacitor ($C_{\mathrm{pp}} = 0.2$ nF) mounted on a N_2-pressurized spark-gap, that was connected to the middle electrode in order to charge the peaking capacitance $C_{\mathrm{peak}} = 0.1$ nF.

Using this configuration, we measured the middle electrode voltage, U_{mid} (solid line), and the discharge current, I_{d} (dotted line). A typical example of the measured waveforms is shown in Fig. 4.8. Between $t = 0$ ns and $t = 170$ ns, the PFN is slowly pulse charged, resulting due to the use of potential defining resistors parallel to the volumes in a voltage of 4 kV at the middle electrode. At $t \approx 150$ ns, the preionization pulse (not shown) is applied, which is followed at $t \approx 180$ ns by the application of the prepulse. The prepulse ($U_{\mathrm{pp}} = -14$ kV) increases the voltage across volume 2 from 4 kV to -10 kV in 30 ns. The negative peak voltage marks the moment of

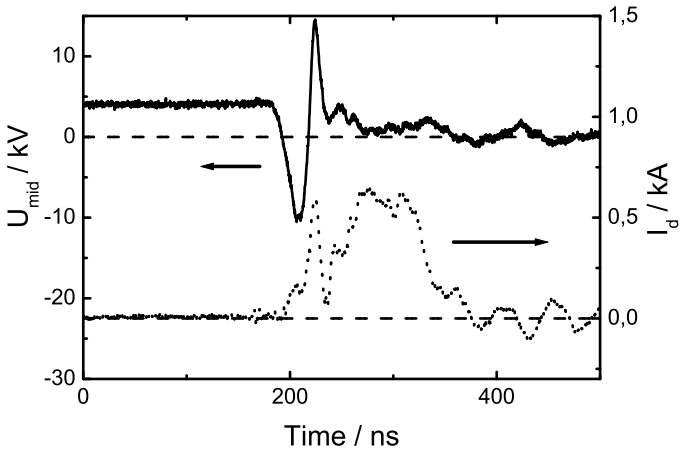

Figure 4.8: Typical example of the middle electrode voltage (solid) and discharge current (dotted) for the consecutive breakdown, using a gas mixture of HCl/Kr/Ne (1.3/60/4940) mbar.

breakdown in volume 1, causing a current between C_{peak} and C_{PFN}. This results in the current signal in the observed peak at $t \approx 220$ ns with an amplitude of 580 A. After breakdown in the first volume, we observe a voltage reversal and an increase in 20 ns to a voltage of 14 kV. The observed reduction of the voltage rise time from 30 ns to 20 ns is caused by the lower self-inductance of the current loop between the discharge volume and the peaking capacitance when compared to the peaking circuit self-inductance (C_{peak} and C_{pp}). As a result of the reduced voltage rise time, the breakdown voltage increases [38]. At a voltage of 14 kV, the breakdown threshold in volume 2 is reached and as the discharge is formed, the voltage reduces to its steady-state value of approximately 1.3 kV. After both discharges are initiated, the PFN sustains the discharge. The discharge current starts at $t = 230$ ns and reaches a peak value of 620 A, having a pulse duration of 80 ns (FWHM).

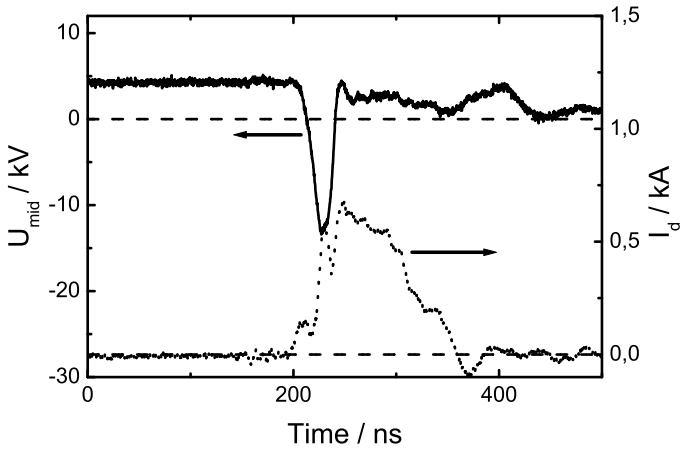

Figure 4.9: Typical example of measured middle electrode voltage (solid) and discharge current (dotted) during the simultaneous breakdown, using a gas mixture of HCl/Kr/Ne (1.3/60/4940) mbar.

Simultaneous breakdown

As a result of the previous measurement, we obtained $E_{\mathrm{br}} = 10\,\mathrm{kV\,cm^{-1}}$ and $E_{\mathrm{ss}} = 1.3$ kV cm^{-1} for the KrCl gas mixture used at a gas pressure of 5 bar. From the conditions discussed in Sec. 3.2.2, the electrode separations for simultaneous breakdown were determined to be $d_1 = 1.5$ cm and $d_2 = 1$ cm for voltage polarities as shown in Fig. 3.8.

To observe if the simultaneous breakdown could be achieved for this geometry, we measured the middle electrode voltage and the discharge current for the same gas mixture and circuit configuration. Fig. 4.9 shows a typical example of the measured voltage and current waveforms. Since the total gap separation increased by 25%, we charged the PFN capacitance to a voltage of 10 kV. Before breakdown, a middle electrode voltage of 4 kV was measured across the lower discharge volume. In the voltage waveform (solid), we see an increase of the prepulse voltage from 4 kV to -14

kV ($t \approx 230$ ns), followed by a voltage reversal directly into a regime of constant voltage. From the measured voltage waveform follows that both discharges are initiated at a voltage of $U_{\mathrm{mid}} = -14$ kV, causing the voltage to reverse and to reduce to a steady-state field of 2 kV cm^{-1}. This field is somewhat higher than the previously measured one, which we attribute to a slightly higher HCl concentration of the gas fill, which is also suggested to cause the higher breakdown field of 14 kV cm^{-1}. In the measured current waveform, we observe the current to increase to a peak value of 560 A. A small dip is observed in the rising edge of the current signal shortly after the moment of breakdown. The reason is that the current through the discharge is a superposition of the current from the peaking capacitance and the PFN capacitance. As a particular feature of the simultaneous breakdown, the solitary current oscillation observed in the consecutive breakdown during the voltage reversal is avoided.

Summarizing, we realized the simultaneous breakdown in a three-electrode discharge set-up. In the initial stage of the discharge, the current oscillation has been reduced considerably compared to the consecutive breakdown. To investigate in detail the potential of the simultaneous breakdown for sustaining high-pressure KrCl gas discharges, further experiments were carried out with the focus on the discharge homogeneity, which will be presented in the following.

Long-pulse KrCl/XeCl discharges

We investigated particularly the simultaneous breakdown in high-pressure KrCl and XeCl gas mixtures with the goal to create long and homogeneous discharges with pulse durations of several hundreds of nanoseconds. For this, the PFN capacitance was increased from 8 nF to 51.3 nF, using capacitors that are connected in parallel via inductors of equal inductance. This way, we increased the pump pulse duration from 80 ns to 370 ns (FWHM). Every inductor-capacitor pair is called a stage of the PFN. Geometrically, the PFN stages were placed in a row with one outer stage being connected directly to the main electrodes. To calculate the characteristic impedance of a single PFN stage ($Z_c = \sqrt{L/C}$), we estimated the inductance of the PFN connection (L) from its geometric dimensions to be 32 nH. Using these values, we calculate a

characteristic impedance of 3.4 Ω.

In order to reach high prepulse voltages that allow to initiate discharges with a high halogen and heavy rare-gas concentration, we employed a different prepulse scheme compared to the previous section. A three-stage Mini Marx Generator (C_{pp} = 1.2 nF) was used, where three capacitors are charged in parallel and are then connected in series via spark gaps. In this way an output pulse is generated with an amplitude of roughly three times the charging voltage. As a result, peak voltages up to $U_{\mathrm{pp}} = -28$ kV were measured when the Mini Marx Generator was connected to C_{peak} = 200 pF via a coaxial cable. Furthermore, in experiments to characterize the prepulse, we measured a voltage rise time of 30 ns, which is sufficiently short to initiate discharges homogeneously.

Using this configuration, our goal was to generate homogeneous KrCl discharges with pulse durations in excess of 200 ns. To obtain a reference of a homogeneous discharge, we employed the circuit first as pump source for high-pressure XeCl discharges, because these are extensively studied theoretically and experimentally and it is known that XeCl discharges can be pumped for several hundred nanoseconds. As a typical gas mixture for long-pulse XeCl lasers, we employed a gas composition of HCl/Xe/Ne of (0.5/10/4989.5) mbar [53].

To characterize the pumping characteristics of this discharge circuit, we measured the anode-cathode voltage, the middle electrode voltage, and the discharge current. A typical result of this measurement is shown in Fig. 4.10, where (a) the anode-cathode voltage, U_{main}, (b) the middle electrode voltage, U_{mid}, and (c) the discharge current, I_d, have been measured simultaneously. In this graph, the X-ray pulse (not shown) is applied at t = 20 ns. During the first 30 ns shown, the PFN is charged, resulting in an anode-cathode voltage of 4.7 kV and a middle electrode voltage of 1.8 kV. As the prepulse is applied (t = 50 ns), the voltage at the middle electrode reverses and becomes negative, leading to a charge transfer from the prepulse capacitance to the peaking capacitance, as can be seen by the small current peak at this time. As the breakdown voltage is reached (t = 70 ns), the middle electrode voltage reduces and a current oscillation and two peaks in the anode-cathode voltage are observed. As a

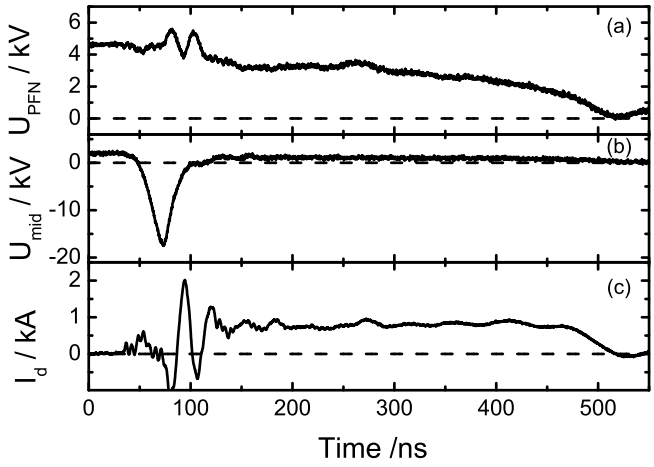

Figure 4.10: Typical example of the measured waveforms of (a) the anode-cathode voltage, (b) middle electrode voltage, and (c) discharge current. Gas composition: HCl/Xe/Ne (0.5/10/4989.5) mbar.

voltage below $2U_{ss}$ was used, the oscillation and both peaks are probably caused by a delayed formation of the discharge. However, this did not influence the discharge stability, as will be shown in the next section. After breakdown, as both discharges are initiated (t = 120 ns), the voltage reduces across the anode and the cathode, therewith also at the middle electrode, to the steady-state voltage. From the measured anode-cathode voltage we determine a steady-state voltage of 3.1 kV. During the steady-state regime of the discharge, a near constant current of 880 A is measured, resulting together with the measured steady-state voltage in a power deposition of 260 kW cm^{-3} and a current density of 220 A cm^{-2}. These values are comparable to long-pulse XeCl lasers and provide for this reason a good reference to observe the discharge homogeneity, as will be shown below. Calculating the electric efficiency of the circuit, $\eta = E_{dep}/E_{in}$, where E_{in} is the sum of the stored prepulse and mainpulse energy and E_{dep} is the energy deposited during the first half-period of the current pulse, we determine a value of 94%, which demonstrates the high efficiency of this excitation circuit.

In order to investigate the electric characteristics of long-pulse KrCl discharges, we filled a gas mixture of HCl/Kr/Ne with partial pressures of (0.5/100/4899.5) mbar into the discharge cell. The circuit parameters were not changed for this experiment. Figures 4.11(a)-(c) show typical examples of the measured anode-cathode voltage, the middle electrode voltage, and the discharge current. Because the electric parameters were not changed compared to the experiment using XeCl, the shape of the waveforms are comparable. However, due to the use of a different gas, we find changes in the measured peak current and voltage. The PFN was charged to a voltage of 7 kV, resulting in the observed constant anode-cathode voltage and middle electrode voltage before breakdown. After preionization (t = 20 ns), the prepulse was applied, increasing the voltage U_{mid} to -18 kV, simultaneously initiating the discharge in both volumes, which lead to the observed reduction of both voltage signals and an increase of the current to its peak value of 2.1 kA in 8 ns. This rise time is extremely short, as typical excimer lasers have rise times in the order of 100 ns, due to a large self-inductance. As the discharge stabilizes ($t \approx$ 200 ns), we measure a steady-state voltage of 3.1 kV for the total anode-cathode separation and a near constant current

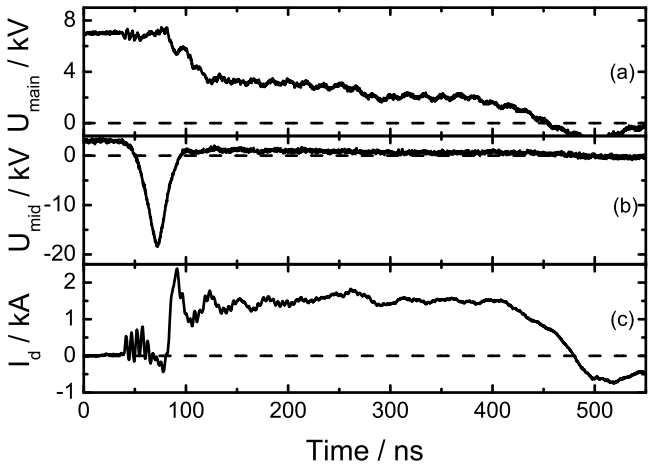

Figure 4.11: Typical example of the measured waveforms of (a) the discharge voltage, (b) middle electrode voltage, and (c) discharge current. Gas composition: HCl/Kr/Ne (0.5/100/4899.5) mbar.

of around 1.6 kA. The current density is approximately 400 A cm^{-2} during this time, resulting in a specific peak power deposition of 540 kW cm^{-3}, which is a value required for the generation of long laser pulses using KrCl [55]. Moreover, we observe a reduction of the discharge voltage at times later than $t = 300$ ns, which can be caused by the depletion of the halogen donor, resulting in a change of the electron balance and, therewith, of the steady-state voltage. However, such a voltage reduction can also be caused due to the formation of filaments, because these reduce the discharge impedance. In the following section, we present experimental results from observations of the discharge homogeneity, with the result that indeed filaments develop on the observed time scale and, thus, can be taken as reason for the voltage reduction.

We calculate an electric efficiency of 88% for the energy transfer from the PFN into the discharge, which still reveals the high efficiency of the discharge excitation circuit. The efficiency is somewhat lower compared to the result obtained for XeCl, because the PFN voltage was charged to a value higher than $2U_{ss}$, which resulted after the first half-period of the current pulse in an extra loss of energy in further current oscillations.

4.3.2 Discharge stability

The output energy and duration of excimer lasers depend strongly on the discharge stability. As will be shown in this section, the development of discharge instabilities in KrCl discharges is unavoidable, however, it is possible to delay them in order to extend the homogeneous phase of the discharge. Consequently in a laser, this allows the extension of the laser pulse duration, the build-up of a beam with a high spatial coherence, and increase of the pulse energy. Employing our test-cell, the observation of the spatial homogeneity of a discharge is a good method to follow the development of the discharge stability [42, 43].

The discharge stability was followed by observation of the fluorescence emission from the discharge with an intensified CCD camera (ICCD), having a gating time of 10 ns. This way, we observed the spectrally integrated light of the discharge. The cylindrical

walls of the discharge cell are transparent in the visible wavelength range. The camera has a CCD array with 512×512 pixels and a spatial resolution of $300\,\mu$m. From the images recorded, the development of the spatial homogeneity of the discharge was observed. The camera was placed such that one discharge volume is recorded at a time. The experiments were carried out as single shot experiments. The synchronization of the CCD camera with the excitation circuit was realized using a pulse delay generator. This way, it was possible to follow the development of the homogeneity in time by shifting the recording time of the camera. This method is valid within certain limits as independent discharges were recorded, but the discharges were found to be very reproducible.

In order to obtain a reference for spatially very homogeneous discharges, we recorded images of XeCl discharges, because these discharges can be homogeneous over several hundred nanoseconds. We employed the gas mixture of HCl/Xe/Ne with partial pressures of (0.5/10/4989.5) mbar. The fluorescence from a single volume was recorded at different times during the discharge, taking steps of 20 ns up to 50 ns between the images. As an example of XeCl discharges pumped with 260 kW cm^{-3}, Figure 4.12 shows images recorded at (a) 100 ns, (b) 200 ns, (c) 300 ns, and (d) 400 ns after breakdown. In these images, the cathode is located at the bottom. As a result, we find the XeCl discharges to be very stable and homogeneous throughout the complete pump pulse duration. Filaments are not observed and the discharge preserves its homogeneous glow until the end of the current pulse.

Analyzing the discharge images further, we find bright spots at the bottom of images (b)-(d), where the cathode is located. The brightness of these spots is a result of a very high local current density, causing thermal emission of electrons from the cathode surface. For this reason, these spots are also called hot spots. Typically, hot spots develop in discharges with current densities of several 100 A cm^{-2}. We find that the hot spots are uniformly distributed on the cathode surface and that the bulk of the discharge remains homogeneous in the presence of hot spots.

To investigate the dependence of the stability of long-pulse KrCl discharges on the gas composition, we employed various partial pressures of HCl and Kr, while keeping

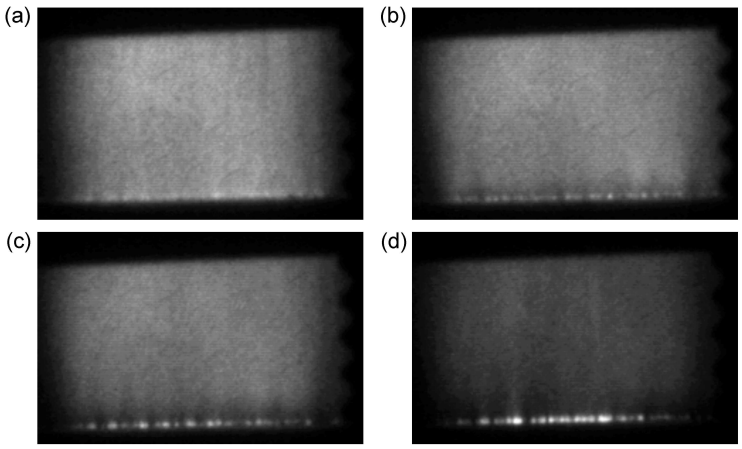

Figure 4.12: Temporal development of a discharge in volume 2 in HCl/Xe/Ne with partial pressures of (0.5/10/4989.5) mbar and a power deposition of 260 kW cm^{-3}.(a) 100 ns, (b) 200 ns, (c) 300 ns, (d) 400 ns after breakdown.

the total pressure at 5 bar. Using a Kr partial pressure of 10 mbar ($p_{\mathrm{HCl}} = 0.5$ mbar), we observed that KrCl discharges are as homogeneous as XeCl discharges. However, while XeCl lasers can be operated with such a low rare-gas partial pressure, KrCl lasers require much higher partial pressures [27,31]. Therefore, the pressure was increased to $p_{\mathrm{Kr}} = 100$ mbar. Also in this high-pressure gas discharge, we observe a very homogeneous discharge up to almost 300 ns in both volumes. As an example, the development of the discharge in a gas mixture with $p_{\mathrm{HCl}} = 0.5$ mbar is shown in Figure 4.13. The images were taken from discharges in the lower volume (a) 100 ns, (b) 200 ns, (c) 300 ns and (d) 400 ns after the breakdown. Again, hot spots become visible on the cathode. The development of hot spots is somewhat faster compared to discharges containing Xe, as they are observed already 50 to 100 ns after the initiation of the discharge. After 200 ns, the width of the discharge decreases in volume 2 by 30% but the discharge remains homogeneous for durations of almost 300 ns. After about 300 ns streamers are clearly observed in volume 2, while in volume

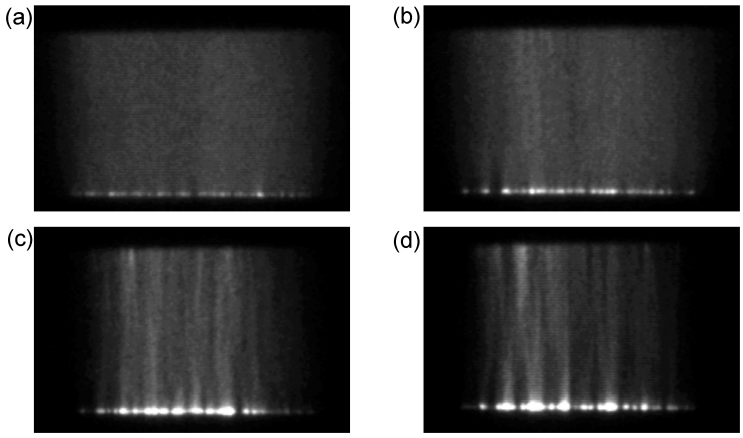

Figure 4.13: Temporal development of a discharge in volume 2 in HCl/Kr/Ne with partial pressures of (0.5/100/4899.5) mbar and a power deposition of 540 kW cm^{-3}.(a) 100 ns, (b) 200 ns, (c) 300 ns, (d) 400 ns after breakdown.

1 filamentation starts somewhat earlier. An increase of the HCl partial pressure to 1 mbar leads to a faster development of filaments and instabilities. This behaviour is shown in Figs. 4.14(a)-(d). The discharge is still very homogeneous 100 ns after the breakdown. Hot spots can already be observed but they are evenly distributed and homogeneous in brightness. Filaments become visible 200 ns after breakdown (Fig. 4.14(b)). The discharge is strongly filamentary at 300 ns (Fig. 4.14(c)) and dark vertical structures are observed. The development of instabilities is accompanied by a reduction of the gap voltage to 50% of the steady-state voltage. Several hotspots become brighter as the current density increases locally. The discharge constricts and becomes asymmetric. At the end of the pump pulse, the discharge width has reduced to approximately 25% of its maximum width and is filamentary.

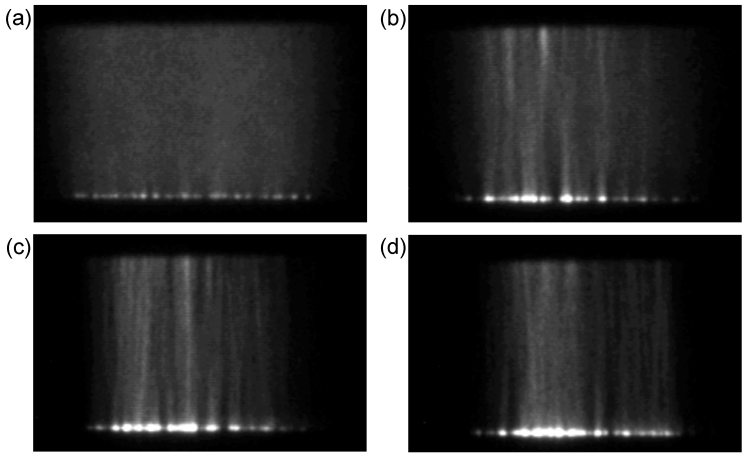

Figure 4.14: Temporal development of a discharge in volume 2 in HCl/Kr/Ne with partial pressures of (1/100/4899) mbar and a power deposition of 540 kW cm^{-3}.(a) 100 ns, (b) 200 ns, (c) 300 ns, (d) 400 ns after breakdown.

Discharge image analysis

For a better understanding of the temporal development of the discharge homogeneity, we defined a figure of discharge instability, based on the homogeneity of the recorded spatial light pattern. For this, we analyzed the images according to the edge detection method [73], determining the gradient of the intensity pattern along the horizontal axis of the discharge bulk (see Appendix A). The figure of instability (ψ_{rms}) defined this way increases as intensity variations in the bulk of the discharge increase.

The definition of a homogeneous discharge is somewhat arbitrary, since an absolute value for the homogeneity is absent. However, correlating the figure of instability with the corresponding images allows one to define a reasonable good dividing line between a homogeneous and inhomogeneous discharge. When keeping the camera position and signal amplification constant between the discharges, this method can be used to compare quantitatively the stability of different discharges, e.g., employing

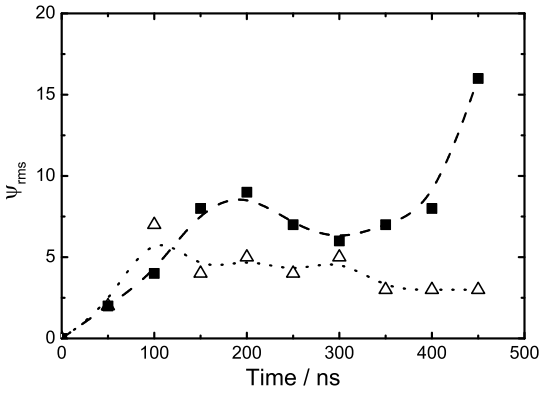

Figure 4.15: Temporal development of the figure of instability, ψ_{rms}, in XeCl discharges, determined for the upper volume (△) and lower volume (■). The lines are drawn to guide the eye.

different partial pressures.

To define the difference between homogeneous and inhomogeneous discharges, we used the recorded images of XeCl discharges in combination with the stability analysis, because of the observed homogeneity throughout the complete pump duration. As a result of the procedure described in Appendix A, Figure 4.15 shows the determined figure of instability for XeCl discharges containing a HCl/Xe/Ne mixture with partial pressures of (0.5/10/4989) mbar and for pump conditions described in Sec. 4.3.1 (see Figs. 4.12(a)-(d)). We observe that in the upper volume the figure of instability increases to a value of $\psi_{\mathrm{rms}} = 9$ during the first 200 ns and decreases to six for $t = 300$ ns. The corresponding images appear to be very homogeneous during this time and we conclude from this comparison that $\psi_{\mathrm{rms}} \leq 9$ represents very homogeneous discharges. Analyzing the determined intensity gradient in detail, we find that the increase and decrease of the figure of instability during the first 300 ns is accompanied by appearing and disappearing small discharge structures at the boundary of the plasma, probably caused by a spatial redistribution of the discharge current during the build-up of the discharge. For times later than 350 ns in the graph, thus at the end of the pump

pulse, the figure of instability is found to increase. Comparing this development with recorded images, we find during this time a decrease of the discharge width by 30%.

Compared to this development, we determine for the lower volume generally lower values of ψ_{rms} during the discharge. Nonetheless, small fluctuations are found, due to the same reason (plasma boundary) as in the upper volume. Moreover, ψ_{rms} reduces for $t > 300$ ns to a value of three. Comparing this development with the recorded images, we see, in contrast to the constriction observed in the upper volume, that the discharge width remains constant and that the light intensity reduces homogeneously with the end of the pump pulse.

With the goal to determine the time-dependence of the KrCl discharge stability on the gas composition, we applied the stability analysis on different HCl/Kr/Ne gas mixtures. As mentioned earlier in this section, the gas mixture contained either HCl/Kr partial pressures of (1/20) mbar, (1/100) mbar, or (0.5/100) mbar, while the Ne pressure (4.9 bar) was kept constant. Fig. 4.16 shows the figure of instability determined from the images recorded from the lower volume as a function of time. We find for a Kr pressure of 20 mbar that ψ_{rms} steadily increases during the first 200 ns with a comparable low rate as found in XeCl discharges. After 250 ns, ψ_{rms} increases to values that are found in XeCl discharges only in the upper volume with the end of the pump pulse and shows the transition into an unstable regime. Increasing the Kr pressure to 100 mbar while keeping the HCl pressure constant, we find that instabilities develop faster. On the other hand, decreasing p_{HCl} to 0.5 mbar leads to a delayed growth of the instabilities. Furthermore, we find that the growth of the figure of instability is well-described by an exponentially increasing function, which can be interpreted the following way. Once minor inhomogeneities are formed in the bulk of the discharge, they are strongly amplified via a positive feedback loop between the high local electron density that characterizes inhomogeneities, and ionization and attachment reactions.

We conclude from this image analysis that the temporal evolution of discharges containing an HCl/Kr composition of (1/20) mbar is comparable to gas mixtures containing (0.5/100) mbar, thus, the discharge stability depends more on the HCl con-

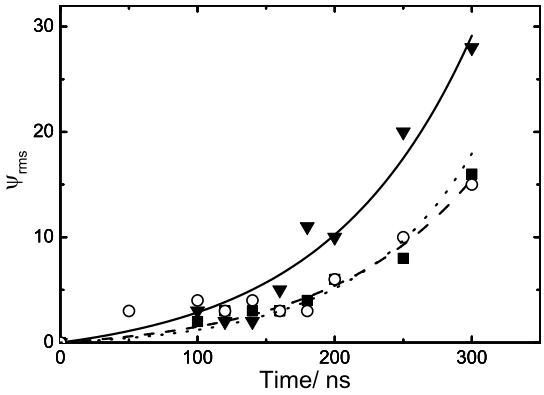

Figure 4.16: Figure of instability, ψ_{rms}, for the lower discharge volume for HCl/Kr pressures of (1/20) mbar (■), (1/100) mbar (▼), and (0.5/100) mbar (○). Exponentially increasing functions are fitted to the data.

centration than on the Kr concentration, which will be explained in the following. Looking at the discharge kinetics shows that the stepwise ionization of metastable Kr increases with higher Kr partial pressure [74]. The electron attachment losses are expected to remain constant when the HCl concentration is kept constant. Therefore, the electron density can increase locally, leading to an increased local consumption of the halogen donor and, therewith, growth of filaments. On the other hand, the steady-state voltage reduces with decreasing HCl pressure, resulting in a lower electron temperature. The attachment rate increases [35] while ionization of metastable reduces. This combination balances the electron density and the homogeneous glow phase of the discharge is extended.

Summarizing, the three-electrode discharge experiments with typical gas mixtures used in long-pulse XeCl lasers revealed very homogeneous discharges for the complete pump duration. In comparison, we find that instabilities develop faster in KrCl discharges. Stable discharges of almost 300 ns were observed for a gas composition containing 0.5 mbar of HCl and 100 mbar of Kr. Increasing the HCl pressure to 1 mbar reduced the stability considerably to a value of 200 ns. As a result of the image

analysis, we find a much stronger dependence of the discharge stability on the halogen donor than on the rare-gas content.

4.4 Summary

A very compact three-electrode system was build to sustain discharges under optimum pump conditions. The discharge current was established very fast (less than 10 ns) due to a very low circuit self-inductance. The short rise time of the prepulse and the discharge current ensure that a high quality discharge can be established and sustained for periods of up to 370 ns (FWHM) with an almost rectangular current pulse.

Using the three-electrode excitation circuit, a high energy transfer efficiency of 88% for KrCl and 94% for XeCl discharges is determined. These values show that the three-electrode circuit can be employed as highly efficient pump source for excimer lasers.

Experiments in mixtures containing Xe as rare-gas revealed that the discharge is homogeneous during the complete pump duration. Although hot spots are observed on the cathode, they do not lead to a filamentation of the bulk of the discharge. In comparison, discharges using Kr at a low partial pressure of 10 mbar were as stable as discharges using Xe. However, an increase of p_{Kr} to 100 mbar lead to an earlier appearance of hot spots and a decreased stability duration. For 1 mbar of HCl the discharge became strongly filamentary already 200 ns after initiation, while for a HCl partial pressure of 0.5 mbar a considerable increase of the stability lead to homogeneous discharges with a duration of 300 ns. These results show that a KrCl laser with a long pulse duration is, in principle, feasible.

Chapter 5

The three-electrode KrCl laser

In this chapter, we demonstrate successfully the first discharge pumped high-pressure KrCl laser with a high discharge quality and long laser pulse duration.

An overview of the discharge system and excitation circuit is given in Sec. 5.1. As is presented in Sec. 5.2, in order to estimate the quality of the developed system, we employed XeCl as active medium and compared the laser output with values that have been presented by others for XeCl lasers. In Sec. 5.3, we present experimental results employing the discharge system successfully as long-pulse KrCl laser. This section is devoted to investigations towards increasing the laser pulse energy and duration and, for this purpose, a parametric study was conducted. As a result of the investigations, we present experimental results in Sec. 5.4, demonstrating the high discharge homogeneity we achieved with the discharge system.

5.1 Three-electrode discharge set-up

In order to give an overview of the designed and constructed discharge system, we describe in the following the three-electrode discharge set-up.

5.1.1 Laser head and preionization source

A schematic cross section of the discharge set-up is given in Fig. 5.1. The discharge system comprises a discharge cell and a preionization source. To separate the discharge electrodes, defining therewith the electrode separation, an electric insulator is placed between the electrodes. The insulator is made of a halogen resistant polymer (PVDF) to avoid corrosion of the wall material and degradation of the gas. All electrodes are made of nickel-coated aluminum, because of the high inertness of nickel with respect to HCl and the good resistivity against surface damage caused by arcs. The middle electrode is a 1 mm thick, solid plate. To test the initiation of discharges in both volumes simultaneously, we chose an electrode separation of 1.7 cm in the upper volume, while the middle electrode was placed in a distance of 2.0 cm from the anode. The discharge cell is operated at a pressure of up to 5 bar. Higher pressures may cause deformation of the electrodes that could lead to electric field distortions, inducing arcs.

Fig. 5.1 shows also a cross section of the X-ray source, which generates X-rays ($\tau_{\text{rise}} =$ 20 ns) by the technique described in Ch. 4.1. Shown in Fig. 5.1 are the corona plasma cathode and the target anode. X-rays are emitted from the target anode toward the gas discharge cell. An X-ray window in the anode confines the preionization beam to a width of 2 cm inside the discharge cell. In order to extract laser energies of up to several hundred mJ, we developed a laser with a volume that is considerable larger than the volume of the test set-up. Using estimations obtained from XeCl lasers [69], we preionized the discharge volume over a length of 80 cm, such that the lower discharge volume amounts to 320 cm^3 and the upper discharge volume to 272 cm^3, giving a total discharge volume of 592 cm^3.

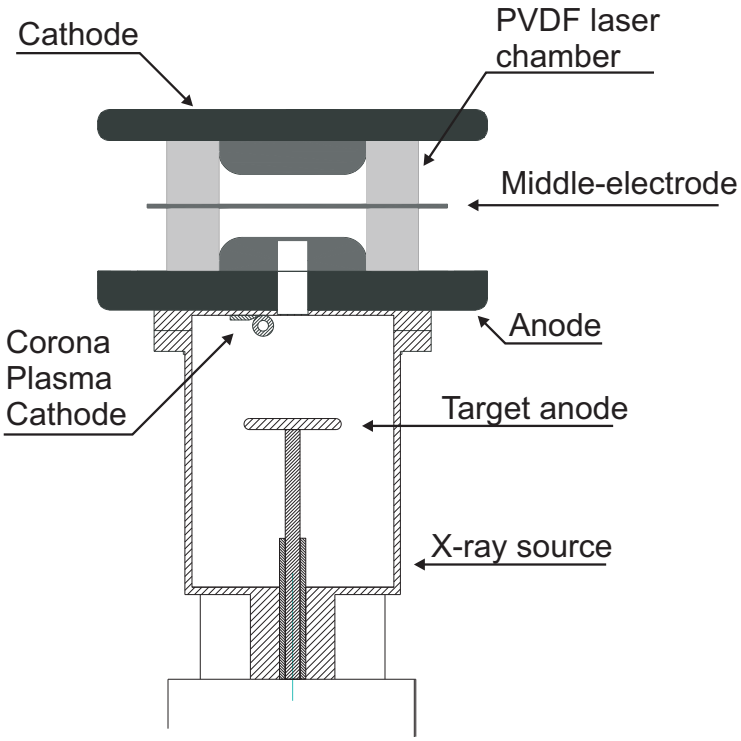

Figure 5.1: Schematic cross section of the three-electrode laser set-up, including the X-ray preionization source.

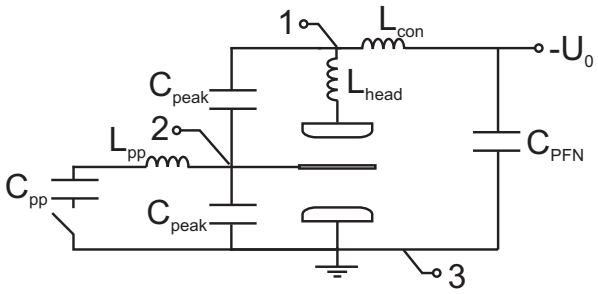

Figure 5.2: Electrical scheme of the electric circuit connected to the three-electrode laser. $C_{\mathrm{PFN}} = 800$ *nF,* $C_{\mathrm{pp}} = 1.8$ *nF,* $C_{\mathrm{peak}} = 3.6$ *nF,* $L_{\mathrm{con}} \approx 30$ *nH,* $L_{\mathrm{pp}} \approx 750$ *nH. 1, 2: high-voltage probe, 3: current probe.*

5.1.2 Excitation circuit

The electrical scheme of the electric circuit built to pump the laser is shown in Fig. 5.2. This excitation circuit is similar to the circuit used for the test-cell presented in Sec. 4.2. The prepulse circuit is connected to the middle electrode of the discharge cell. To obtain a high discharge homogeneity in KrCl, we developed a prepulse circuit that generates a voltage peak with a short rise time of 32 ns, which will be presented in Sec. 5.3.1.

To sustain the discharge after breakdown, a low-impedance pulse forming network (PFN, $Z_{\mathrm{PFN}} \approx 0.2\,\Omega$) is connected to the outer electrodes. The PFN is made of 26 rows of ceramic capacitors with a total capacitance of 800 nF and can be charged to a maximum voltage of 15 kV. Calibrated resistive voltage-divider probes, connected to position 1 and 2 in Fig. 5.2, are used to measure the anode-cathode voltage and the middle electrode voltage. A shunt resistor probe in the current return loop to the PFN is employed to measure the discharge current. The electric power deposited into the discharge is calculated from the discharge current $I(t)$ and the anode-cathode voltage $U(t)$ as $P(t) = U(t) \cdot I(t)$. The voltage is corrected for inductive effects according to Eq. 4.4.

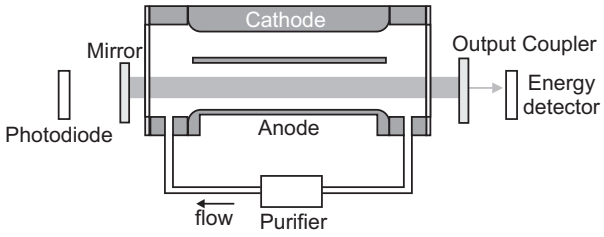

Figure 5.3: Scheme of the three-electrode laser.

5.1.3 Experimental set-up

A scheme of the laser is shown in Fig. 5.3. The gas cell was sealed off from ambient air using anti-reflection coated windows made of fused silica. Additionally, to observe light emitted transversal to the optical axis, view-ports (fused silica) were placed in the sidewall of the laser chamber. The discharge system was equipped with a resonator using dielectric mirrors suited either for XeCl (308 nm) or KrCl laser (222 nm). Depending on the positioning of the laser mirrors either the upper or lower volume, or both volumes simultaneously were used for laser operation. Due to the experimental restrictions set by the open high-voltage, a resonator length of 1.5 m was chosen. A calibrated pyro-electric energy detector was used to measure the pulse energy. The temporal shape of the laser pulse was measured employing a fast photodiode with a rise time of less than 2 ns.

In order to remove gas impurities and to circulate the gas through the discharge volume, a gas purifier with a cryogenic trap is used. By regulating the temperature of the purifier, unwanted impurity species that build-up during discharge operation, like metal-halides, can be frozen out. The purifier can also freeze out any unwanted contaminants brought in with the initial gas filling, e.g., water. These impurities must be removed to avoid degradation of the laser energy by absorption of UV radiation and to prevent the initiation of discharge instabilities.

In order to stabilize the HCl concentration during experiments, the gas system (pu-

rifier and discharge volume) is filled with a higher HCl partial pressure than required and the purifier was employed to control the HCl partial pressure. The excess amount of HCl is frozen out by the cryogenic trap until the desired partial pressure is reached. During discharges, highly reactive halogen components produce molecular species in reaction with the material of the gas system, which reduce the HCl partial pressure and cause the evaporation of HCl from the trap into the gas until the initial partial pressure is restored. This replenishment of HCl by the purifier allows longer operation of the laser with a single gas filling, thereby reducing the chance of contamination of the cell by refilling gas.

5.2 Benchmarking the three-electrode discharge system with XeCl lasers

In order to assess the quality of the developed three-electrode discharge laser, we decided to operate it first as XeCl laser and to compare it with long-pulse XeCl lasers presented in literature. For this, we used a gas mixture containing HCl/Xe/Ne with partial pressures of 0.5/13/4987 mbar, respectively, which is typically used in long-pulse lasers [44,69]. A PFN with a total capacitance of $C_{\mathrm{PFN}} = 280$ nF was connected to the laser head together with a peaking capacitance of $C_{\mathrm{peak}} = 3.6$ nF per discharge volume. To this point no effort was put into an optimization of the PFN, such as a very compact distribution of the capacitance (high packing density). In contrast to the prepulse employed during KrCl discharge experiments, we used for the simplicity of implementation in the electric scheme a Meso Marx Generator ($C_{\mathrm{pp}} = 1.8$ nF) to generate the prepulse, which is a larger version of the Mini Marx Generator (see Sec. 4.3.1). Using this prepulse generator, a rise time of 68 ns was measured, where the rise time is defined as the time difference between 0.1 U_{pp} and 0.9 U_{pp}, where U_{pp} is the peak prepulse voltage, measured while the mainpulse is not applied, as shown in Fig. 5.4.

For simple alignment of the resonator with the prospect of generating high laser pulse

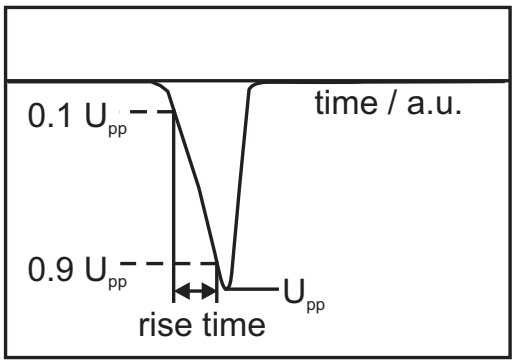

Figure 5.4: Definition of the prepulse voltage rise time.

energies, we equipped the discharge cell with a stable resonator by employing a flat output coupler ($R = 0.7$) and a curved ($r_c = 10$ m), highly-reflecting mirror. The resonator was built for each volume separately to measure the output energy for an optimum resonator alignment. At this point no further effort was put in optimizing the resonator, e.g., via testing various mirror curvatures or reflectivities.

5.2.1 Electrical and laser output characteristics

In the following, we present experimental results of the pulse duration and energy achieved with the three-electrode discharge excitation system operated as XeCl laser.

A typical example of measured electric and optical waveforms is given in Fig. 5.5. Shown are the measured waveforms of the anode-cathode voltage, the middle electrode voltage, the current, and the temporal shape of the laser pulses from both volumes. Before breakdown, the PFN is charged to $U_{\mathrm{PFN}} = -13$ kV. In order to initiate the discharge, the X-ray pulse (not shown) is fired approximately at $t = 50$ ns, followed by the prepulse at $t = 100$ ns, which increases the voltage across the lower volume to approximately -20 kV. As charge flows from the prepulse to the peaking capacitance, it results in the observed negative current pulse at around $t = 130$ ns. When the

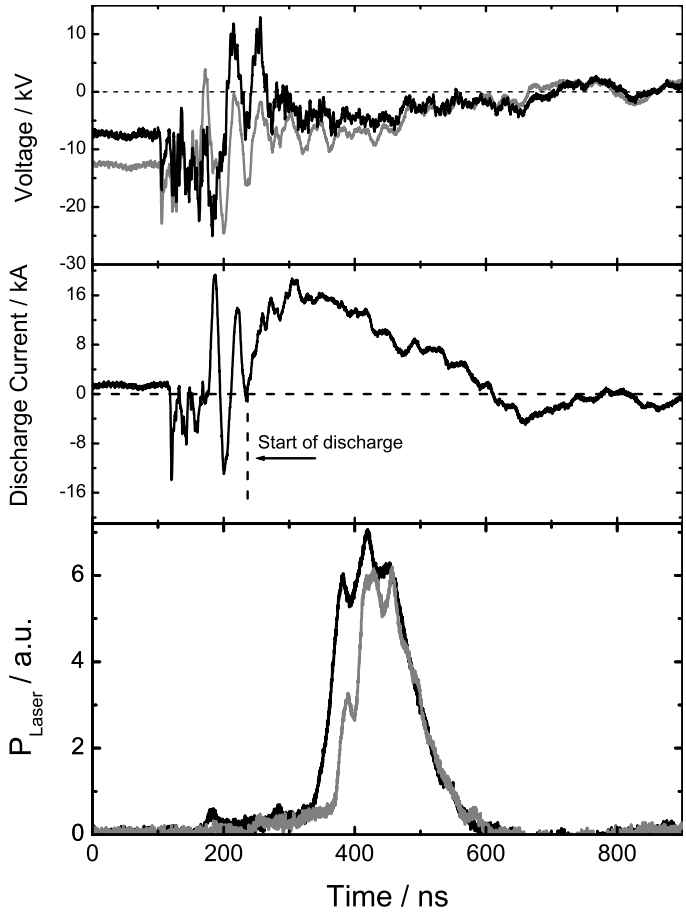

Figure 5.5: From top to bottom: Typical example for measured waveforms in a HCl/Xe/Ne discharge of the main electrode voltage (grey), middle electrode voltage (black), discharge current (black), optical signal of the laser pulses emitted from the upper volume (grey), and lower volume (black). The laser pulses were measured separately.

breakdown threshold is reached in the lower volume, a discharge is initiated there, causing the voltage to reverse. With the forming of a plasma in the lower volume, a current oscillation is observed due to the charge transfer between C_{peak} and C_{PFN}. As a result of the voltage reversal, the discharge starts also in the upper volume and, from approximately $t = 230$ ns, both discharges are sustained by the current from the PFN, reaching a peak current of 18 kA. During the steady-state regime, a voltage of $U_{\mathrm{ss}} \approx -7$ kV is measured. At around $t = 650$ ns, the mainpulse ends and the voltage reduces to zero, inhibiting smaller oscillations due to a slight voltage mismatch. From the pulse shape of the current signal, we determine a pulse duration of 192 ns (FWHM). From the peak current and steady-state voltage, we calculate a specific peak power deposition of 220 kW cm^{-3}, which is comparable to other long-pulse XeCl lasers [59, 69, 75].

The simultaneously measured laser output pulses are shown in the lower graph of Fig. 5.5. Shown in black is the laser pulse emitted from the lower volume, while the laser pulse emitted from the upper volume is shown in grey. It can be seen that the laser pulse generated in the lower volume builds up with a delay of 100 ns with respect to the start of the discharge current, and has a pulse duration of 130 ns (FWHM). In the upper volume, we observe that the laser pulse is detected about 15 ns later ($t = 390$ ns) and we measure a correspondingly shorter pulse duration of 114 ns. The observed time difference between both laser pulses can be explained by the following. As the discharge is initiated first in the lower volume, the peaking circuit sustains the discharge for several nanoseconds and light emission and amplification, although weak, can already take place in the lower discharge volume before the PFN starts to sustain the discharge.

5.2.2 Laser pulse energy

To determine the specific laser pulse energy and laser efficiency for a comparison with other XeCl lasers, we measured the laser pulse energy obtained from the upper and lower volume. As a result, we measured a pulse energy of $E_1 = 270$ mJ from the upper

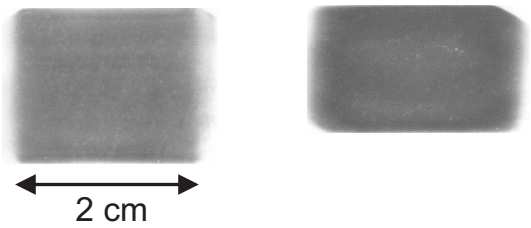

Figure 5.6: Beam imprints of the XeCl laser beam from the lower volume (left side) and the upper volume (right side).

volume and $E_2 = 320$ mJ for the lower volume. The ratio E_1/E_2 is in good agreement with the ratio of the discharge volumes (V_1/V_2) and we determine a specific output energy of 1 J/l for both volumes, which is a high value under the given circumstances (non-optimzed resonator and PFN). A detailed comparison with other XeCl lasers is given in Sec. 5.2.5.

5.2.3 Beam shape

To determine the cross section of the laser beam, beam imprints were taken using thermo-sensitive paper that colors upon absorption of UV-radiation. The paper is placed directly in front of the output coupler. Figure 5.6 shows two typical examples of the beam imprints obtained from the lower volume (left side) and the upper volume (right side). The energies of these pulses are similar to the measured values of E_1 and E_2 mentioned before. As beam cross section, we determine a near-rectangular area of 1.7×2.1 cm^2 for the upper volume and of 2.0×2.1 cm^2 for the lower volume. We find that both cross sections correspond very good to the dimensions of the transversal discharge cross sections, which are imposed by the electrode separations and the width of the discharge as defined by preionization. From this we can conclude that the full preionized volume is employed in the build-up of the laser beam.

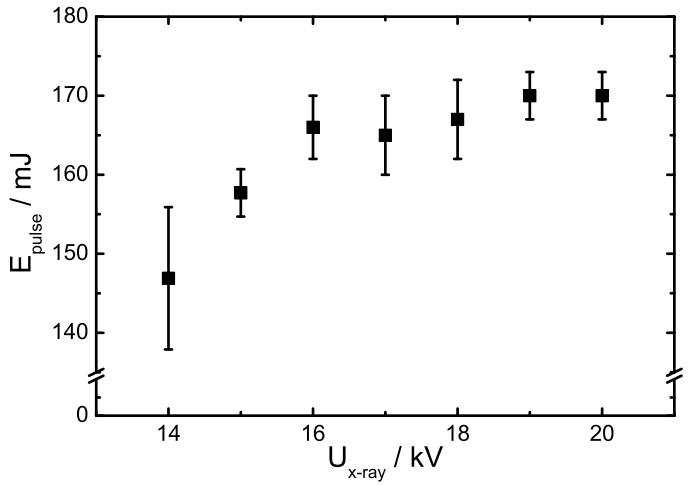

Figure 5.7: XeCl laser pulse energy (upper volume) measured as a function of the X-ray charging voltage $U_{\mathrm{x-ray}}$.

5.2.4 X-ray intensity

In order to infer the X-ray intensity that provides a sufficiently high preionization, we measured the laser pulse energy as a function of the accelerating voltage, which is selected for charging the X-ray source, $U_{\mathrm{x-ray}}$. The pulse energy was averaged over 15 measurements, and its standard deviation was determined from the pulse-to-pulse fluctuation of the laser output energy. Figure 5.7 shows the average pulse energy of the upper volume for increasing charging voltages and its standard deviation. We observe an increase of the pulse energy from 148 mJ to 165 mJ as the voltage is increased from 14kV to 16 kV. A further increase of the voltage results in a saturation of the pulse energy at approximately 170 mJ. We find that the measured pulse energies were generally lower compared to the previous measurement, which we address to changes in the gas composition during the experiments. The rise in output energy with voltage is attributed to a higher preionization electron density, which is then increased by several orders of magnitude due to the application of the prepulse, leading

to improvements of the discharge quality. However, for voltages above 19 kV, the preionization electron density is high enough so that a further increase does not contribute significantly to an improvement of the discharge quality and, consequently, the energy saturates.

5.2.5 Evaluation of the performance

In conclusion, operating the developed three-electrode XeCl laser, we successfully demonstrated high output energies of 1 J/l and pulse durations in excess of 100 ns, although, as was noted before, neither the resonator nor the PFN were optimized. Nevertheless, the specific energy is only somewhat (20%) lower than was reported for other long-pulse lasers after optimization [56, 59, 60]. Also, we expect an increase of the pulse energy by further extending the duration of the pump pulse or by adding HCl.

When determining the electric efficiency of the prepulse-mainpulse circuit, we find a value of 3%. Even though not optimized, this value is better than the efficiency of 2.8% measured by Borovkov et al. [58] and only slightly below the efficiency of 3.2% measured by Bollanti et al. [59] for a similar XeCl laser. This comparison shows successfully that the developed discharge set-up is highly suitable to excimer lasers and marks a step towards the development of a long-pulse KrCl laser.

5.3 Investigations on the operation as KrCl laser

Turning to KrCl as gain medium, to achieve a high discharge quality and laser pulse durations in excess of 100 ns, we performed a parametric study on the electric circuit and the gas composition as follows.

First, we present the discharge excitation scheme with the modified prepulse in Sec. 5.3.1. This is followed in Sec. 5.3.2 by the determination of the self-inductance of the mainpulse circuit, which is an important parameter in order to achieve a high

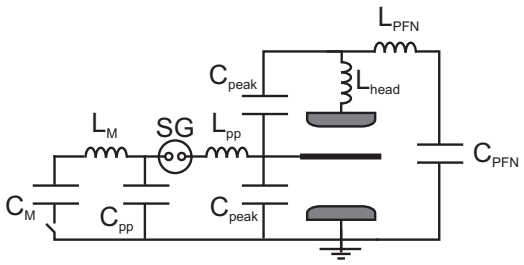

Figure 5.8: Electrical scheme of the excitation circuit used for KrCl as gain medium. C_{PFN} = 800 nF, C_M: storage capacitance (1.8 nF), L_M: charge-line inductance (2 μH), C_{pp}: prepulse capacitance (3.6 nF), C_{peak}: peaking capacitance (2 $C_{\mathrm{peak}} = 6.7$ nF).

power deposition. Next to the self-inductance, for an optimum energy transfer from the PFN into the discharge, we determine the steady-state voltage for three KrCl gas mixtures. Section 5.3.3 describes the experimental set-up and presents first measurements of the successful generation of long laser pulses employing KrCl. In order to maximize the pulse duration and energy, we conducted a parametric study that included the discharge excitation circuit as well as the gas composition. The results of this study is presented in Sec. 5.3.4 and Sec. 5.3.5.

5.3.1 KrCl excitation circuit

Although the measurements employing XeCl as gain medium demonstrated the good performance of the excitation circuit, we developed an alternative prepulse to initiate KrCl discharges. The goal was to develop a prepulse with a rise time of about 30 ns, as the discharge experiments with the test-cell resulted in long stable discharges employing such a short rise time (see Sec. 4.3.1). Figure 5.8 shows the alternative electrical scheme of the excitation circuit. The developed prepulse circuit consists of a single capacitance, C_{pp} = 3.6 nF, mounted on a N_2 pressurized spark gap (SG). The prepulse capacitor and the spark gap are mounted in a distance of only 20 cm

from the middle electrode, resulting in a very small current loop for C_{pp} and C_{peak}, thus, reducing the parasitic inductance L_{pp}. Since voltages of several tens of kV are applied to the prepulse capacitance, a closer positioning was not possible without risking an electric flash-over to other circuit components. The prepulse capacitance, C_{pp}, is charged by a storage capacitor (C_{M}) via a CLC-circuit. The pressure in the spark gap is chosen such that the gap is triggered spontaneously when C_{pp} is fully charged. If the pressure and voltage are chosen carefully, a low time jitter of below 25 ns was achieved resulting in very reproducible discharge conditions. Most important is that we realized the desired short rise time of only 32 ns, which makes this circuit highly suitable for the fast discharge initiation.

The connection of the PFN capacitance, $C_{\mathrm{PFN}} = 800$ nF, to the laser has an intrinsic (parasitic) inductance, L_{PFN}, which adds to the total circuit self-inductance. The PFN inductance was minimized by mounting the capacitors in the most compact way, i.e., were they occupy the smallest possible volume (highest packing density). The total mainpulse self-inductance is given by $L = L_{\mathrm{head}} + L_{\mathrm{PFN}}$, where L_{head} is the laser head self-inductance, arising due to its geometric dimensions. In the following, experimental results will be presented in order to quantify the circuit self-inductance.

5.3.2 Determination of the laser head inductance and KrCl steady-state voltage

A low self-inductance is essential for achieving high pump power densities, because the discharge current increases only with the inverse square-root of the self-inductance. In this section, we show that the three-electrode circuit was successfully developed to yield a very low total self-inductance of approximately 30 nH, which includes the discharge driving circuit and the laser head. In order to fulfill the voltage-matching condition, the measurements used to determine the self-inductance were also used to determinate the steady-state voltage.

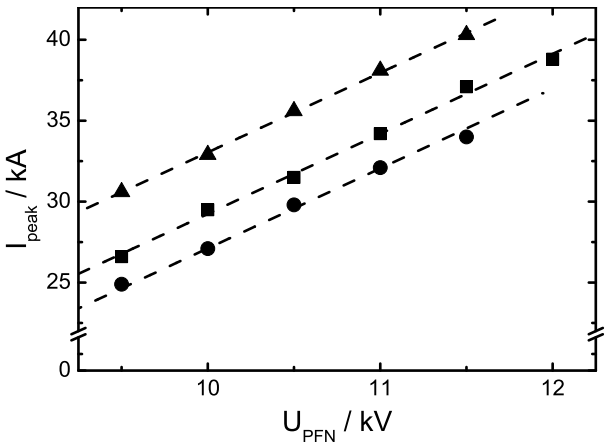

Figure 5.9: Peak current, I_{peak}, as function of the PFN charging voltage, U_{PFN}, for different HCl partial pressures: $p_{\mathrm{HCl}} = 0.4$ mbar (▲), $p_{\mathrm{HCl}} = 1.0$ mbar (■), $p_{\mathrm{HCl}} = 1.5$ mbar (●). $p_{\mathrm{Kr}} = 100$ mbar, $p_{\mathrm{Ne}} \approx 3.4$ bar.

Laser head inductance

To estimate the circuit self-inductance, we measured the peak discharge current, I_{peak}, as a function of the PFN charging voltage, U_{PFN}, as shown in Fig. 5.9 measured for HCl partial pressures of 0.4 mbar, 1 mbar, and 1.5 mbar. A Kr partial pressure of 100 mbar and a Ne partial pressure of 3.4 bar were filled into the gas system. We find that the peak current increases in all three cases linearly with the charging voltage, however, the value of the peak current increases with decreasing HCl partial pressure, which is the result of a reduction of the discharge steady-state voltage as will be shown in the following section.

Using Eq. 3.2, the peak current is given by:

$$I_{\mathrm{peak}}(U_{\mathrm{PFN}}) = \sqrt{\frac{C}{L}}(U_{\mathrm{PFN}} - U_{\mathrm{ss}}). \tag{5.1}$$

As the circuit parameters, C and L, are kept constant, a reduction of the HCl concen-

tration leads to a reduction of the steady-state voltage, which increases the voltage difference in Eq. 5.1 and, thus, the peak current. Moreover, we see from Eq. 5.1 that the slope in Fig. 5.9 is given by the inverse of the impedance $Z = \sqrt{L/C}$, while from the y-axis offset, $I_{\mathrm{peak}}(0)$, the steady-state voltage can be determined. Using a linear fit to the data sets gives an impedance of 0.2 Ω, from which we obtain an inductance of $L = 33$ nH. In the following, we want to estimate the self-inductance of the laser head, L_{head}, in order to show that a further reduction of L is possible when $L_{\mathrm{PFN}}$is reduced, which could lead to a further increase of the pump power density. The estimation can be made using the geometric dimensions of the laser vessel:

$$L_{\mathrm{head}} = \frac{\mu_0 \mu_r A}{l}, \tag{5.2}$$

where A is the area enclosed by the current loop and l is the length of the magnetic field lines, approximately twice the discharge length. Using for the geometry of the discharge cell the following estimated values: $A = 250$ cm^2, $l = 1.6$ m, and $\mu_r = 1$, yields a laser head inductance of 10 nH. As a conclusion, a further reduction of the total mainpulse self-inductance seems possible by reducing the size of the PFN current loop, which should allow to sustain discharges with a higher power deposition.

Steady-state voltage

Using the experimental results presented in Fig. 5.9, we determine the steady-state voltage. This value is required for optimizing the energy transfer from the PFN into the discharge (voltage-matching condition). From the y-axis intersection for $U_{\mathrm{PFN}} = 0$ V in Fig. 5.9 and Eq. 5.1, the steady-state voltage is determined. The calculated steady-state voltage is shown in Fig. 5.10, given as a function of the HCl partial pressure. The partial pressures of Kr and Ne were kept constant. It can be seen that the steady-state voltage increases when adding HCl, which is expected due to an increase of the electron attachment as follows. In the electron balance (see Eq. 2.26), an increased HCl concentration leads to the effect that the steady-state field increases, which is required to balance via ionization the electron loss.

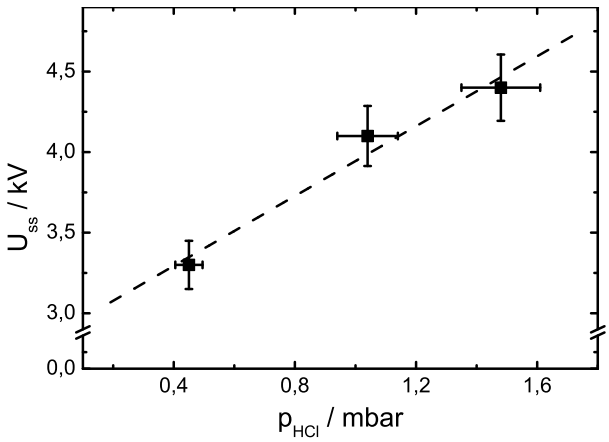

Figure 5.10: Measured steady-state voltage, U_{ss}, as function of the HCl partial pressure, p_{HCl}, for $p_{\mathrm{Kr}} = 100$ mbar and $p_{\mathrm{Ne}} = 3.399$ bar.

5.3.3 Experimental set-up

To extend the parametric studies also to laser operation, the KrCl laser was equipped with a stable resonator configuration according to Fig. 5.3. The windows were anti-reflection coated for $\lambda = 222$ nm. Also, the mirrors were exchanged for a highly-reflecting ($R \approx 1$) curved mirror ($r_c = 5$ m) and a output coupler with 10% transmission. A bandpass filter ($\lambda_c = (214 \pm 12)$ nm) was used in combination with a photodiode to detect the temporal shape of the laser pulse. The laser pulse energy was measured using a calibrated pyro-electric energy detector.

Typical KrCl laser pulse generation

The successful generation of KrCl laser pulses with long duration became apparent via observing waveforms of extended length for the laser pulse as well as for the discharge current. The laser was operated with HCl/Kr/Ne partial pressures of (1/100/3899) mbar. Figure 5.11 shows a typical example of the measured waveforms of the discharge

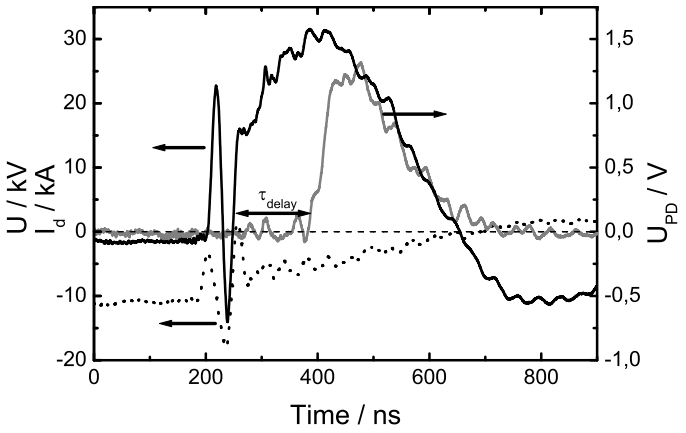

Figure 5.11: Typical measured KrCl discharge waveforms. The main electrode voltage (dashed), discharge current (black), and laser pulse (grey) are measured as function of time. $U_{\mathrm{PFN}} = -11$ kV and HCl/Kr/Ne partial pressures of (1/100/3899) mbar.

voltage, current, and laser pulse, which will be described in the following. The PFN is slowly charged to a voltage of -11 kV, which is also applied to the main electrodes of the discharge system. When the PFN is fully charged, the prepulse (voltage of -36 kV) is applied to the middle electrode at $t \approx 200$ ns. The prepulse initiates a discharge in both volumes, causing the observed current oscillation between $t = 200$ ns and $t = 250$ ns. Subsequently, the discharge is sustained by the PFN and a peak current of 32 kA is measured ($t = 400$ ns). For the current pulse, we determine a duration of 404 ns (full width at base), which is given by the LC-time of the discharge driving circuit (see Chapter 3). Compared to the start of the discharge current ($t = 250$ ns), the signal from the laser pulse is observed to appear approximately 135 ns later. Compared to the measurement with XeCl, this build-up time is higher by almost 50% and we expect this to be caused by a lower gain when compared to XeCl (see also Chapter 6). Nonetheless, we successfully obtained a laser pulse duration of 145 ns (FWHM), which compares favorably with previously reported attempts to realize long-pulse KrCl lasers, ranging from 60 ns to 135 ns [31, 55, 58]. The measured pulse

energy of 78 mJ was found to be below energies reported for other lasers (e.g., Ref. 55). However, as will be shown below, a considerable improvement of the pulse energy is achieved by optimizing the resonator and the gas composition.

5.3.4 Parametric study on the performance of the long-pulse KrCl laser

Starting from the measurements presented in the previous section, we investigated the dependence of the energy and pulse duration of the laser output on the preionization, the charging voltages of the excitation circuit and the gas composition. The results obtained from this parametric study are described and discussed in the following sections.

Preionization

As pointed out in the measurements on the XeCl laser, the preionization density is important for the discharge stability and, consequently, also for the laser pulse energy and duration. Above, we described the saturation of the XeCl pulse energy for X-ray charging voltages above 19 kV. However, as has been pointed out by Panchenko et al. [31], the pulse energy in KrCl laser can be expected to be even more sensitive to the preionization intensity. For this reason, we conducted experiments on the KrCl laser pulse energy as a function of the X-ray intensity with the goal, to determine the voltage, for which saturation of the pulse energy can be observed.

The lower discharge volume was equipped with the resonator described in Sec. 5.3.3 to measure the pulse energy as a function of the X-ray charging voltage. Shown in Fig. 5.12 is the result for a HCl/Kr/Ne gas mixture of (1/80/3220) mbar. The energy is found to increase strongest in the voltage range between 10 kV and 13 kV. For higher voltages, the energy increases less and saturates finally for voltages above 18 kV to a value of 45 mJ. The saturation takes place due to a rising preionization electron density at a voltage, where a further increase does not further contribute to

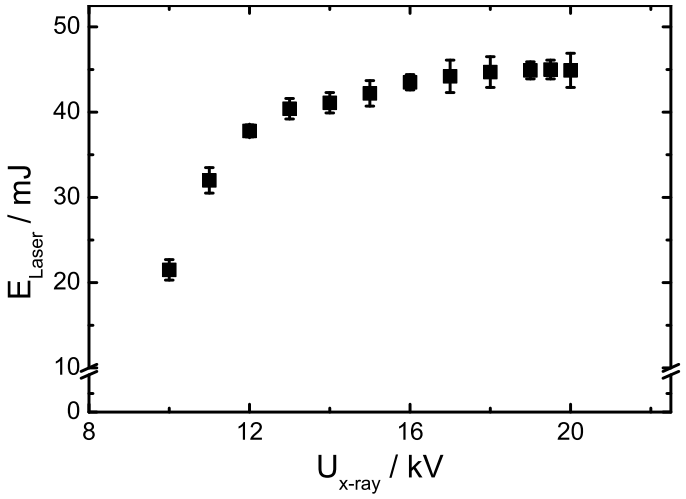

Figure 5.12: KrCl pulse energy (single volume) measured for varying X-ray charging voltage, $U_{\mathrm{x-ray}}$.

the discharge quality, as described in the experiments with XeCl.

Dependence on preionization timing

The preionization electron density, generated in the discharge volume due to the X-ray pulse, is increased to the required high electron densities of $\approx 10^{15}$ cm^{-3} by applying the prepulse voltage. However, if the delay between the X-ray pulse and the prepulse is too large, the preionization density will be reduced due to electron attachment to halogen or recombination with ions, leading to a reduction of the laser energy. Moreover, an electron depleted layer is formed close to the cathode as electrons drift away in the electric field of the anode-cathode voltage, giving rise to the formation of filaments, as observed by Timmermans [69].

To investigate the dependence of the laser performance on the preionization timing, we varied the time delay between X-ray pulse and prepulse. The time delay is defined

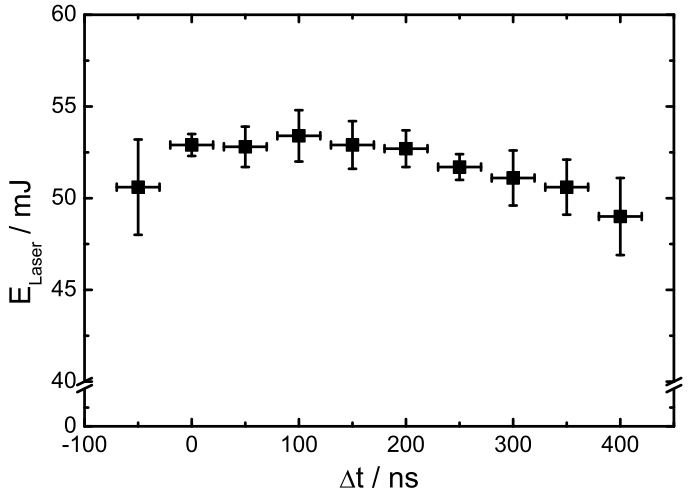

Figure 5.13: KrCl pulse energy (single volume) measured versus delay times, Δt.

in this measurement as the time difference between the peak prepulse voltage and the peak X-ray intensity, $\Delta t = t_{\mathrm{pp}} - t_{\mathrm{x}}$. The PFN was charged to a voltage of 11.5 kV. Shown in Fig. 5.13 is the measured pulse energy of the lower volume as a function of the delay between the X-ray pulse and prepulse. Measuring the pulse energy 15 times per delay, we calculated the mean energy and the standard deviation, which is shown as error bar. As a result, we find the lowest laser pulse energy and highest pulse-to-pulse energy fluctuation when the prepulse is fired well before the X-ray pulse ($\Delta t = -50$ ns). Such a result is expected, because the electron density is not sufficiently high when the prepulse is applied before the preionization and, thus, the required electron density to form a homogeneous discharge is not reached. On the other hand, firing the prepulse up to 100 ns after the X-ray pulse is found to affect the laser energy only marginally. However, a larger time delay reduces the laser energy and increases the pulse-to-pulse fluctuations. We conclude from these measurements that the optimum time delay is around 100 ns and that the time jitter of the prepulse circuit (25 ns) is not of importance for the discharge stability.

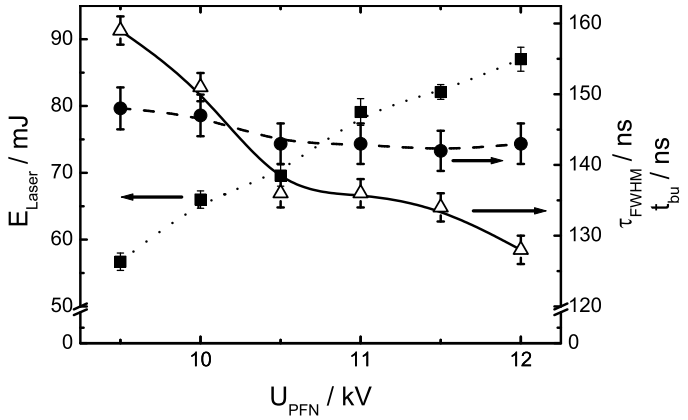

Figure 5.14: Laser pulse energy (■), build-up time (△) and pulse duration (●) measured as a function of U_{PFN}. HCl/Kr/Ne partial pressure: (1/100/3399) mbar.

Dependence on PFN voltage

As has been shown in Sec. 5.3.4, the peak current and, thus, power density depends on the charging voltage of the PFN and an increase of the PFN voltage might increase the laser pulse energy. For this purpose, we measured the laser pulse energy as a function of the PFN charging voltage. Additionally, as the higher peak power is expected to change the reaction rates of excimer formation, we measured the laser pulse duration and the build-up time of the laser pulse. We defined the latter as the time-difference between the rising edge of the laser signal and current, taken at $0.1\,\hat{U}_{\mathrm{PD}}$ and $0.1\,I_{\mathrm{peak}}$, where $\hat{U}_{\mathrm{PD}}$ is the peak laser signal and I_{peak} is the peak current (see Fig. 5.11). For this experiment, we used a gas mixture containing HCl/Kr/Ne at partial pressures of (1/100/3399) mbar.

Shown in Fig. 5.14 is the laser pulse energy (lower volume), pulse duration (FWHM), and build-up time measured as a function of the PFN charging voltage. Measuring the pulse energy, we find that, by increasing U_{PFN} from 9.5 kV to 12 kV, the laser energy increases almost linearly from 56 mJ to 87 mJ. Higher voltages than 12 kV were not

applied in this experiment, as the increasing voltage-mismatch with the steady-state voltage lead to reverse currents that caused arcing inside the discharge volume.

Additionally, Fig. 5.14 shows that the pulse duration reduces only slightly from 148 ns to 143 ns over the applied voltage range. On the other hand, the build-up time reduces from 160 ns to 128 ns as the PFN charging voltage is increased to 12 kV. Thus, although the laser pulse is observed to start almost 40 ns earlier, the laser pulse duration remains almost constant. In the following, we will explain this result. As the voltage is increased, the discharge current increases with the result that also the power deposition increases. As will be shown in Chapter 6, this leads to an increase of the gain and consequently, to a faster build-up of the laser power. However, HCl is consumed during the discharge since a recombination channel of hydrogen and chlorine ions back to HCl does not exist on the time scale of the discharge. A higher power deposition results in a faster consumption with the result that the number of excited KrCl reduces earlier. Consequently, the laser pulse duration does not gain from the faster build-up. As will be shown in the following, the addition of HCl to compensate for its consumption is restricted due to the reduction of the stability of the laser.

5.3.5 Gas composition

To determine the optimum gas pressure, which provides the highest output energies and longest pulse duration, both laser parameters are measured for different halogen, buffer gas, and rare-gas pressures for the lower discharge volume.

First, to determine the dependence of the output energy on the halogen content, we increased the HCl partial pressure in steps from 0.4 mbar to 2.1 mbar and measured the laser energy. This measurement was repeated for several total gas pressures, ranging from 2.5 bar to 5.0 bar. Shown in Fig. 5.15 is the measured pulse energy, each point averaged over 15 pulses. The standard deviation is depicted as error bar. We observe that, except for the data obtained with 2.5 bar, an increase of the HCl partial pressure from 0.4 mbar to approximately 1.1 mbar leads to an increase of the

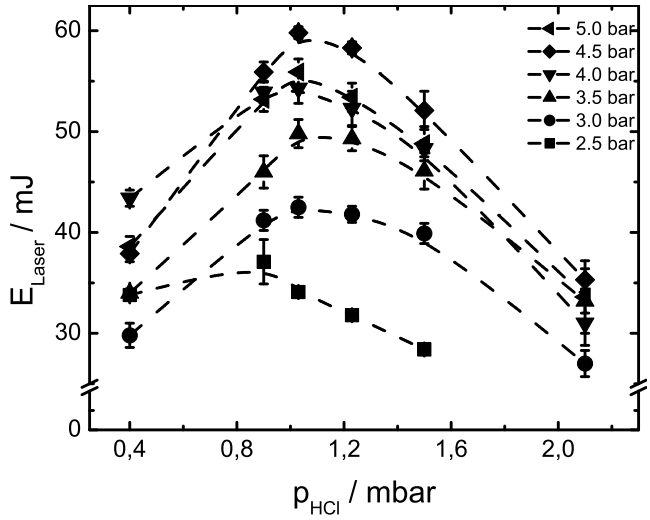

Figure 5.15: Pulse energy as function of the HCl partial pressure, p_{HCl}. The total pressure is varied while $p_{\mathrm{Kr}} = 80$ mbar.

pulse energy. For higher HCl partial pressures, we find that the laser pulse energy reduces. The observed dependence of the laser pulse energy on an increasing halogen concentration is explained in the following by the trade-off between the formation of excimers and, therewith, the gain, and the growth of discharge instabilities (see Sec. 4.3.2). In the range of 0.4 mbar to 1.1 mbar, the addition of HCl leads to an stronger increase of the formation of excited $KrCl^*$ molecules than is lost due to the growth of instabilities. However, for partial pressures above 1.1 mbar, the power deposition becomes increasingly inefficient as instabilities, e.g., filaments, dominate the discharge. As a result, the formation of $KrCl^*$ and, therefore the energy, reduces.

In a second step, keeping $p_{\mathrm{HCl}} = 1$ mbar constant, the laser pulse energy and duration were measured as a function of the Ne partial pressure. In this experiment, the reduced field, E/p, was found to be ≈ 0.37 kV cm^{-1} bar^{-1}. To account for the increasing steady-state voltage with increasing total pressure, the PFN charging voltage was increased. Also, the prepulse voltage was increased to account for the higher breakdown voltage when increasing the total pressure. Shown in Figs. 5.16(a) and (b) are the measured laser pulse energy and duration with varying Ne pressures. Additional measurements were carried out with gas mixtures containing either $p_{\mathrm{Kr}} = 90$ mbar or $p_{\mathrm{Kr}} = 130$ mbar. We find a peak pulse energy of 85 mJ for a Kr partial pressure of 90 mbar and $p_{\mathrm{Ne}} = 4.3$ bar. Increasing p_{Kr} to 130 mbar resulted in a shift of the optimum Ne pressure to a lower value of around 3.8 bar. With a krypton partial pressure below 60 mbar, no laser action is observed.

For a Kr partial pressure of 90 mbar, the maximum pulse duration of 152 ns is obtained at a Ne pressure of 3.3 bar and decreases to 145 ns beyond this pressure. It can be seen that the pulse duration changes only by 5% in the investigated pressure range, while the energy changes by about 80% and, therefore, mainly the peak power increases with the pressure. For a Kr partial pressure of 130 mbar, we find the peak pulse duration of 148 ns for a Ne pressure of 3.3 bar.

In the following, an interpretation of the obtained results based on a qualitative discussion of the basic chemical reactions in the discharge is given. The optimum working pressure of the laser, as determined by the pulse duration and output energy,

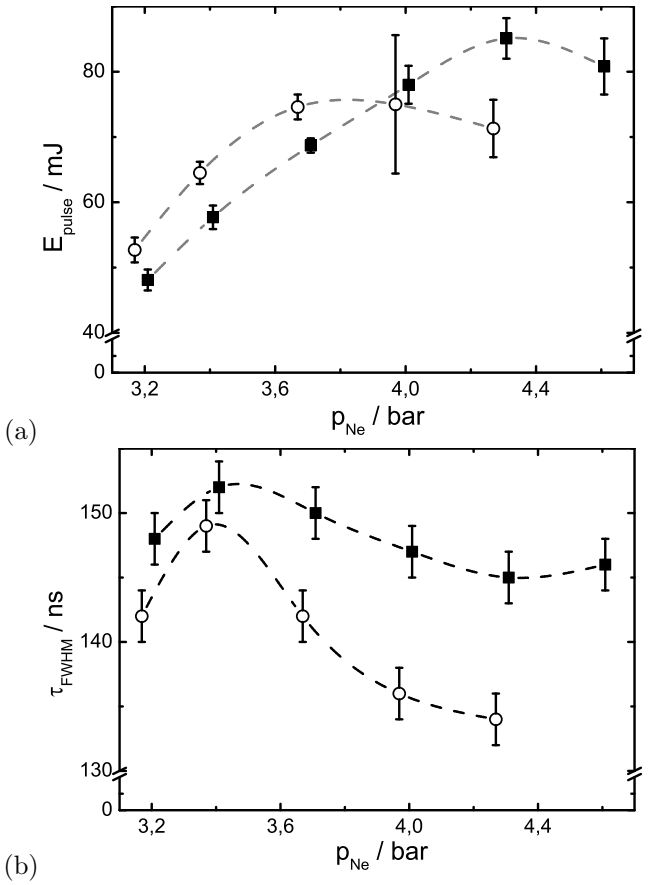

Figure 5.16: (a) Laser pulse energy, E_{pulse}, and (b) pulse duration, τ_{FWHM}, as function of the Ne pressure, p_{Ne}, and for two different Kr partial pressures. ■ *: $p_{\mathrm{Kr}} = 90$ mbar,* ○ *: $p_{\mathrm{Kr}} = 130$ mbar. Output coupler reflectivity $R_{OC} = 0.9$ and radius of curvature of the reflector ($R > 0.999$) $r_c = 5$ m.*

is given by the balance of the production and loss of KrCl molecules. The initial enhanced pulse energy employing a higher Kr partial pressure is assumed to be the result of a faster formation of KrCl, as the initial Kr^+ density is higher:

$$Kr^* + e^- \rightarrow Kr^+ + 2e^-. \tag{5.3}$$

Therefore, a higher electron density due to the additional ionization of excited Kr atoms is expected. The consumption of HCl and vibrationally excited HCl(v) increases with the higher electron density as a consequence of the high electron attachment rate [35] for the low E/p values used to generate long optical pulses. Furthermore, we expect that the formation of $KrCl^*$ via the harpooning channel

$$Kr^* + HCl \rightarrow KrCl^* + H \tag{5.4}$$

is only of minor importance, as will be shown in the following discussion. For the Kr($^3P_2$) state, this reaction is energetically forbidden and, therefore, must involve the higher lying levels ($^3P_1$, $^3P_0$) of Kr. However, to access these states, a sufficiently high electron temperature is required that scales in proportion with the value of E/n, where E is the applied electric field and n is the gas number density. Even in a high-power, short-pulse KrCl lasers, this reaction channel has been found to only contribute 6 % to the KrCl density [27]. In our experiments, when compared to short-pulse lasers [48], the value of E/n is typically one order of magnitude lower and is in the order of 1×10^{-17} V cm^2. Thus, although no precise number can be given here, in long-pulse KrCl discharges the harpooning channel should only contribute marginally to the excimer formation. It looks therefore advantageous, to increase the HCl partial pressure to compensate the consumption. Indeed, we observed that adding HCl to the gas mixture increases the pulse power but also to reduce the pulse duration with the result that the pulse energy reduces. The $KrCl^*$-density is expected to increase as more Cl^--ions are present in the discharge. Nonetheless, increasing the Ne pressure above the optimum pressure reduces the upper laser state population due

to enhanced quenching processes of $KrCl^*$ involving the rare-gas and buffer gas, e.g.:

$$\begin{aligned} KrCl^* + Kr + Ne &\rightarrow Kr_2Cl^* + Ne, \\ KrCl^* + Ne &\rightarrow Kr + Cl + Ne. \end{aligned} \tag{5.5}$$

From this we conclude that the laser performance is determined by the halogen consumption and collisional quenching processes taking place in the gas discharge.

From the measured low pulse-to-pulse energy fluctuation of less than 5%, as expressed by the error bars in Fig. 5.16(a) we obtained a first impression of the high discharge quality achieved in KrCl with the developed excitation circuit. An exception are the large deviations oberved for $p_{Ne} = 4$ bar and $p_{Ne} = 4.3$ bar in combination with $p_{Kr} = 130$ mbar. Here, the discharges were instable from the beginning. We found the reason in the required high prepulse voltage to initiate the discharge for such a pressure. The breakdown voltage increased such that flash-overs to other circuit elements occured. This resulted in power loss of the prepulse, consequently leading to an insufficient discharge initiation. Because the breakdown voltage depends, next to the other gas constituent, on the amount of rare-gas [30], this effect was observed to be weaker when employing $p_{Kr} = 90$ mbar.

5.4 Discharge homogeneity

In order to determine the homogeneity of the discharge, we measured the propagation of the laser beam when generated in a plane-plane resonator. The beam generated in such a resonator reflects very strongly the spatial homogeneity of the gain medium as will be explained in the following. In a plane-plane resonator, photons emitted parallel to the optical axis are reflected back into the gain medium and experience for this reason a higher amplification after several roundtrips than photons emitted in a nonparallel direction. This causes photons mostly to traverse the discharge region within a small sub-volume of the gain medium parallel to the optical axis. As an example, discharge inhomogeneities, e.g., streamers, have been observed in the near-

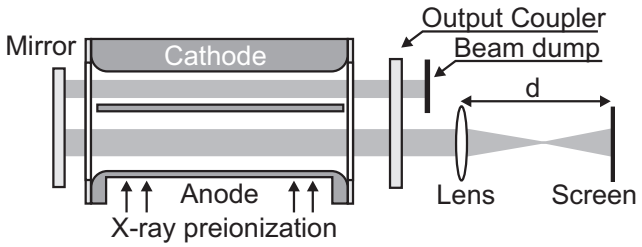

Figure 5.17: Plane-plane resonator of the three-electrode KrCl discharge laser used to measure the beam propagation.

field intensity distribution of long-pulse XeCl laser beams by recording the near-field with burn patterns [75]. Furthermore, after focusing the output beam with a lens, the beam divergence can be used as a relative measure of the discharge quality when compared to lasers of similar resonator length and discharge cross section, whose discharge quality and beam divergence are known. Under these circumstances, laser beams generated in a discharge with a poor spatial homogeneity have a very large beam divergence compared to laser beams generated in discharges with a high spatial homogeneity.

Employing the plane-plane resonator shown in Fig. 5.17, the focusability of both laser beams was investigated. The measurement was performed for each beam separately by blocking one of the beams at a time (behind the outcoupler). A lens with a focal length of 1 m was used to focus the remaining beam on thermo-sensitive paper and the spot size was determined from the coloring of the paper. With this method, we found that the spot size in the focus can be determined with an accuracy of $\pm 15\%$, due to the high energy density in the focus that leads to sharp rising edges in the beam imprint, defining well the spot size. To determine the minimum spot size, the measurement was repeated at various positions along the optical axis close to and in the focal plane of the lens. The measured spot size, w, plotted as function of the distance, d, to the lens is shown in Fig. 5.18(a) for the upper volume and in Fig. 5.18(b) for the lower volume. Shown is the spot size measured in the horizontal

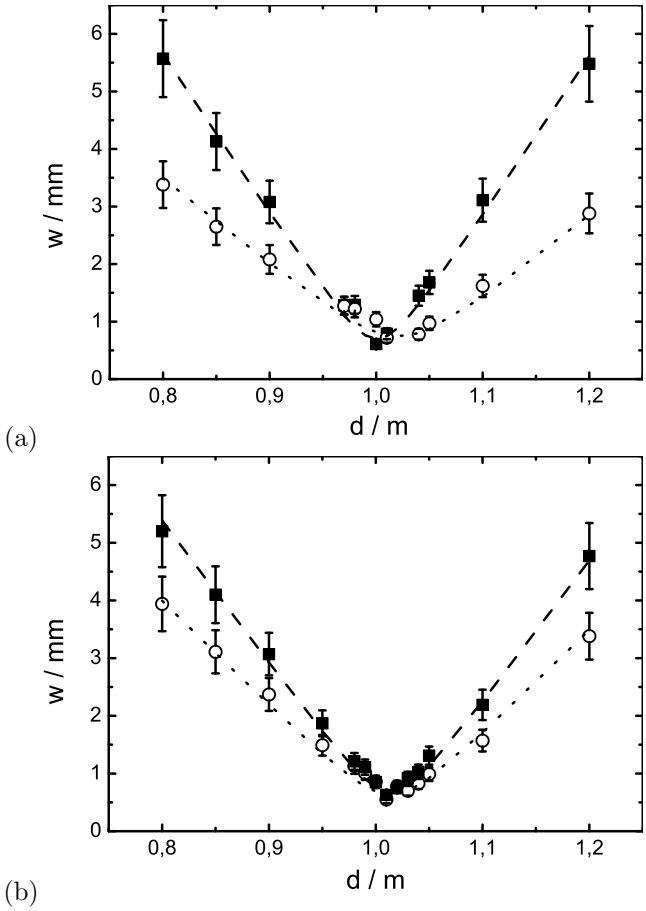

Figure 5.18: Spot size, w, of the laser beam emerging (a) from the upper volume and (b) from the lower volume measured as function of the distance, d, to the focusing lens (f = 100 cm). ■ *: horizontal axis,* ○ *: vertical axis. Lines are drawn to guide the eye.*

(filled symbol) and vertical plane (open symbol), respectively. A spot size in the focus of the lens of $w_{0,x} = (800 \pm 120)$ μm for the horizontal and $w_{0,y} = (750 \pm 110)$ μm for the vertical plane is measured for the lower volume. For the upper volume a similar result is found with $w_{0,x} = (700 \pm 100)$ μm and $w_{0,y} = (750 \pm 120)$ μm. We find the beam divergence for the lower volume to be $\Theta_x = (0.8 \pm 0.1)$ mrad and $\Theta_y = (0.8 \pm 0.1)$ mrad. For the upper volume $\Theta_x = (0.7 \pm 0.1)$ mrad and $\Theta_y = (0.8 \pm 0.1)$ mrad are obtained.

The determined beam divergence of the KrCl laser is found to be lower by a factor of four compared to a XeCl laser with comparable discharge and resonator dimensions [10, 76] that has shown an excellent discharge quality. A beam divergence of 3 mrad has been reported for that XeCl laser when equipped with a plane-plane resonator, generating laser beams with a comparable beam cross section [10, 75]. Taking into account that a factor of 1.5 in this improvement can be explained by the shorter wavelength (308 nm for XeCl vs. 222 nm for KrCl), this low beam divergence means that the spatial quality of the KrCl discharge is comparable or even better than of the XeCl discharge. Consistent with this, the discharge appears homogeneous in a visual inspection through the transverse windows of the discharge cell.

5.5 Summary

In this chapter, we demonstrated successfully the first long-pulse discharge pumped high-pressure KrCl laser with a high discharge quality. As a result of the high discharge quality, laser pulses with a long duration of 150 ns were achieved.

As a first test of the basic performance, we operated our discharge system as XeCl laser to compare it with previously realized XeCl lasers. Although neither the resonator nor the PFN were optimized, we obtained laser pulses with a long duration of 130 ns with a high specific output energy of 1 J/l and a high efficiency of 3%, demonstrating the good performance of the system. In comparison to other XeCl lasers, the efficiency is already found to be in the upper range. The specific output energy

is only somewhat lower than in literature, however, an increase for our laser can be achieved by increasing the duration of the mainpulse and optimizing the resonator.

For the operation as KrCl laser, we investigated in detail the dependence of discharge and laser parameters on the gas composition and pump parameters. We found as a result of this investigation that the maximum laser pulse duration and energy increased when a lower Kr partial pressure of 90 mbar (instead of 130 mbar) is used. This lower Kr concentration is supposed to be favorable as the collisional quenching of the upper state population and the halogen donor consumption slows down.

Using the identified optimum conditions, we achieved to excite and sustain very homogeneous discharges in KrCl that resulted in the generation of pulses with a long duration of 150 ns. When pumped with 340 kW cm^{-3}, a beam divergence of smaller than 1 mrad was measured for both output beams when a plane-plane resonator was used with 10% outcoupling. A comparison with a long-pulse XeCl laser showed that the achieved discharge homogeneity is as high as in XeCl lasers. This observation is also supported by low pulse-to-pulse fluctuations of the laser energy and confirmed by transverse inspection of the discharge.

Chapter 6

KrCl gain measurement

The successful operation of all lasers towards the desired specifications is governed by properly matching the properties of its two essential components, the laser gain medium and the laser resonator. This means that designing a laser is not possible without a prior detailed characterization of the gain medium. Only after such a characterization, which has to comprise the so-called net gain, and the saturation intensity, a resonator with matching (optimum) properties can be designed, such as to achieve a desired beam quality, laser pulse duration, and output energy, for specific applications. For this reason, we present here measurements of the named properties of the KrCl gain medium under long-pulse excitation.

So far, the net gain and saturation intensity of KrCl lasers has been measured only for short-pulse systems, with pump pulse durations of a few tens of nanoseconds [31,77,78]. A graph, summarizing these measurements is shown in Fig. 6.1. The graph shows the KrCl net gain as a function of the pump power density. Power densities of several to several tens of MW cm^{-3} have been used in these experiments. However, it can be seen that in the range below 1 MW cm^{-3}, where long-pulse discharge lasers are typically expected to operate, no prior experimental data are available, due to the lack of a reliable long-pulse KrCl laser. In a simplified picture based on an extrapolation

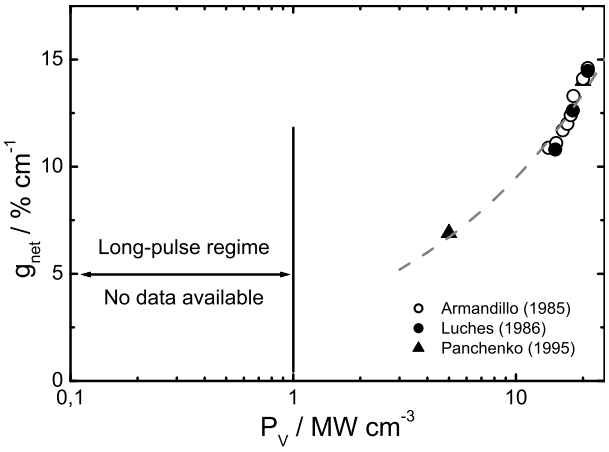

Figure 6.1: Summary of the measured net gain for short-pulse KrCl lasers. Typical pulse durations of the corresponding laser pulses are in the order of a few up to a few tens of nanoseconds. The line is drawn to guide the eye.

towards zero pump power one could yield values of more than 3% cm^{-1}. Such gain values would still be sufficient to generate near diffraction-limited KrCl laser beams, e.g., when using confocal, unstable resonators [75, 79, 80], which introduce losses in the range of $1 - 2\%$ cm^{-1} [59]. Seen the lack of gain data with long-pulse (i.e., low pump power density) pumping, the question on how to design a long-pulse KrCl laser has remained largely unclear.

In this chapter, we present the first experimental measurements on the properties of the gain in long-pulse KrCl discharges and successfully compare them with a theoretical model. Section 6.1 discusses the experimental set-up employed in our measurements. Thereafter, we describe the measurement of the spontaneous fluorescence power, which is proportional to the number density of the upper laser level in KrCl*. Also, the dependence of the KrCl* fluorescence power with the pump power density and halogen donor concentration is discussed in Sec. 6.2. The section is followed by the measurement of the peak net gain (Sec. 6.3) over a range of pump conditions and

gas compositions. The first measured values of the saturation intensity, small-signal gain, and losses for long-pulse excited KrCl discharges are presented in Sec. 6.4. In particular, the saturation intensity yields unambiguous information to identify the scale on which collisional processes reduce the population density in KrCl discharges due to its direct dependence on collisional processes (see also Sec. 2.1). Additional measurements on the dependence of the pulse duration and energy of the laser on the resonator feedback are presented in Sec. 6.5. After having characterized in the described manner the properties of the gain medium, in Sec. 6.6, we present a time-dependent resonator model in order to predict the temporal shape of the laser pulse and the pulse energy. We find a good agreement between the measured and calculated values of the pulse duration and pulse energy, which will be shown in Sec. 6.7. Concluding remarks are given in the end of the chapter (Sec. 6.8).

6.1 Experimental setup

The measurements of the gain and the spontaneous fluorescence were performed on the long-pulse KrCl laser described in Ch.5. Figure 6.2 shows a schematic sideview of the three-electrode discharge laser and the oscillator-amplifier set-up used to measure the gain. To generate the probe pulse, the upper volume is employed as the oscillator. Its stable resonator consists of a highly-reflecting, curved mirror (R_c = 5 m) and a flat output coupler with a transmission of 10%. Due to restrictions set by the open high-voltage, the resonator length is 150 cm, while the length of the gain medium, as defined by the discharge length, is 80 cm. To inject the laser pulse into the amplifier, we use a set of plane mirrors as beam transfer, as is indicated in Fig. 6.2. To provide a probe beam with low divergence (and, thus, constant intensity) with a radius that is sufficiently small to probe the central section in the amplifier, an aperture (A) is placed inside the resonator, in front of the output coupler, to suppress the build-up of higher order transverse modes. With the aperture inserted, the laser generates a probe beam with a radius of approximately 0.3 cm, which does not change significantly on the length of the amplifier. Typically, probe laser pulse energies of 1-5 mJ with pulse

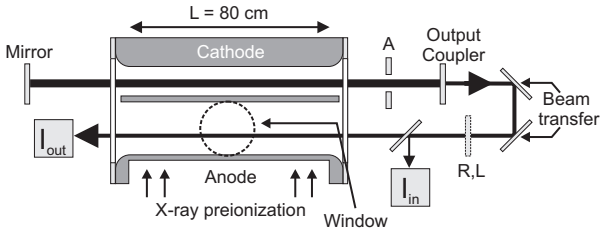

Figure 6.2: Schematic sideview of the three-electrode laser and the oscillator-amplifier configuration used to measure the gain. Upper discharge section: oscillator, lower section: amplifier. The gain length in both sections is 80 cm. Reflective attenuators (R) or a focusing lens (L) are inserted to variably decrease or increase the input intensity to the amplifier. A side window (dashed circle) allows the observation of the transversal emitted fluorescence. A: aperture.

durations of 150 ns (FWHM) were injected into the amplifier to measure the net gain of the amplifier.

The probe beam travels collinearly through the amplifier. Plane partial reflectors, with reflectivities of $R = 0.8, 0.7, 0.5$ were inserted into the beam path (R) to vary the probe beam power. When higher probe beam intensities were required, an additional lens with a focal length of 1 m was placed in the beam path (L). In this case, the probe beam had a near constant beam radius of 0.1 cm over the length of the gain medium.

As shown in the previous chapter, the laser is pumped with power densities between 200-650 kW cm^{-3}. The discharge volume of 0.6 l contains HCl/Kr/Ne gas mixtures with a total pressure of up to 3.5 bar. Under these circumstances, laser pulse durations of 150 ns (FWHM) with a pulse energy of 87 mJ were observed. The optical signals of the input probe power and output power were recorded employing a bandpass filter ($\lambda_c = (214 \pm 12)$ nm) in combination with a photodiode ($\tau_{\text{rise}} = 2$ ns), attached to a digital oscilloscope. The spectral response of the photodiode and the transmission of the bandpass filter were known. Parasitic signals due to the high-voltage switching were eliminated by subtracting the, independently measured, noisy background from

the original signals during the data processing.

In order to investigate the excited state (upper laser level) population, the $KrCl^*$ number density and its temporal evolution was measured via the transversal emitted fluorescence of the discharge at 222 nm. For this, a part of the fluorescence was observed through a fused silica window in the sidewall of the lower discharge section of the laser vessel, as shown in Fig. 6.2. The fluorescence was passed through a bandpass filter and detected by a photodiode. To monitor the build-up of the laser field with respect to the dynamics of the population of the upper laser level, we first block the resonator mirrors and monitor only the spontaneous fluorescence. Thereafter, both the fluorescence and the laser pulse are recorded as the laser oscillates with unblocked mirrors.

6.2 Spontaneous fluorescence

We determine in the following the number density of $KrCl^*$. The number density n_{KrCl^*} is calculated according to [21]:

$$n_{KrCl^*}(t) = \frac{4\pi\tau_r}{h\nu}\frac{\Delta P(t)}{\Delta\Omega}, \tag{6.1}$$

where $h\nu = 5.6$ eV is the photon energy, ΔP is the power detected at $\lambda = 222$ nm, emitted from the discharge volume (in units of W/cm^3) into the solid angle $\Delta\Omega = 1.9\times10^{-3}$ sr covered by the detector. The discharge volume, which is observed through the side window from the position where the photodiode is located, is approximately 5 cm^3. As radiative lifetime, $\tau_r = 19$ ns is taken for $KrCl^*$ from literature [78].

As a result of the calculation, Figure 6.3 shows a typical example of the measured temporal shape of the $KrCl^*$ number density (black line) and the discharge current (grey line) for a pump power density of 300 kW cm^{-3}. For this measurement, both resonator mirrors are blocked. The mainpulse capacitance (800 nF) was charged to a voltage of 10.5 kV. It can be seen that, initially, between 0 and 100 ns, the current is about -5 kA due to the charge transfer between C_{pp} and C_{peak}. The prepulse (not

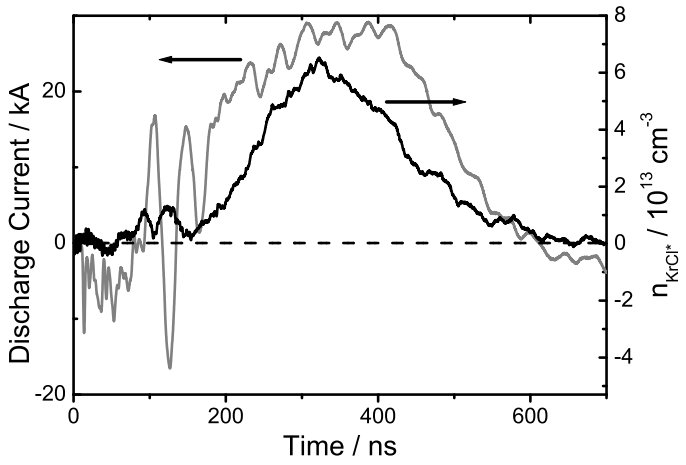

Figure 6.3: Number density of $KrCl^*$ (black line) and discharge current (grey line) of the lower discharge volume measured as function of time. The cavity mirrors are blocked (see text). $P_V = 300$ kW cm^{-3}, HCl/Kr/Ne = 1/90/3410 mbar.

shown) initiates the discharge in both volumes consecutively, which can be seen as the rapid increase of the current from 0 to 15 kA, followed by an oscillation between -16 kA and +14 kA (until 150 ns). Following this oscillation, the discharge current increases to a peak value of almost 30 kA between 300 ns and 400 ns. The full width at the zero crossing of the current pulse is 420 ns, limited by the pulse length of the driving circuit. In the graph showing the number density, two small peaks are observed around $t = 100$ ns. Thereafter, the number density increases nearly linear until it reaches a peak value of $n_{\mathrm{KrCl}^*} = 7 \times 10^{13}$ cm^{-3} after 150 ns relative to its onset ($t \approx 250$ ns). At times after 300 ns the number density decreases and ends at about 600 ns. In comparison to the current, the number density starts to decrease 100 ns prior to the decay of the current signal.

In the following, we explain the observed rapid oscillation in both signals. The current oscillation is caused by the application of the prepulse, which charges the peaking capacitance connected in parallel to the discharge volumes. As a result of this current,

a low $KrCl^*$ number density develops prior to the main discharge, as can be seen by the two peaks in the graph.

We want to give a qualitative explanation for the early decline of the number density. Although discharge inhomogeneities can be responsible for the decreasing number density, we exclude this possibility because our observations show that the discharge was very homogeneous during the entire pump duration. An explanation is, therefore, to be found in the discharge kinetics. In KrCl discharges, the main reaction channel for the formation of excimer molecules is ion-ion recombination [48]:

$$Kr^+ + Cl^- + Ne \rightarrow KrCl^* + Ne \tag{6.2}$$

$$Kr_2^+ + Cl^- + Ne \rightarrow KrCl^* + Kr + Ne. \tag{6.3}$$

Chlorine ions are mainly formed via electron attachment to HCl and HCl(v). However, the hydrogen and chlorine ions do not have a recombination channel back to HCl. Furthermore, to maintain a homogeneous discharge over durations of several hundred nanoseconds, a comparatively low HCl concentration is required. From this, we conclude that the number density is limited by the consumption of HCl during the discharge, which decreases the concentration of Cl^- ions (halogen donor depletion).

To obtain a preliminary estimation for the gain, which we can compare later with directly measured values, we determined the gain coefficient that corresponds to the peak number density in Fig. 6.3. The laser transition in KrCl is a bound-free transition with a repulsive ground state. In this case, the gain can be written as [21]:

$$g = \sigma_{SE} n_{KrCl^*}, \tag{6.4}$$

where g is the gain coefficient and σ_{SE} is the stimulated emission cross section. Values of the stimulated emission cross section range from 0.8 $Å^2$ to 2.2 $Å^2$ [27, 78]. Taking these values suggests that, in our setup, the gain is between 0.6 and 1.5% cm^{-1} for a power density of 300 kW cm^{-3}.

In order to identify experimental parameters that could improve the laser pulse du-

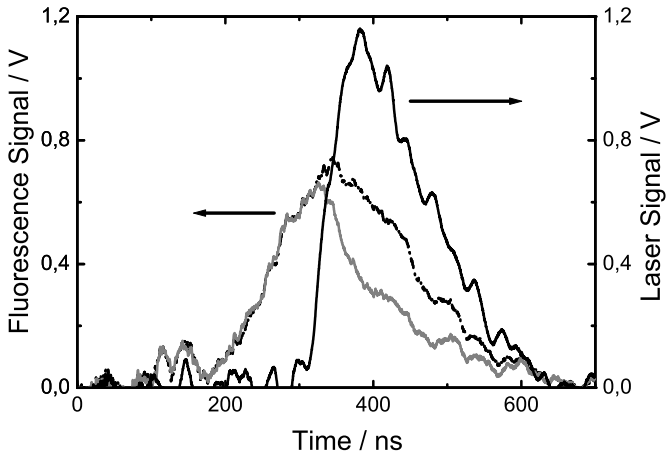

Figure 6.4: Laser pulse (solid black line), the sidelight as the laser oscillates (solid grey line), and the sidelight as the resonator is blocked (dashed line) of the lower discharge volume measured as function of time. The discharge conditions are the same as in Fig. 6.3. The resonator consists of a curved mirror ($r_c = 5$ m, $R \approx 1$) and a flat output coupler ($R = 0.9$).

ration and energy, we compared the temporal evolution of the laser pulse with the transversely emitted spontaneous fluorescence (sidelight) in the lower discharge volume. Figure 6.4 shows the laser pulse (solid black line), the sidelight as the laser oscillates (solid grey line), and the sidelight when the resonator is blocked (dashed line) of the lower discharge volume measured as function of time. The signals are measured for same gas pressure and under the same discharge conditions as presented in the previous section. During the first 300 ns, the sidelight with and without the laser overlap, shown as an approximately linear increase with time. However, when the laser mirrors are unblocked, the sidelight begins to decrease at $t = 320$ ns, falling to 50% of its peak value within 30 ns. This coincides in time with the rising edge of the laser pulse, as can be seen from the graph in Fig. 6.4. After the reduction of the sidelight, the fluorescence is observed to continue to decay during the following 240 ns until it ends.

The comparison between the temporal evolution of the fluorescence and the laser pulse allows one to also obtain a qualitative statement on the gain of the laser, in comparison to short-pulse lasers. It can be seen from Fig. 6.4 that the build-up of the laser takes 150 ns with respect to the onset of the fluorescence, when taking the time delay between the 10% peak values of the rising edge of the signals. The large time difference, which is about 10-times longer than typically found in short-pulse lasers, is an indication that the laser operates in a regime with a comparatively lower gain.

The early decrease of the population of the upper laser level, as observed by the decrease of the fluorescence at 222 nm, can be identified as the limiting factor of the pulse duration as can be seen in Fig. 6.4. The graph shows that only shortly after the sidelight starts to decrease, the laser signal reaches its maximum value, followed by its immediate decay. Thereby the peak of the laser pulse coincides with the falling edge of the spontaneous fluorescence, which was observed without the laser oscillating. This observation shows that the laser signal reaches its maximum during a time, when the upper laser level already depopulates.

Based on these observations, it should be possible to extend the laser pulse duration by shortening the build-up time. For this, the gain, which is associated with the $KrCl^*$ number density, must be increased, which could be done via a higher pump power density. To experimentally investigate this possibility, we measured the peak $KrCl^*$ number density and the fluorescence pulse duration as a function of the pump power density (P_V), ranging from 260 kW cm^{-3} to 600 kW cm^{-3}. The power density was increased using either higher mainline voltages or decreasing the width of the discharge volume. The spontaneous fluorescence was measured with a blocked laser resonator. For these experiments, a gas composition of HCl/Kr/Ne = 1/90/3410 mbar was used. The experimental results are shown in Fig. 6.5. It can be seen that the number density (and thus the gain) indeed increases with the pump power density, although the increase is seen to be less than linear: it starts from a value of 6×10^{13} cm^{-3} to almost 9×10^{13} cm^{-3}, as the power density is increased from 260 kW cm^{-3} to 580 kW cm^{-3}. This suggests that the laser pulse energy and duration may be increased further by increasing the power density further. However, Fig. 6.5 also

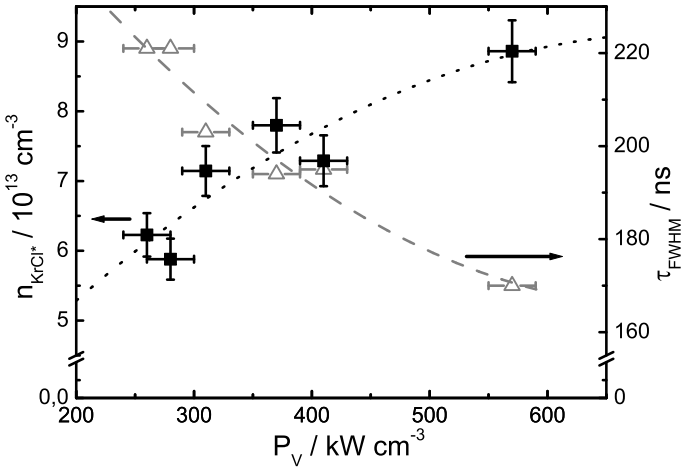

Figure 6.5: Pulse duration, τ_{FWHM}, of the spontaneous fluorescence (△) and peak $KrCl^*$ number density, n_{KrCl} (■), with increasing pump power density, P_V, and blocked cavity. HCl/Kr/Ne = 1/90/3410 mbar. The lines are drawn to guide the eye.

shows that the FWHM duration over which fluorescence is observed, i.e., over which the increased number density is available, decreases almost inversely proportional to P_V. The duration shortens from 220 ns to 170 ns as the power density increases from 260 kW cm^{-3} to 600 kW cm^{-3}. We explain these results to be a consequence of the faster electron attachment to HCl (halogen donor depletion) due to the increased electron number density in the discharge, when the current density is increased for a higher power deposition.

These experiments illustrate that, in order to maximize the duration and the energy of KrCl laser pulses, one has to compromise between two limiting situations. On one hand, a low gain causes a long build-up time (and thus shortens the pulse) but, simultaneously, the depletion of the halogen donor reduces, giving the upper state population a longer duration, which lengthens the pulse. In order to come to a more quantitative conclusion on the best compromise between these two effects, it is necessary to determine quantitatively both, the saturation intensity and the peak net gain, as will be shown in the next section.

6.3 Peak gain

The measurement of gain and saturation intensity in long-pulse KrCl discharges can, in principle, be done by using both the laser oscillator or the amplifier shown in Fig. 6.2. However we expect that such measurements would yield less reliable data with the oscillator, because here amplification in single passes are more difficult to separate from the resonator feedback, and because the resonator-internal light intensity changes rapidly over many orders of magnitude during round trips through the resonator. In order to avoid the correspondingly complex interpretation of data, we decided to perform gain measurements in a single pass through the amplifier discharge, and use the oscillator and additional optics to provide suitable probe pulses (see Fig. 6.2). Also, since the number of KrCl* molecules depends on the halogen donor concentration, we measured the net gain, which is the gain reduced by transient and static losses, for HCl partial pressures of 0.8 mbar, 1.0 mbar and 1.5 mbar.

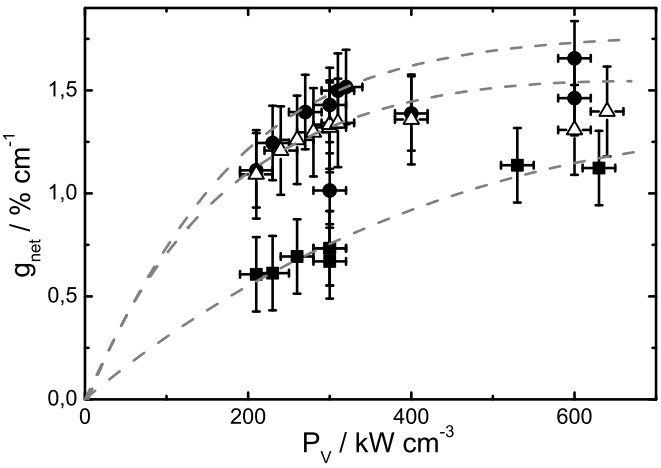

Figure 6.6: Measured peak gain as function of the specific pump power density for constant partial pressures of $p_{\mathrm{Kr}} = 90$ *mbar and* $p_{\mathrm{Ne}} \approx 3.5$ *bar.* ■ *:* $p_{\mathrm{HCl}} = 0.8$ *mbar,* △ *:* $p_{\mathrm{HCl}} = 1.0$ *mbar,* ● *:* $p_{\mathrm{HCl}} = 1.5$ *mbar. The lines are drawn to guide the eye.*

The partial pressures of Kr and Ne were kept constant at 90 mbar and 3.5 bar, respectively. To prevent gain saturation, the input intensity of the probe laser was kept at approximately 60 kW cm^{-2}, which is far below the saturation intensity of 580 kW cm^{-2} expected from calculations [78]. To determine the peak net gain (called peak gain hereafter), which is the highest net gain during an observed pulse duration, the measured output power, $P_{\mathrm{out}}(t)$, of the amplified pulse is divided by the input power, $P_{\mathrm{in}}(t)$. Then, the peak gain is determined from the time-dependent function $L^{-1} \ln[P_{\mathrm{out}}(t)/P_{\mathrm{in}}(t)]$, where L is the length of the gain medium.

Figure 6.6 shows the measured peak gain as a function of the pump power density. It can be seen that the gain increases with increasing pump power density for all employed gas mixtures until saturation sets in. It can also be seen that the gain increases at a higher HCl partial pressure. For a partial pressure of $p_{\mathrm{HCl}} = 0.8$ mbar, the gain increases almost linearly from 0.6% cm^{-1} when pumped with 200 kW cm^{-3} to 1.1% cm^{-1} when pumped with 600 kW cm^{-3}. Moreover it can be seen

that raising the halogen pressure to 1 mbar results in an doubling of the gain to 1% cm^{-1} for $P_V = 220$ kW cm^{-3}. However, in contrast to the gain measured for a lower HCl pressure, a saturation of the gain is observed to approximately 1.4% cm^{-1} for a further increase of the pump power density to 600 kW cm^{-3}. A similar dependence on P_V, although shifted to slightly higher values is found when increasing the HCl partial pressure to 1.5 mbar. At pump power densities between 200 kW cm^{-3} and 300 kW cm^{-3}, the gain is indistinguishable to that obtained from 1.0 mbar of HCl. Also, as the pump power density is increased, a similar saturation of the gain is observed. Here, a maximum of 1.6% cm^{-1} is measured, when employing a pump power density of 640 kW cm^{-3}. We suggest that the differences in the increase of the gain when adding HCl arises from an increase of the absorption losses at 222 nm. As it has been shown in other KrCl lasers, HCl, HCl(v), and Cl^- have absorption bands in the region of the laser transition [27, 81], where approximately 50% of the absorption losses arise from Cl^- [27]. Since Cl^- is formed due to electron attachment to HCl, the absorption is very likely to increase when the HCl partial pressure is increased.

In this section, we have determined for the first time the gain of KrCl discharges in the, for long-pulse lasers important, power density range below 1 MW cm^{-3}. These measurements contribute significantly to the picture of the gain of KrCl discharges, as it was shown in Fig. 6.1, which had been confined so far to short-pulse lasers with high pump power densities.

6.4 Small-signal gain, losses and saturation intensity

In previous work, the determination of the central gain parameters in KrCl lasers, which are the saturation intensity, small-signal gain, and losses, has so far been limited to the short-pulse lasers [78]. Here, by experiments employing the three-electrode laser in the oscillator-amplifier scheme, these parameters will be obtained for the first time for such long-pulse lasers. In our corresponding experiments, the pump power

density was kept constant, while the probe pulse intensity was varied. This allows the gain medium to be probed with different intensities while the, pressure and power density dependent, collisional quenching rate of excited KrCl is unchanged. These measurement were repeated for increasing P_V. A gas composition of HCl/Kr/Ne = 1/90/3410 mbar was used as laser gas mixture. A plane-concave resonator with an output coupler transmission of 10% was employed as oscillator.

The small-signal gain, loss coefficient, and saturation intensity were calculated according to the analysis described by Rice and others [82]. This description is based on a steady-state approximation of the amplifier [83], where the time constants of the processes in the laser are short compared to the duration of the pump pulse as it is in our case, where the lifetime of the upper level is 19 ns, while the pump pulse duration is much longer ($\approx$ 400 ns). As the probe beam with input intensity $I_{in} = I(0)$ enters the gain medium (see Fig. 6.2), it is amplified along the path x (see Sec. 6.6, Fig. 6.9):

$$\frac{\partial I(x)}{\partial x} = I(x)(g - \alpha), \tag{6.5}$$

with the total losses, α, which include static and transient losses (see also Sec. 6.6), and the gain, g, defined as:

$$g = \sigma_{SE}(N_2 - N_1) = \frac{g_0}{1 + \frac{I}{I_{sat}}}, \tag{6.6}$$

where N_2 is the number density of the upper laser level and N_1 is the ground state population. For KrCl lasers, $N_1 = 0$, since the ground state is strongly repulsive and, thus, not stable.

After passing through a gain region of length L, the pulse has the intensity $I_{out} = I(L)$, given by the integral of Eq. 6.5 over the interval $x = 0$ and $x = L$. Evaluating the integral yields a transcendental equation:

$$0 = g_0 L - \alpha L + \ln\left(\frac{I_{in}}{I_{out}}\right) + \gamma \ln\left(\frac{I_{out} - I_{sat}(\gamma - 1)}{I_{in} - I_{sat}(\gamma - 1)}\right), \tag{6.7}$$

where $\gamma = g_0/\alpha$. In our case, where $I_{\rm in}$ and $I_{\rm out}$ are much less than $I_{\rm sat}(\gamma-1)$, Eq. 6.7 can be simplified, such that the extracted intensity, $I_{\rm out} - I_{\rm in}$, depends on the gain parameters, the input intensity, and the output intensity:

$$I_{\rm out} - I_{\rm in} \cong \frac{\gamma - 1}{\gamma} I_{\rm sat} \left[g_0 L - \alpha L - \ln\left(\frac{I_{\rm out}}{I_{\rm in}}\right)\right]. \tag{6.8}$$

The extracted intensity of the probe pulse is plotted against $\ln(I_{\rm out}/I_{\rm in})$. The parameters g_0, α, and $I_{\rm sat}$ are determined by fitting a linear function to the data points. The values obtained for $I_{\rm sat}$, α, and g_0 are shown in Fig. 6.7. Figure 6.7(a) shows that the saturation intensity increases from $I_{\rm sat} = (0.8 \pm 0.4)$ MW cm^{-2} to (3.4 ± 1.0) MW cm^{-2} as the pump power density increases from 320 kW cm^{-3} to 640 kW cm^{-3}. Because the current density was increased as only parameter, we conclude that collisional quenching of KrCl* by electrons,

$$\mathrm{KrCl}^* + \mathrm{e}^- \longrightarrow \mathrm{Kr} + \mathrm{Cl}^-, \tag{6.9}$$

is mainly responsible for the reduction of the effective upper state lifetime and, thus, the increase of the saturation intensity. To support this conclusion, we want to give in the following an estimation of the lifetime of collisional quenching by electrons, τ_Q, using quenching rate constants that have been determined for XeCl and KrF lasers of 1×10^{-7} cm^3/s [35] and 3×10^{-8} cm^3/s [84], respectively. Using these values, we want to calculate the quenching lifetime, τ_Q, according to [21]:

$$\tau_Q = \frac{1}{k_{Q,e} n_e}, \tag{6.10}$$

where $k_{Q,e}$ is the rate constant for collisional quenching by electrons and n_e is the electron density. The electron density is calculated for the peak of the power deposition:

$$n_e = \frac{I_{\rm peak}}{q_e v_d A}, \tag{6.11}$$

where q_e is the electron charge, v_d the drift velocity, and A the discharge area. The drift velocity, $v_d = \mu_e E$, is given by the electric field, E, and the electron mobility, μ_e,

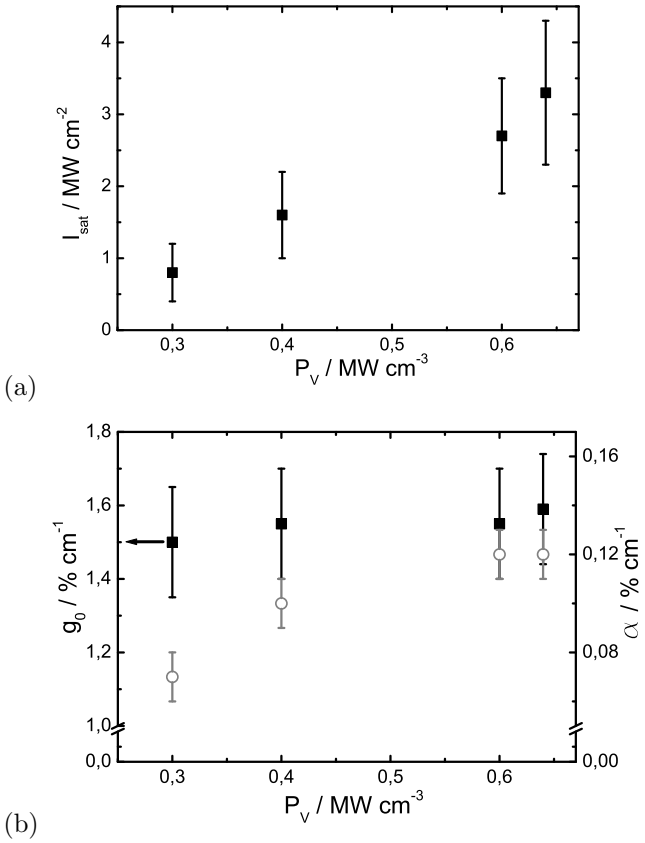

Figure 6.7: (a) Calculated saturation intensity, I_{sat}, and (b) small-signal gain (filled squares) and losses (open circles) as a function of the specific pump power density, P_V. HCl/Kr/Ne = 1/90/3410 mbar.

in neon. Firstly, to determine the drift velocity, we calculate the steady-state electric field, using $d = 3.7$ cm and $U_{\mathrm{ss}} = 4.1$ kV (see Sec. 5.3.2), from which we obtain $E_{\mathrm{ss}} = 1.1$ kV cm^{-1}. Using this value, from tabulated values for a neon pressure of 3.5 bar [30], we determine $v_d = 0.63 \times 10^6$ cm s^{-1}. Finally, we calculate for a discharge area of 160 cm^2 and $I_{\mathrm{peak}} = 31.5$ kA, as measured for $U_{\mathrm{PFN}} = 10.5$ kV and $p_{\mathrm{HCL}} = 1$ mbar, an electron density of $n_e = 2 \times 10^{15}$cm^{-3}. As a result, we obtain a lifetime of $\tau_Q(\mathrm{XeCl}) = 5$ ns and $\tau_Q(\mathrm{KrF}) = 17$ ns. Both values are shorter than or comparable to the radiative lifetime of the excited state of KrCl* (≈ 19 ns) and, thus, a reduction of the effective lifetime according to Eq. 2.14 can be expected. Therefore, we consider collisional quenching by electrons to be a relevant loss mechanism in KrCl discharges, in contrast to long-pulse XeCl lasers [69].

From Fig. 6.7(b) we find that the small-signal gain remains almost constant in the investigated range of power density. For an excitation rate of 320 kW cm^{-3}, the small-signal gain is calculated to be $g_0 = (1.50 \pm 0.12)\%$ cm^{-1}. A similar value of $(1.60 \pm 0.13)\%$ cm^{-1} is calculated for a power density of 640 kW cm^{-3}. In contrast, the loss coefficient is found to increase strongly with the power density, compared to the small-signal gain. We calculated a loss coefficient of $(0.07 \pm 0.01)\%$ cm^{-1} for a power density of 320 kW cm^{-3}. The losses increase to $(0.12 \pm 0.01)\%$ cm^{-3} when the laser is pumped at 640 kW cm^{-3}.

6.5 Resonator feedback

Measurements with various different resonator output coupler transmission were carried out to achieve the maximum pulse energy, using the previously determined optimum gas composition (HCl/Kr/Ne = (1/90/4310) mbar)) while the PFN was charged to 11.7 kV (see Ch.5). These measurements employed the lower discharge volume as laser medium. The output coupler reflectivity was reduced in steps from $R_{\mathrm{OC}} = 0.9$ to 0.8 and 0.7. In this experiment, lower reflectivities were not employed as we found in previous experiments that the pulse energy and duration decreases for $R_{\mathrm{OC}} < 0.7$.

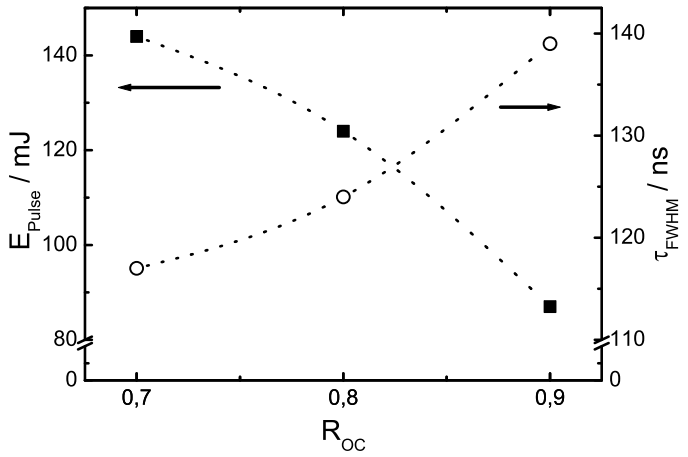

Figure 6.8: Laser pulse energy (■) and pulse duration (○) as function of the output coupler reflectivity, R_{OC}. Gas mixture: HCl/Kr/Ne with partial pressures of (1/90/4010) mbar.

The measured pulse energies and durations as a function of the output coupler reflectivity are shown in Fig. 6.8. It can be seen that a pulse energy of 85 mJ (filled symbol) was achieved using a 90% reflective output coupler and that the corresponding pulse duration amounts to 139 ns (FWHM, open symbol). The output energy increased to 144 mJ as R_{OC} was reduced to 70%, while the laser pulse duration decreased from 139 ns to 117 ns. The maximum pulse energy corresponds to a specific pulse energy of 0.45 J/l and a laser efficiency of 0.63% based on the energy deposited in the volume. Note that this is a 20% increase of the efficiency and pulse duration compared to what had previously been achieved with KrCl lasers of similar large volume [58].

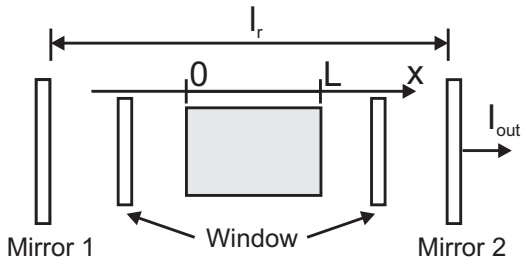

Figure 6.9: Schematic overview of the resonator. The optical field is amplified in the discharge pumped region (grey area) on the length L. The resonator consists of mirrors, separated by a distance l_r, with a reflection coefficient R_1 and R_2 and transmission coefficients T_1 and T_2. Windows seal the laser gas off from the ambient air. The laser is coupled out through mirror 2.

6.6 Resonator model

Further increase of the laser pulse energy and pulse duration via optimization of the laser parameters, such as the resonator length, can be done in a numerical study, which allows to change easily the parameters over a wide range. However, accurate modeling of a discharge pumped laser would require time consuming calculations of the discharge dynamics in order to describe the spatial distribution of the light and gain inside the resonator. Another approach, as will be shown in this section, is to use experimentally determined values that describe the amplification properties of a discharge, i.e., gain and saturation intensity, which are used as input parameters in a simple laser model [20] that simulates the time evolution of a laser pulse. Although the discharge dynamics are neglected in this model, it will be shown at the end of this chapter that, nevertheless, the pulse duration and pulse energy can be modeled in rather good agreement with the experimental data, which justifies the named simplifications of the model.

For referencing to the experimental laser parameters, the scheme of the resonator is shown in Fig. 6.9. The laser resonator is formed by two mirrors, separated by a

distance l_r, where mirror 2 is used for output coupling a part of the radiation, while mirror 1 is highly reflective, as was the case in the experiments. The influence of two windows (inside the resonator, to seal off the gas volume of the discharge laser), i.e., their transmission losses, was neglected because these losses were measured to be small compared to the output coupling used. In the mean-field approximation [19], the temporal development of the resonator-internal photon flux, ρ, can be described by a rate equation:

$$\frac{d\rho}{dt} = c\,\rho\,\left[(g-\alpha_T)\,\frac{L}{l_r} - \Gamma - \alpha_s\right] + \frac{\Omega}{4\pi}\frac{N_2}{\tau_r}. \tag{6.12}$$

The factor L/l_r, effectively, acts to distribute the net gain over the length of the resonator, c is the speed of light, L is the length of the gain medium, g is the time-dependent gain defined by Eq. 6.6, α_T and α_s denote time-dependent and the static absorption losses, respectively. The reason why there should be time-dependent losses present is that, next to providing population inversion at the laser wavelength, the discharge also generates a number of other species and populates a number of excited states, which can then (re-) absorb a certain fraction of the generated laser light. Formally, the time-dependent absorption loss, α_T, is described as the sum of all losses due to absorbing species generated during the discharge:

$$\alpha_T = \sum_i \sigma_{\mathrm{abs},i}\left[n_{\mathrm{abs},i}\right], \tag{6.13}$$

where the contribution of the i-th species is given by the product of its absorption cross section $\sigma_{\mathrm{abs},i}$ with its time-dependent concentration $\left[n_{\mathrm{abs},i}\right]$. Any static absorption, which arises, e.g., from background absorption due to gas impurities, is summarized in α_s.

The last term in Eq. 6.12 describes the contribution of spontaneous fluorescence, which is emitted into the solid angle of the oscillating resonator mode, Ω, which also contributes to the build-up of the intracavity photon flux. N_2 is the upper state population and τ_r the radiative lifetime. Γ denotes the resonator output coupling

efficiency distributed over the cavity length, given by:

$$\Gamma = -\frac{\ln(R_1 R_2)}{2l_r}, \tag{6.14}$$

where R_1 and R_2 denote the reflection coefficients of the resonator mirrors.

Equation 6.12 describes the build-up of the light field in the time domain and is independent of spatial coordinates since it is assumed that the intensity variation along the resonator length is small. Once the time-dependent photon density in the resonator is obtained from integrating Eq. 6.12, the output intensity of the laser can be calculated by multiplication with the output coupling efficiency:

$$I_{\text{out}}(t) = \Gamma l_r c \rho(t) h\nu. \tag{6.15}$$

After having obtained the time-dependent output intensity from Eq. 6.12, the pulse energy can be calculated by integrating Eq. 6.15:

$$E_{\text{out}} = A \int I_{\text{out}}(t)\, dt, \tag{6.16}$$

and multiplying with the beam cross section, A.

With this set of equations, the laser output intensity and pulse energy can be calculated, provided that the upper state population, N_2, is known as a function of time from an independent measurement, because the remaining laser parameters g_0, α_T, and I_{sat} are known from the experimental set-up, while τ_r can be taken from literature [29]. A comparison between experimentally measured pulse energies and pulse durations and values obtained using this model, is given in the next section.

6.7 Employing the resonator model

In this section, the measured laser pulse energy and duration for different output coupler values are compared with numerical results, obtained from the model described

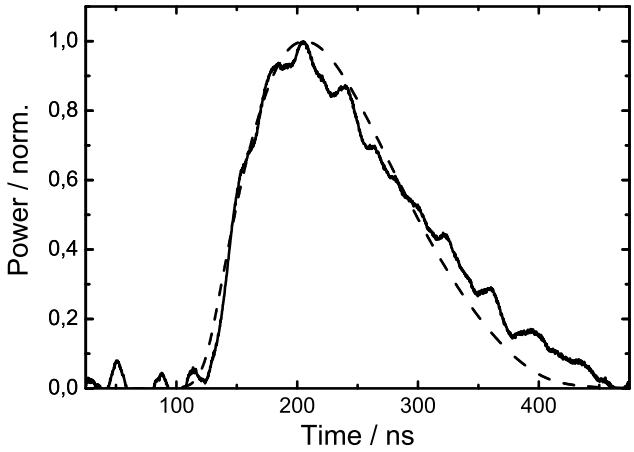

Figure 6.10: Comparison of a calculated (dashed line) and measured (solid line) laser pulse as function of time. The resonator output coupler has a transmission of 10%. Model parameters: $I_{\mathrm{sat}} = 1.1\ MW\ cm^{-2}$, $g_0 = 1.6\%\ cm^{-1}$, $\alpha = 0.07\%\ cm^{-1}$.

in the previous section.

To model the time-dependence of the gain of our KrCl laser, we employ the measured temporal shape of the $KrCl^*$ number density (Sec. 6.2). This is a good approximation, because the ground state of KrCl is repulsive and, for this reason, unpopulated. In this case, the population inversion (and thus the gain) is directly proportional to the $KrCl^*$ number density. We employ the measured pulse shape of the $KrCl^*$ number density to describe the gain, by multiplying it with a constant factor, such that the modeled peak gain is equal to the measured one.

An example of a calculated laser pulse with a duration of 154 ns (FWHM, dashed line) is shown in Fig. 6.10 and is compared to the measured laser pulse. The peak value of both pulses is normalized to unity for a better comparison. We find that the difference between the measured and the calculated pulse energy, 62 mJ and 58 mJ respectively, is better than 10%. The experimentally determined laser pulse has been

measured for a specific input power of 340 kW $cm^{-3}$and a transmission of 10% of the output coupler.

As model parameters, we used the experimental parameters of the set-up, i.e., a resonator length of 1.5 m, a gain length of 80 cm, and the named transmission of the output coupler. The solid angle Ω was calculated from the ratio of the beam cross section and the square of the resonator length. The losses ($\alpha = \frac{L}{l_r}\alpha_T + \alpha_s$) were taken as constant (0.07% cm^{-1}) during the first 180 ns, which is in accordance with the determined loss factor from measurements presented in the previous section. However, to accurately describe the reduction of the laser power, an exponential increase of the losses had to be assumed with the end of the gain pulse, which is in agreement with the oberved time-development of the figure of instability presented in Ch.4. Including this, the loss coefficient was modeled such that it reached a value of 0.12% cm^{-1}after 370 ns, which is the highest loss coefficient we determined, as shown above.

With these assumptions, good agreement between the measured and the calculated temporal pulse shape is obtained, as can be seen from Fig. 6.10. Both pulses have a similar rise time of approximately 30 ns. After reaching the peak power ($t \approx 200$ ns), both pulses decay to zero ($t \approx 450$ ns) with almost equal decay times.

In a further step, the validity range of the model is tested by comparing the measured and calculated pulse energy and duration for various values of the output coupler reflectivity. The calculated and measured laser pulse energy and pulse duration are given as a function of the output coupler reflectivity, R, shown in Fig. 6.11. In Fig. 6.11(a), the measured pulse energy (filled symbols) is observed to increase from almost zero to 92 mJ as the reflectivity of the output coupler reduces from $R \approx 1$ to 0.7. Beyond this value of the reflection coefficient, the pulse energy decreases strongly to zero for $R = 0.3$. For comparison, the calculated pulse energy is shown (open symbols). A pulse energy close to zero is calculated for $R \approx 1$, increasing to a peak value of 82 mJ for $R = 0.7$. For lower reflection coefficients, the pulse energy reduces to 11 mJ ($R = 0.3$). Although our calculated values deviate somewhat from the measurements, the agreement between the two is still very good, demonstrating the validity of the applied model.

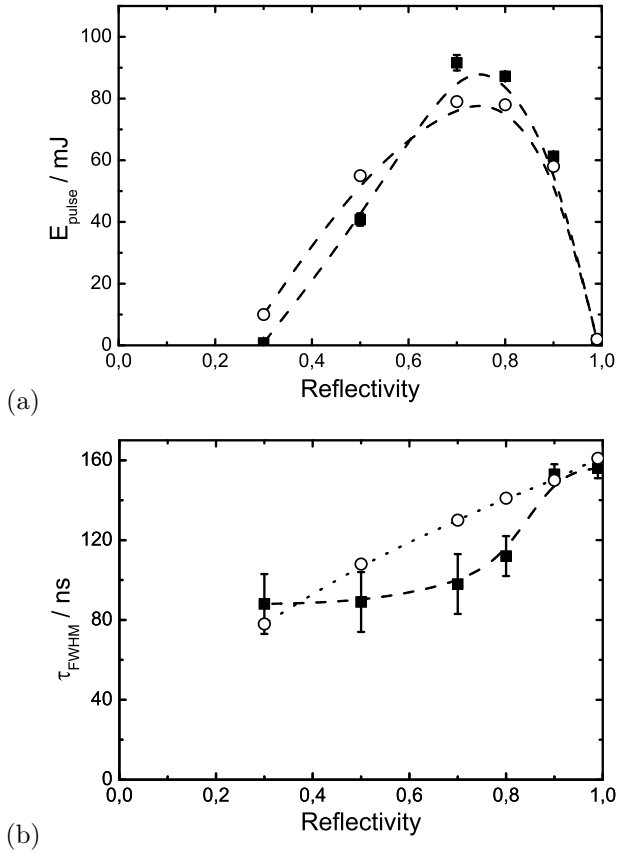

Figure 6.11: Comparison of measured (■) and calculated (○) laser pulse parameters as a function of the output coupler reflectivity, R. (a) Laser pulse energy, (b) pulse duration. Simulation parameters: $I_{\mathrm{sat}} = 1.1\ MW\ cm^{-2}$, $g_0 = 1.6\%\ cm^{-1}$, $\alpha = 0.07\%\ cm^{-1}$.

We also compare the calculated pulse duration, as can be seen in Fig. 6.11(b). Here, the measured pulse duration (filled symbols) reaches a maximum of 160 ns, with an output coupler of $R \approx 1$ or $R = 0.9$. For a reflection coefficient of 0.8, the pulse duration decreases to 110 ns and reduces further to a value of approximately 90 ns for lower values of R. The calculated pulse duration is found to decrease from 160 ns ($R \approx 1$) almost linearly to 80 ns for $R = 0.3$. The values deviate somewhat more from the measured ones compared to the energy calculation. However, the trend to shorter pulse durations with higher output coupler transmissions is in agreement with measurements. Furthermore, we find that the deviation between the calculated and the measured values is within 20%, an acceptable range, since the discharge dynamics are not taken into account with this model.

The good match of the model with the experimental data suggest that the model can be used to theoretically investigate whether the output energy and pulse duration can be further increased by changing the resonator configuration. Actually, in the experimental set-up, there are restrictions set by the open high-voltage circuit, which lead us to use a resonator length that was almost twice the size of the discharge length, while in the model the output can easily be calculated for shorter resonator lengths. In the corresponding calculations, we kept the discharge lengths constant at the experimental value of 80 cm. The calculated pulse energy and duration is shown in Fig. 6.12. As can be seen from Fig. 6.12(a), it should be possible to increase the pulse energy by 30% if the resonator length is shortened to 90 cm, which is a significant increase. We note, however, that experimentally such a modification is not straightforward. It would require to place the resonator mirrors inside the discharge vessel, close to the electrodes, which could lead to distortions of the electric field distribution in the discharge volume and would thus require a more detailed numerical study of the electric field distribution.

The pulse duration, on the other hand decreases, as can be seen from Fig. 6.12(b). However, this change was found to be only small, less than 10%, such that a long laser pulse duration is still obtained. Rather due to the nearly doubled number of roundtrips for the 90 cm resonator, it can be expected that the beam quality

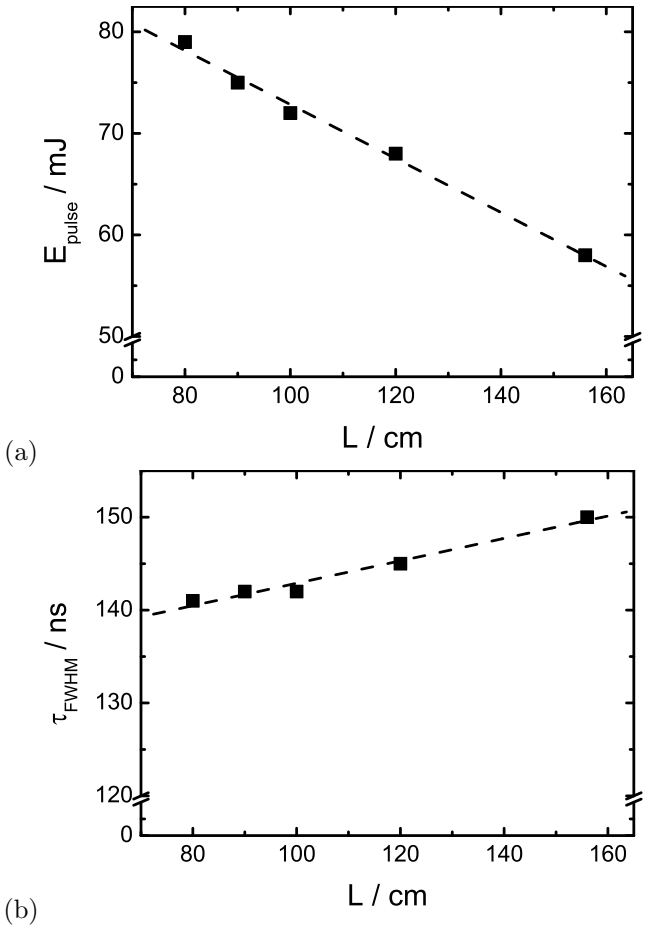

Figure 6.12: Calculated laser pulse parameters as a function of the resonator length L. (a) Laser pulse energy, (b) pulse duration. Simulation parameters: $I_{\mathrm{sat}} = 1.1\ MW\ cm^{-2}$, $g_0 = 1.6\%\ cm^{-1}$, $\alpha = 0.07\%\ cm^{-1}$.

increases. The predicted 10%-reduction of the pulse duration can be understood to be caused by two counteracting effects. The reduced round trip time of the laser pulse, on the one hand, increases the pulse duration due to a faster build-up of the laser oscillation. On the other hand, the decay rate of the light field also increases, which decreases the pulse duration. Obviously, when looking at Fig. 6.12(b), these two effects nearly compensate each other and the laser still provides a pulse duration which is significantly longer than in KrCl lasers that are known so far.

In summary, the numerical results illustrate clearly that a further improvement of the long-pulse KrCl laser should be possible with a shorter resonator. In this case, a substantial (30%) increase of the output energy should be achievable with a nearly doubled number of round trips, which would increase the beam quality.

6.8 Summary

For the first time, the peak net gain of a discharge pumped long-pulse KrCl laser has been experimentally measured. An upper limit of 1.6% cm^{-1} was observed for a HCl partial pressure of 1.5 mbar and a power deposition of 620 kW cm^{-3}. These values were obtained from a direct, time-resolved gain measurement, and are supported by calculations of the gain, using the spontaneous fluorescence at 222 nm to determine the $KrCl^*$ number density. We conclude that the observed maximum of the upper laser level number density is set by collisional quenching through electrons while increasing the pulse energy by the addition of more HCl is limited due to quenching involving the halogen donor. Also, we found that the pulse energy is limited by the depletion of the halogen donor.

From amplification measurements, we derived values for the small-signal gain, loss coefficient, and saturation intensity. We find that these parameters show a similar dependency on the power density as in short-pulse lasers, but that the values in our long-pulse laser are a factor of 2-3 lower. Such a value is, as expected, below the gain of short-pulse KrCl lasers that are typically pumped with much higher power

densities. However, a trade-off between high gain and long pulse duration is required to generate laser beams with a high spatial coherence. From the saturation intensity we find that collisional quenching reactions reduce the effective upper state lifetime, as the power density increases. Additionally, the losses, though small, are found to be higher than what would be expected from experiments using short-pulse high-power excitation circuits. Based on these measurements, it looked promising to look for a further improvement of the laser pulse duration and energy via optimizing the laser parameters, such as the strength of the output coupling from the resonator.

Using a stable resonator and by pumping the discharge under optimum conditions, a maximum specific energy of 0.45 J/l with a pulse duration of 117 ns and an efficiency of 0.63% was achieved. This is, indeed, an improvement of almost 20% in the pulse duration and efficiency for these high output energies. Also, the pulse duration increased for a resonator feedback of 90% to a value of almost 150 ns with a specific energy of 0.27 J/l.

For a further understanding and search for improvements, we modeled the laser with time-dependent rate equations for the resonator-internal photon density in the mean-field approximation. The model was found in good agreement with experimental data when time-dependent gain and loss coefficients were used as input parameters, which were found from independent measurements. A calculation of the laser pulse energy and pulse duration for various output coupler reflection coefficients were found to be in good agreement with the measured values. This suggests that the described model, in spite of its simplicity, can indeed be used to explore a further optimization, such as a short laser resonator, without the need of time consuming calculations of the discharge dynamics and the electric pump circuit.

Corresponding calculations showed that a 30% improvement of the pulse energy should be possible by reducing the resonator length to a value of about 90 cm. Although this would shorten the resonator lifetime by nearly a factor of two, we find from the model that only a minor (10%) shortening of the pulse duration is expected. Therefore, the number of round trips per pulse could nearly be doubled to increase the beam quality with, simultaneously, providing higher output energies.

Chapter 7

Summary and conclusion

In this thesis, we described the successful realization of a discharge pumped KrCl laser (222 nm) with a high discharge homogeneity, which resulted in the generation of laser pulses with a long duration of 150 ns. The laser has been pumped in the prepulse-mainpulse scheme that has been realized employing a three-electrode circuit with two discharge volumes. As a result of our investigations, we demonstrate a considerable increase of the laser efficiency, pulse duration and specific laser energy.

Discharge properties

In the first part of this thesis, we have demonstrated that long and homogeneous discharges in KrCl are possible with a duration reaching up to 300 ns. In order to perform this investigation on the discharge stability with optimum discharge conditions, that is very short rise time of both the prepulse voltage and the discharge current, we developed a low-inductive discharge test set-up. With this, we have investigated the relation between homogeneity and electrical characteristics, i.e., the discharge voltage and current, of KrCl discharges and compared them to XeCl discharges, when pumped with a power deposition of 260 kW cm^{-3}, which is a typical

value for a long-pulse XeCl laser. The discharge homogeneity was monitored as a function of time with recording the discharge fluorescence with an intensified CCD camera set to a temporal resolution of 10 ns.

The test set-up was employed to simultaneously initiate discharges in both discharge volumes. In mixtures containing Xe as rare-gas, we found that discharges are homogeneous during the entire duration of the pump current pulse. Although hot spots are observed on the cathode, this does not lead to a filamentation of the bulk of the discharge. In comparison, discharges using Kr at a partial pressure of 100 mbar showed an earlier development of hot spots and a shorter duration of the stable phase of the discharge. For a partial pressure of 1 mbar HCl, the discharge became strongly filamentary already 200 ns after initiation, while for a HCl partial pressure of 0.5 mbar a considerable increase of the stability leads to homogeneous discharges with a duration of 300 ns. These results indicate that KrCl lasers with a long pulse duration, and thus also high beam quality, are feasible.

KrCl discharge laser

In the second part of the thesis and based on the discharge investigations with the test set-up, we designed and constructed a three-electrode KrCl discharge laser set-up in which the two discharge volumes are 80 cm long.

In a first experiment, we tested the laser set-up with XeCl, to compare the quality of our discharge with that in other XeCl lasers, via comparing the output energy, pulse duration, and efficiency. The laser set-up generated laser pulses with a long duration of 130 ns, with a high specific output energy of 1 J/l and with a high efficiency of 3%. This demonstrates a good performance, particularly when considering that neither the resonator nor the drive circuit was optimized for this test with XeCl.

To investigate the operation as a KrCl laser under optimized conditions, we investigated the dependence of the discharge and laser parameters on the gas composition and pump parameters. Using the optimum conditions as found in the test set-up, we achieved very homogeneous discharges in KrCl that enabled the generation of laser

pulses with a long duration of 150 ns. A low beam divergence (smaller than 1 mrad) was observed with both discharge volumes and a plane-plane resonator, when pumping with a power density of 340 kW cm^{-3}. The measured beam divergence is a factor of three smaller than what is found in long-pulse XeCl laser measured under similar circumstances. From this we conclude that the homogeneity that we achieved in the KrCl laser is as high as what was found previously in XeCl lasers. This observation is also supported by low pulse-to-pulse fluctuations of the laser energy and confirmed by transverse inspection of the discharge.

KrCl gain parameters

In the third part of this thesis, we determined for the first time the basic gain parameters of a KrCl in long-pulse operation, i.e., the net gain, small-signal gain, losses, and the saturation intensity. Furthermore, we modeled the KrCl laser with time-dependent rate equations for the resonator internal photon density.

For measurement of the gain parameters, the three-electrode discharge system has been employed in an oscillator-amplifier configuration. As first experiment, the net gain has been measured directly with this scheme and a gain of up to 1.6% cm^{-1} was observed at a HCl partial pressure of 1.5 mbar and a power deposition of 620 kW cm^{-3}. This value is supported by the calculation of the gain using the $KrCl^*$ number density.

From measuring the net gain with different probe intensities, we determined the small-signal gain, loss coefficient, and the saturation intensity. From the saturation intensity we find that collisional quenching reactions reduce the effective upper state lifetime, as the power density increases. Additionally, the losses, though small, are found to be higher than what would be expected from experiments using short-pulse high-power excitation circuits. Based on these measurements, it looked promising to look for a further improvement of the laser pulse duration and energy via optimizing the laser parameters, such as a variation of the output coupling from the resonator.

Optimizing the resonator output coupling and the laser gas composition for high

output energy, we achieved a specific energy of 0.45 J/l and pulse duration of 117 ns. This is a 20% increased pulse energy compared to other KrCl lasers and an almost 20% increased pulse duration.

In search for further improvements of the laser, we modeled the time-dependent resonator-internal photon density, the temporal shape of the output pulses and the pulse energy. For this we employed the experimentally determined, time-dependent gain parameters, which avoids modeling the rather complex discharge dynamics. Despite the simplicity of this model, we found a good agreement of the calculated with the measured laser pulse shapes and pulse energies found with various output couplers.

When using these calculations for an extrapolation, we found that another 30% improvement of the pulse energy should be possible, simply by reducing the resonator length to a value of about 90 cm, while only a minor (10%) shortening of the pulse duration is expected.

Conclusion

In conclusion, this work contributes significantly to the development of discharge pumped KrCl lasers with a high spatial beam quality. As a step of fundamental importance, we developed a KrCl laser with a high homogeneity of the discharge medium, resulting in long pulse duration and high pulse energy. This opens the way to exploit KrCl lasers for applications requiring a short emission wavelength, 222 nm, with a high spatial beam quality. For this, a further optimization of the laser to higher output energies and longer pulse durations seem feasible by reducing the resonator length and the self-inductance of the pump circuit. For the latter, it might be advantageous to place capacitors of the pulse forming network inside the discharge cell, i.e., close to the main electrodes. This way, it would be possible to further reduce the rise time of the discharge current and reach the laser threshold earlier. Furthermore, it seems straightforward to increase the beam quality of the laser to near the fundamental limit of a diffraction-limited beam.

Appendix A

Digital image analysis

To obtain a quantitative comparison between the discharge quality of the various gas mixtures used, the recorded images are analyzed according to the edge detection technique [73]. This technique allows the definition of a numerical value, describing the discharge instability, hereafter called figure of discharge instability. The value of this figure can be determined and compared with the value obtained from homogeneous discharges, allowing to follow the temporal development of discharge instabilities.

Shown in Fig. A.1 is a schematic overview of the image analysis. The image recorded by the CCD is an intensity pattern $I(x_i, y_j)$, where x_i is the horizontal and y_j the vertical position of a pixel in the image. In a first step, noise on the image is reduced. For this, the intensity of the bulk of the discharge, indicated as the center part of the image enclosed by the white box, is averaged in the y direction.

$$\langle I(x_i)\rangle = \frac{1}{N}\sum_{j}^{N} I(x_i, y_j), \tag{A.1}$$

where N is the number of pixels to be averaged. Shown schematically in the figure is a plot of $\langle I(x)\rangle$ as a function of x. In a second step, intensity fluctuations caused for

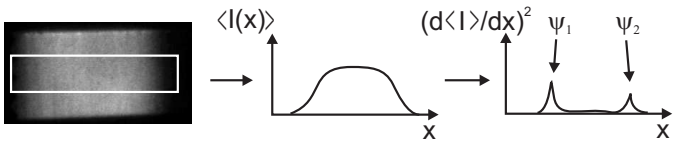

Figure A.1: Schematic overview of the discharge image analysis. The bulk of the discharge is used to determine the discharge quality. Its average intensity is calculated in vertical direction (white box). The result is shown as a function $\langle I(x)\rangle$ of the horizontal (x) position. Differentiating $\langle I(x)\rangle$ with respect to x reveals spatial fluctuations, which are determined as the peak values of the function $\left(d\langle I\rangle/dx\right)^2$.

example by instabilities, are detected calculating the the square of the intensity gradient $d\langle I(x)\rangle/dx$ (see Fig. A.1). Peaks in this derivative represent boundaries between high and low intensities in the intensity pattern. Using the number of determined peaks and the corresponding amplitudes, we define as figure of discharge instability the root-mean-square value (rms) of the amplitudes:

$$\psi_{\mathrm{rms}} = \sqrt{\frac{1}{n}\sum_{i}^{n}\psi_i^2}, \tag{A.2}$$

where n is the total number of peaks located at the different positions x_i with the amplitude $\psi_i = d\langle I(x)\rangle/dx|_{x=x_i}$. This value can be used to represent the discharge quality as strong intensity fluctuations and, consequently, large peak values, contribute more to the sum in Eq. A.2 as a result of the square dependence. The result is that an increasing rms-value represents growing inhomogeneities in the bulk of the discharge.

References

[1] **T. H. Maiman**, *Stimulated optical radiation in ruby*, Nature **187**, 493 (1960).

[2] **R. S. Sze and P. B. Sott**, *Intense lasing in discharge excited noble-gas monochlorides*, Appl. Phys. Lett. **33**, 419 (1978).

[3] **M. Rokni, J. A. Mangano, J. H. Jacob and J. C. Hsia**, *Rare gas fluoride lasers*, IEEE J. Quantum Electron. **QE-14**, 464 (1978).

[4] **R. C. Sze**, *Rare-gas halide avalanche discharge lasers*, IEEE J. Quantum Electron. **QE-15**, 1338 (1979).

[5] **D. J. Elliott**, *Ultraviolet laser technology and applications*, Academic Press, San Diego (1995).

[6] **D. Basting and G. Marowksy**, *Excimer laser technoloy*, Springer, Berlin, Heidelberg (2005).

[7] **Aart Schoonderbeek**, *Laser drilling of metals with a XeCl excimer laser*, PhD thesis, University of Twente, Enschede, The Netherlands (2005).

[8] **J. W. Gerritsen, A. L. Keet, G. J. Ernst and W. J. Witteman**, *High-efficiency operation of a gas discharge XeCl laser using a magnetically induced resonant voltage overshoot circuit*, J. Appl. Phys. **67**, 3517 (1990).

[9] **F. A. van Goor, W. J. Witteman, J. C. M. Timmermans, J. van Spijker and J. Couperus**, *High-average power XeCl laser with x-ray pre-ionization and spiker-sustainer excitation*, Proc. SPIE - Int. Soc. Opt. Eng. (USA) **2206**, 30 (1994).

[10] **R. M. Hofstra, F. A. van Goor and W. J. Witteman**, *Beam divergence studies on hard edge unstable resonators for a long pulse XeCl excimer laser*, Opt. Comm. **144**, 43 (1997).

[11] **J. C. M. Timmermans**, *1-kW industrial excimer laser (308 nm)*, Proc. SPIE - Int. Soc. Opt. Eng. (USA) **3343**, 687 (1998).

[12] **R. M. Hofstra, J. C. M. Timmermans and H. J. G. van Heel**, *On the optical quality of NCLR's 1 kW, 1 kHz XeCl excimer laser*, Proc. Advanced High-Power Lasers **3889**, 388 (2000).

[13] **C. Biesheuvel C, O. van Donselaa, R. Hofstra and A. Krijgsman**, Proc. of ALAC **4**, 92 (2005).

[14] **H. Schmidt, J. Ihlemann, B. Wolff-Rottke, K. Luther and J. Troec**, *Ultraviolet laser ablation of polymers: spot size, pulse duration, and plume attenuation effects explained*, J. Appl. Phys. **83**, 5458 (1998).

[15] **T. Fourrier, G. Schrems, T. Mhlberger, J. Heitz, N. Arnold, D. Buerle, M. Mosbacher, J. Boneberg and P. Leiderer**, *Laser cleaning of polymer surfaces*, Appl. Phys. A **72**, 1 (2001).

[16] **P. E. Dyer**, *Excimer laser polymer ablation: twenty years on*, Appl. Phys. A **77**, 167 (2003).

[17] **M. S. Trtica, B. M. Gaković, L. T. Petkovska, V. F. Tarasenko, A. V. Fedenev, E. I. Lipatov and M. A. Shulepov**, *Surface modifications of TiN coating by the pulsed TEA CO_2 and KrCl laser*, Appl. Surf. Sci. **225**, 362 (2004).

[18] **J. Ihlemann**, *Ultraviolet laser ablation patterning of oxide films for optical applications*, Opt. Engin. **44**, 051108–1 (2005).

[19] **A. E. Siegman**, *Lasers*, University Science Book, Mill Valley, CA, USA (1986).

[20] **P. W. Milonni and J. H. Eberly**, *Lasers*, John Wiley & Sons, Hoboken, New Jersey (1988).

[21] **J. T. Verdeyen**, *Laser electronics*, Prentice-Hall, Englewood Cliffs, New Jersey, 2nd edition (1989).

[22] **E. W. McDaniel and W. L. Nighan**, *Applied atomic collision physics*, Academic Press, New York (1982).

[23] **G. A. Mesyats, V. V. Osipoc and V. F. Tarasenko**, *Pulsed gas lasers*, SPIE, Bellingham, Washington (1995).

[24] **C. S. Willett**, *Gas Lasers: population inversion mechanisms*, Pergamon Press, Oxford, New York, Toronto, Sydney (1974).

[25] **Ch. A. Brau**, *Rare gas halogen excimers*, Ch. K. Rhodes, ed., volume 30 of Topics in Applied Physics, Springer, Berlin, Heidelberg (1984).

[26] **M. Krauss and F. H. Miess**, *Rare gas halogen excimers*, Ch. K. Rhodes, ed., volume 30 of Topics in Applied Physics, Springer, Berlin, Heidelberg (1984).

[27] **V. É. Peét and E. V. Slivinskiĭ**, *Diagnostics of an electric-discharge KrCl laser*, Sov. J. Quantum Electron. **20**, 372 (1990).

[28] **J. Tellinghuisen, J. M. Hoffman, G. C. Tisone and A. K. Hays**, *Spectroscopic studies of diatomic noble gas halides: analysis of spontaneous and stimulated emission from XeCl*, J. Chem. Phys. **74**, 2484 (1976).

[29] **M. C. Castex, J. Le Calvé, D. Haaks, B. Jordan and G. Zimmerer**, *Formation of $KrCl^*$ and $ArCl^*$ molecules and radiative lifetimes of their B states investigated with selective synchrotron radiation excitation*, Chem. Phys. Lett. **70**, 106 (1980).

[30] **Yu. P. Raizer**, *Gas discharge phyics*, Springer-Verlag Berlin Heidelberg (1991).

[31] **A. N. Panchenko and V. F. Tarasenko**, *Maximum Performance of Discharge-Pumped Exciplex Laser at $\lambda = 222$ nm*, IEEE J. Quantum Electron. **31**, 1231 (1995).

[32] **A. Mandl**, *Electron photodetachment cross sections of Cl^- and Br^-*, Phys. Rev. A **14**, 345 (1976).

[33] **V. Radojević, H. P. Kelly and W. R. Johnson**, *Photodetachment of negative halogen ions*, Phys. Rev. A **35**, 2117 (1987).

[34] **L. Feenstra**, *On the long pulse operation of a discharge pumped ArF excimer laser*, PhD thesis, University of Twente, Enschede, The Netherlands (1999).

[35] **H. Hokazono, K. Miorikawa, M. Obara and T. Fujioka**, *Theoretical analysis of a self-sustained discharge pumped XeCl laser*, J. Appl. Phys. **56**, 680 (1984).

[36] **M. M. Turner and P. W. Smith**, *Modeling of the self-sustained, discharge-excited xenon-chloride laser*, IEEE Trans. on Plasma Science **19**, 350 (1991).

[37] **R. Sorkina, F. A. van Goor and W. J. Witteman**, *Simulation studies of the prepulse-main-pulse XeCl discharge lasers with magnetic switching*, Appl. Phys. B **55**, 478 (1992).

[38] **J. I. Levatter and S.-C. Lin**, *Necessary conditions for the homogeneous formation of pulsed avalanche discharges at high gas pressures*, J. Appl. Phys. **51**, 210 (1980).

[39] **J. Coutts and C. E. Webb**, *Stability of transverse self-sustained discharge-excited long-pulse XeCl lasers*, J. Appl. Phys. **59**, 704 (1986).

[40] **M. Kushner**, *Microarcs as a termination mechanism of optical pulses in electric-discharge excited KrF excimer lasers*, IEEE Trans. Plasma Sci. **19**, 387 (1991).

[41] **M. Makarov**, *Effect of electrode processes on the spatial uniformity of the XeCl discharge*, J. Phys. D: Appl. Phys. **28**, 1083 (1995).

[42] **R. Dreiskemper and W. Btticher**, *Current Filamentation of Strongly Preionized High pressure Glow Discharges in Ne/Xe/HCl Mixtures*, IEEE Trans. on Plasma Science **23**, 987 (1995).

[43] **M. Makarov and Y. Bychkov**, *The dynamics of XeCl discharge contraction*, J. Phys. D: Appl. Phys. **29**, 350 (1996).

[44] **R. S. Taylor**, *Preionization and discharge stability study of long optical pulse duration UV-preionized XeCl lasers*, Appl. Phys. B **41**, 1 (1986).

[45] **A. Garscadden, M. J. Kushner and J. G. Eden**, *Plasma Physics Issues in Gas Discharge Laser Development*, IEEE Trans. on Plasma Science **19**, 1013 (1991).

[46] **J. J. Ewing**, *Excimer Laser Technology*, IEEE J. Selec. Topics Quantum Electron. **6**, 1061 (2000).

[47] **S. Watanabe and A. Endoh**, *Wide aperture self-sustained discharge KrF and XeCl lasers*, Appl. Phys. Lett. **41**, 799 (1982).

[48] **E. Armandillo, A. Luches, V. Nassisi and M. R. Perrone**, *Improved lasing performance of KrCl excimer laser*, Appl. Phys. Lett. **42**, 860 (1983).

[49] **K. Miyazaki, T. Hasama, K. Yamada, T. Fukatsu, T. Eura and T. Sato**, *Efficiency of a capacitor-transfer-type discharge excimer laser with automatic preionization*, J. Appl. Phys. **60**, 2721 (1986).

[50] **R. Nodomi, Y. Oeda, K. Sajiki, S. Nakajima, M. Watanabe and S. Watanabe**, *High-repetition rate, wide-aperture KrF lasers for subpicosecond amplification*, IEEE J. Quantum Electron. **27**, 441 (1991).

[51] **R. S. Taylor and K. E. Leopold**, *Magnetically induced pulser laser excitation*, Appl. Phys. Lett. **46**, 335 (1985).

[52] **H. M. J. Bastiaens, S. J. M. Peeters, X. Renard, P. J. M. Peters and W. J. Witteman**, *Long pulse operation of an x-ray preionized molecular*

fluorine laser excited by a prepulse-main pulse system with a magnetic switch, Appl. Phys. Lett. **72**, 2791 (1998).

[53] **R. S. Taylor and K. E. Leopold**, *Ultralong optical-pulse corona preionized XeCl laser*, J. Appl. Phys. **65**, 22 (1989).

[54] **R. S. Taylor and K. E. Leopold**, *Magnetic-spiker excitation of gas-discharge lasers*, Appl. Phys. B **59**, 479 (1994).

[55] **J.-M. Hueber, B. L. Fontaine, N. Bernard, B. M. Forestier, M. L. Sentis and Ph. C. Delaporte**, *Long pulse KrCl excimer laser at 222 nm*, Appl. Phys. Lett. **61**, 2269 (1992).

[56] **V. V. Borovkov, V. V. Voronin, S. L. Voronov, D. I. Zenkov, B. V. Lazhintsev, V. A. NorArevyan, V. A. Tananakin, G. I. Fedorov and I. M. Yutkin**, *Three-electrode discharge laser with a middle control electrode*, Quant. Electron. **25**, 414 (1995).

[57] **T. J. McKee and S. D. Hastie**, *Performance of a novel injection-locked excimer laser*, J. Appl. Phys. **56**, 2170 (1984).

[58] **V. V. Borovkov, V. V. Voronin, S. L. Voronov, D. I. Zenkov, B. V. Lazhintsev, V. A. NorArevyan, V. A. Tananakin and G. I. Fedorov**, *Highly efficient gas laser with a three-electrode double discharge*, Quant. Electron. **26**, 39 (1996).

[59] **S. Bollanti, P. di Lazzaro, F. Flora, T. Letardi, D. Murra, C. Petrucci and O. Uteza**, *Study of a compact three-electrode oscillator-amplifier excimer laser system*, Opt. Comm. **132**, 565 (1996).

[60] **S. Bollanti, P. di Lazzaro, F. Flora, G. Giordano, T. Letardi, G. Schina and C. E. Zheng**, *Ianus, the three-electrode excimer laser*, Appl. Phys. B **66**, 401 (1998).

[61] **V. V. Borovkov, A. V. Andramanov and S. L. Voronov**, *Interferometric investigations of the plasma in a three-electrode XeCl laser*, Quant. Electron. **29**, 19 (1999).

[62] **S.-C. Lin and J. I. Levatter**, *X-ray preionization for electric discharge lasers*, Appl. Phys. Lett. **34**, 505 (1979).

[63] **M. S. Pronko**, *Controlling output gain uniformity by spatial variation of the x-ray preionization in large-aperture discharge-pumped KrF apmlifier*, IEEE J. Quantum Electron. **30**, 2147 (1994).

[64] **S. J. Scott**, *Development of a long life, 2 kHz repetition rate X-ray preionizer*, Appl. Phys. B **56**, 201 (1993).

[65] **F. H. Attex, W. C. Roesch and E. Tochilen**, *Radiation Dosimetry, Vol. F*, Academic, New York (1968).

[66] **G. J. Hine and G. L. Brownell**, *Radiation Dosimetry*, Academic, New York (1956).

[67] **H. A. Kramers**, Phil. Mag. **46**, 863 (1923).

[68] **F. A. van Goor**, *Fast rise time x-ray pre-ionization source using a corona plasma cathode*, J. Phys. D: Appl. Phys. **26**, 404 (1993).

[69] **J. C. M. Timmermans**, *Double discharge XeCl laser*, PhD thesis, University of Twente, Enschede, The Netherlands (1995).

[70] **H. M. J. Bastiaens**, *On the long pulse operation of a molecular fluorine laser*, PhD thesis, University of Twente, Enschede, The Netherlands (2000).

[71] **NIST physical reference data: X-ray attenuation coefficients**, http://physics.nist.gov/PhysRefData/XrayMassCoef/cover.html.

[72] **S. Bollanti, F. Bonfigli, P. Di Lazzaro, F. Flora, G. Giordano, T. Letardi, D. Murra, and G. Schina**, *Pulsed x-ray generator for commercial gas lasers*, Rev. Sci. Instrum. **72**, 3983 (2001).

[73] **T. Acharaya and A. K. Ray**, *Image processing: principles and applications*, John Wiley & Sons, Hoboken, New Jersey (2005).

[74] **J. D. Daugherty, J. A. Mangano and J. H. Jacob**, *Attachment-dominated electron-beam-ionized discharges*, Appl. Phys. Lett. **28**, 581 (1976).

[75] **R. M. Hofstra**, *On the optical performance of the long pulse $XeCl^*$ laser*, PhD thesis, University of Twente, Enschede, The Netherlands (1999).

[76] **F. A. van Goor, M. Trentelman, J. C. M. Timmermans and W. J. Witteman**, *Improved X-ray switched XeCl laser*, J. Appl. Phys. **75**, 621 (1994).

[77] **E. Armandillo, A. Luches, V. Nassisi and M. R. Perrone**, *Gain measurements in the KrCl excimer laser*, Appl. Opt. **24**, 18 (1985).

[78] **A. Luches, V. Nassisi and M. R. Perrone**, *Determination of the unsaturated losses and of the saturation intensity in the KrCl excimer Laser*, Appl. Phys. B **40**, 115 (1986).

[79] **T. J. McKee**, *Optical cavity design for long pulse excimer lasers*, Appl. Opt. **30**, 635 (1991).

[80] **S. Bollanti, P. di Lazzaro, D. Murra and Z. E. Zheng**, *More about the self-filtering unstable resonators*, Opt. Comm. **209**, 383 (2002).

[81] **M. Shimauchi, T. Miura and K. Oikawa**, *Absorption lines in the KrCl laser spectrum and the spontaneous emission of the medium related to KrCl*, Jpn. J. Appl. Phys. **25**, 1556 (1986).

[82] **J. K. Rice, C. Tisone and E. L. Patterson**, *Oscillator performance and energy extraction from a KrF laser pumped by a high-energy relativistic electron beam*, IEEE J. Quantum Electron. **QE-16**, 1315 (1980).

[83] **W. W. Rigrod**, *Homogeneously broadened cw lasers with uniform distributed loss*, IEEE J. Quantum Electron. **QE-14**, 377 (1978).

[84] **D. S. Ong, T. Y. Tou and K. S. Low**, *Kinetics modelling of a self-sustained discharge KrF laser*, J. Phys. D: Appl. Phys. **29**, 2586 (1996).

Acknowledgment

Finally, I would like to express my thanks to all those who have supported, guided, helped and inspired me throughout the past four years.

Firstly, I would like to thank Prof. Dr. Klaus Boller and Huub van Heel for the opportunity to be part of this project between the Nederlands Centrum voor Laser Research B.V. (NCLR) and the Laser Physics and Nonlinear Optics Group (LPNO). I would like to thank especially Klaus for the helpful discussions and also for the inspiration he is, demonstrating how elegant complicated physical problems can be explained.

My special thanks go to my supervisors, Dr. Bert Bastiaens and Dr. Ramon Hofstra (NCLR), to whom I am grateful for their support, guidance, and patience. Thank you, Bert, not only for the many discussions, remarks, and criticisms that were so valuable during the past years, but also for your sense of humor that made the work in the laboratory always a bit easier.

I am very grateful to Gerard Oude-Meijers, Jacob Couperus, and Leon Raanhuis for their invaluable technical support. Also, I would like to thank Arco Krijgsman for the various times I could ask for help, typically on a rather short notice. Many thanks also to Emiel Speets and Mark Smithers (both MESA+) for XPS and SEM & EDX measurements.

For the help on the manuscript, I would like to give my extra thanks to Piet Peters

and Chris Lee, and for the help on translating the summary, Bert Bastiaens.

To the colleagues with whom I spent so much time sharing the same laboratory, Denny, Anton, and Hassan, I want to say that this time has been more than a pleasure for me. Denny, thank you for being such a great friend and that I could always rely on you when I needed your help! Also, I want to thank Hassan for the cheerful and inspiring discussions we had during lunch break or during a billiard game after work.

It has been a great experience for me to share the office with you, Balaji, Isabel, Denis, Liviu, Peter, and Roel. It was a joyful time to be surrounded by so many different characters and I will always remember the good atmosphere in our office. Also many thanks to the other PhD students of the group, Rolf, Arie, Ab, and Willem.

To the people I spent regularly the lunch break with, Petra, Chris, Ian and, as former colleagues, Marvin and Claudia, thank you for the daily opportunity to compare our opinions about the various aspects of physics and life.

I want to thank all the other members of the Laser Physics Group and NCLR that welcomed me and helped me in the one or the other way: Piet, Peter, Aarsen, Cees, Fred, Jeroen, Simone and Otto.

The, not always easy, last years showed me again what good friends I have. For the patience, the listening and the support, I want to thank you, Monica, Marco, Elena, and Giorgia.

To my family I am very grateful for the constant encouragement I received. Especially, I thank my grandmother for her support and her patience to accept my sometimes long silence. Jens, my brother, thank you for the many times that you called in the right moment to ask how things are going. You have been a big support during these years!